# CHARACTERISATION OF SI–SI BONDED WAFERS AND LOW-K SILICA XEROGEL FILMS BY MEANS OF OPTICAL SPECTROSCOPIES

von der Fakultät für Naturwissenschaften der Technischen Universität Chemnitz
Genehmigte Dissertation zur Erlangung des akademischen Grades

doctor rerum naturalium
(Dr. rer. nat.)

vorgelegt von Master in Physik Cameliu Constantin Himcinschi
geboren am 29. Juni 1974 in Blaj

eingereicht am 25 November 2002

Gutachter:
Prof. Dr. Dietrich R.T. Zahn
Prof. Dr. Thomas Gessner
Prof. Dr. Ulrich M. Gösele

Tag der Verteidigung: 7 April 2003

## Bibliographische Beschreibung

Cameliu Constantin Himcinschi

**Characterisation of Si–Si bonded wafers and low-k silica xerogel films by means of optical spectroscopies.**

Technische Universität Chemnitz

*Dissertation* (in englischer Sprache), 2002

## Referat

In dieser Arbeit werden als Untersuchungsverfahren für die Charakterisierung von gebondeten Siliziumwafern und Siliziumoxid-Xerogel-Schichten spektroskopische Ellipsometrie mit variablem Einfallswinkel (VASE) und Fouriertransformations-infrarotspektroskopie (FTIR) eingesetzt.

Aus dem Verhalten der LO- und TO-Moden in den Infrarotspektren werden Veränderungen der Dicke und Struktur der vergrabenen Grenzfläche zweier Wafer bei einer Wärmebehandlung abgeleitet. Es werden Mechanismen für das Tieftemperaturbonden von Wafern, die auf der Entwicklung der chemischen Spezies an der vergrabenen Grenzfläche basieren, vorgeschlagen. Die chemischen Spezies wurden durch interne Vielfachtransmissionsinfrarotspektroskopie ermittelt.

Aus ellipsometrischen Messungen wurden Dicke, optische Konstanten, Porosität und Porenabmessungen von Siliziumoxid-Xerogel bestimmt. Mittels VASE und FTIR wurde der Einfluss unterschiedlicher Hydrophobisierungsprozesse auf die Eigenschaften von Xerogel-Schichten untersucht. Weiterhin wurden die elektronischen und ionischen Beiträge zur statischen Dielektrizitätskonstanten bestimmt.

## Schlagwörter

Infrarotspektroskopie, Ellipsometrie, Siliziumwaferbonden, interne Vielfach-transmission, vergrabene Grenzfläche, Siliziumoxid, longitudinale und transversale (LO und TO) optische Phononen, Xerogel, optische Konstanten, Porosität, Dielektrizitätskonstante

**Parts of this work are already published:**

**1.** C.Himcinschi, A.Milekhin, M.Friedrich, K.Hiller, M.Wiemer, T.Gessner, S.Schulze, and D.R.T.Zahn – *Growth of buried silicon oxide in Si-Si bonded wafers upon annealing*, **J. Appl. Phys**. 89, 1992-1994, (2001).

**2.** C.Himcinschi, M.Friedrich, C.Murray, I.Streiter, S.Schulz, T.Gessner, D.R.T.Zahn – *Characterisation of silica xerogels films by variable angle spectroscopic ellipsometry and infrared spectroscopy*, **Sem. Sci. Technol.** 16, 806-811, (2001).

**3.** C.Himcinschi, A.Milekhin, M.Friedrich, K.Hiller, M.Wiemer, T.Gessner, S.Schulze, and D.R.T.Zahn – *Silicon oxide in Si-Si bonded wafers,* **Appl. Surf. Sci.** 175-176, 716-721, (2001).

**4.** C.Murray, C.Flannery, I.Streiter, S.E.Schulz, M.R.Baklanov, K.P.Mogilnikov, C.Himcinschi, M.Friedrich, D.R.T.Zahn, and T.Gessner – *Comparison of Techniques to Characterise the Density, Porosity and Elastic Modulus of Porous Low-k $SiO_2$ Xerogel Films*, **Microelectr. Engineering** 60, 133-141, (2002).

**5.** S.Fruehauf, I.Streiter, S.E.Schulz, E.Brendler, C.Himcinschi, M.Friedrich, T.Gessner, D.R.T.Zahn – *Hydrophobisation process for porous low K dielectric silica layers*, **Conference Proceedings ULSI XVII,** 287-294, (2002) (published by MRS).

**6.** C.Himcinschi, M.Friedrich, S.Frühauf, I.Streiter, S.E.Schulz, T.Gessner, M.R.Baklanov, K.P.Mogilnikov, and D.R.T.Zahn – *Ellipsometric study of the change in the porosity of silica xerogels after chemical modification of the surface with hexamethyldisilazane*, **Anal. Bioanal. Chem.** 374, 654-657 (2002).

**7.** C.Himcinschi, M.Friedrich, K.Hiller, T.Gessner, D.R.T.Zahn – *Investigation during annealing of the interface in Si-Si bonded wafers by multiple internal transmission infrared spectroscopy* , International Semiconductor Conference (CAS) 2002, 8-12 October, 2002, Sinaia, Romania, **CAS 2002 Proceedings**, vol. 2, 271-274, (2002) (published by IEEE).

# CONTENTS

LIST OF ABBREVIATIONS ..... 6

**1 INTRODUCTION ..... 7**

1.1. SILICON WAFER BONDING ..... 7

1.2. SILICA XEROGEL FILMS ..... 8

**2 SAMPLE PREPARATION ..... 10**

2.1. SILICON-SILICON BONDED WAFERS ..... 10

2.2. SILICA XEROGELS ..... 12

**3 EXPERIMENTAL TECHNIQUES; MEASUREMENT PROCEDURES AND DATA EVALUATION ..... 15**

3.1. INFRARED SPECTROSCOPY ..... 15

*3.1.1. Theoretical basics ..... 15*

*3.1.2. Fourier Transform Infrared Spectroscopy. Experimental set-up ..... 20*

*3.1.3. Multiple Internal Transmission ..... 23*

*3.1.4. Heating chamber for in situ MIT measurements ..... 28*

3.2. VARIABLE ANGLE SPECTROSCOPIC ELLIPSOMETRY ..... 30

*3.2.1. Principles. Experimental set-up ..... 30*

*3.2.2. Models for data evaluation ..... 34*

*3.2.3. Ellipsometric Porosimetry ..... 37*

**4 PROPERTIES OF SI—SI BONDED WAFERS. ..... 39**

4.1. HIGH TEMPERATURE SI—SI WAFER BONDING WITH RCA AND $O_2$ PLASMA PRETREATMENT. ..... 39

*4.1.1. Determination of surface oxide thickness ..... 39*

*4.1.2. Evaluation of the "reststrahlen" band: Strain relaxation of the surface oxide with annealing. ..... 40*

*4.1.3. Determination of buried interface thickness: growth of interface oxide with annealing. ..... 44*

4.2. LOW TEMPERATURE WAFER BONDING ..... 49

*4.2.1. Monitoring of chemical species at buried interfaces during annealing of RCA, $O_2$-plasma and RIE Si—Si bonded wafers. ..... 49*

*4.2.2. MIT investigation of Si-$SiO_2$ / Si bonded wafers ..... 55*

4.3. MECHANISMS FOR LOW TEMPERATURE SILICON WAFER BONDING. ..... 59

***5 PROPERTIES OF POROUS LOW-K XEROGEL FILMS. ..... 61***

5.1. DETERMINATION OF THICKNESS, POROSITY AND OPTICAL CONSTANTS OF XEROGEL FILMS. ..... 61

*5.1.1. Reliability of thickness determined using Cauchy model. ..... 66*

5.2. HYDROPHOBISATION PROCESSES FOR POROUS LOW-K SILICA XEROGEL FILMS ..... 68

*5.2.1. FTIR investigation of the hydrophobisation mechanism. ..... 68*

*5.2.2. Influence of the hydrophobisation process on the porosity of silica xerogel films. ..... 73*

*5.2.3. Ellipsometric Porosimetry (EP) results. ..... 79*

*5.2.4. FTIR investigation of cap-layer deposition on xerogel films. ..... 82*

5.3. CONTRIBUTIONS TO DIELECTRIC CONSTANT. ..... 83

***6 CONCLUSIONS ..... 88***

REFERENCES ..... 90

LIST OF TABLES ..... 95

LIST OF FIGURES ..... 96

ERKLÄRUNG ..... 100

LEBENSLAUF ..... 101

PUBLICATION LIST ..... 102

ACKNOWLEDGEMENTS ..... 103

# List of abbreviations

AR – autoretarder
AS – asymmetric stretching
ATR – Attenuated Total Reflection
DTGS – Deuterated Triglycine Sulphate
EMA – Effective Medium Approximation
EP – Ellipsometric Porosimetry
ET – external transmission
FTIR – Fourier Infrared Spectroscopy
HMDS – hexamethydisilasane
HRTEM – High Resolution Transmission Electron Microscopy
IR – Infrared
LO – Longitudinal Optical
MCT – Mercury Cadmium Telluride
MIR – Multiple Internal Reflection
MIT – Multiple Internal Transmission
MSE – Mean Square Error
OTMSA – trimethylsilylacetate
PECVD – Plasma Enhanced Chemical Vapour Deposition
PSD – Pore Size Distribution
RCA – Radio Corporation America
RIE – Reactive Ion Etching
RT – room temperature
SEM – Scanning Electron Microscopy
TEOS – tetraethoxysilane
TMS – trimethylsilyl
TMSDEA – trimethylsilyldiethylamine
TO – Transverse Optical
VASE – Variable Angle Spectroscopic Ellipsometry

# Chapter 1
# Introduction

## 1.1. Silicon wafer bonding

Silicon wafer bonding is an attractive technique to produce silicon-on-insulator (SOI) related microelectromechanical sensors (MEMS) [Ton99, Cri01]. Recently, much attention has been concentrated on studies of the Si-Si bonding mechanism and atomic arrangement at the buried interface [Fei94, Cha95, Wel96a] because the characterisation of the bonded interface is of paramount importance for improving bonding strength, specially for low temperature wafer bonding processes.

Non-destructive techniques are strongly required for the characterization of structure, thickness, stoichiometry, and strain in silicon oxide layers. Since the bonded interface is buried, classical surface techniques are unable to characterise it. Infrared (IR) spectroscopy is one of the few techniques which can supply valuable information about the chemistry of the bonded interface. In particular Multiple Internal Transmission (MIT) IR spectroscopy was recently successfully employed to study the buried interface in Si-Si bonded wafers [Wel96b, Mil00].

The IR studies of silicon oxide demonstrated that the longitudinal and transverse optical (LO and TO) phonons provide valuable information on the internal structure of the oxide. The behaviour of these modes is correlated with changes in stoichiometry [Dev96] or stress relaxation [Luc87, And00]. The MIT technique was also used for the evaluation of buried silicon oxide layer thicknesses in Si-Si bonded wafers based on the analysis of MIT IR absorption by the LO phonons in silicon oxide [Wel96b]. Nevertheless, no independent measurements have been performed to confirm the values obtained.

This work presents an investigation of the influence of annealing and wafer pretreatment on the properties of oxide layers which are formed at the surface and the interface of Si-Si bonded wafers using IR spectroscopy and ellipsometry. The results obtained by means of a non-destructive MIT IR two-prisms coupling geometry during annealing of Si-Si bonded wafers prepared using different prebonding procedures are also presented.

## 1.2. Silica xerogel films

In ultra-large-scale-integration (ULSI) technology the performance of electronic circuits is limited by the resistance-capacitance delay associated with the parasitic capacitance of the dielectric and with the resistance of the metal [Hav98]. Integration of low dielectric constant materials can be applied as an effective way to solve this challenge. Because of its low dielectric constant $\varepsilon$, porous silica prepared as aerogels (dried supercritically) or xerogels (dried by solvent evaporation) [Jin97, Nit99], has become an attractive means of meeting this challenge. Besides the low dielectric constant which is due to the high porosity, these materials have the advantage of a good compatibility with conventional Si technology [Aoi97].

The surfaces of porous silica obtained by sol-gel methods are covered by OH groups [Brin90]. Owing to these OH groups the pore surfaces readily adsorb water leading to an dramatic increase of $\varepsilon$ because of the high polarizability of water molecules. To stabilize electrical properties and to get a sufficient reliability for further integration steps the xerogels films have to be made hydrophobic. The hydrophilic OH species can be removed from the pores and replaced with hydrophobic trimethylsilyl (TMS) groups by chemical modification of the surface [Nit99, Sla00].

Dielectric properties of silica xerogels are strongly influenced by the chemical composition and the porosity of the films. In this work a non-destructive optical spectroscopy study resulting in a complete characterization of the xerogel films, in terms of thickness, optical constants, porosity and pore dimension is presented. The changes in the properties of the film induced by the hydrophobisation process are investigated. The electronic and ionic contributions to static dielectric constant were also established.

In literature the materials with low dielectric constant are known as “low-k materials”. In this work the dielectric constant is denoted by $\varepsilon$.

This work is organized as follows. *Chapter 2* shows the procedures used for preparation of Si-Si bonded wafers and silica xerogels films. In *Chapter 3* the experimental techniques employed in this work are introduced. The theoretical basics of Fourier Transform Infrared (FTIR) and Variable Angle Spectroscopic Ellipsometry

(VASE) are discussed. A description of the two-coupling prisms Multiple Internal Transmission (MIT) geometry used and its advantages are given. In addition, the models for evaluation of the ellipsometry results are described. The results concerning high temperature and low temperature Si-Si wafer bonding are presented in *Chapter 4*. The changes with annealing of the structure and thickness of the buried interfacial oxide are monitored and analyzed. On the basis of MIT results mechanisms for low temperature wafer bonding are proposed. *Chapter 5* shows the results obtained by probing xerogel films using optical spectroscopies. A method for the characterization of these films (in terms of thickness, optical constants, porosity, pore dimensions) is introduced. Hydrophobisation process and its influence on the properties of the films are examined in detail. The electronic and ionic contributions to static dielectric constant were also established. Finally *Chapter 6* summarizes the results obtained.

# Chapter 2
# Sample Preparation

## 2.1. Silicon-silicon bonded wafers

Czochralski-grown (100)-*p*-Si (4 in. diameter, 463µm, 10-40 Ωcm, double side polished) wafers were used for the room temperature (RT) bonding process. In order to achieve hydrophilic Si surfaces different wet chemical treatments and surface plasma activation were used as presented in table 2.1. The aim of these pre-treatments is to create reactive bonding surfaces for Si wafers in order to achieve strong bonding of two Si wafers. The wafer bonding was realized in the Center of Microtechnology Chemnitz in a clean-room.

| *No.* | *Pre-treatment* | *Steps* | *Time/min* | *Temp.* |
|---|---|---|---|---|
| *1.* | *RCA* | *$NH_3OH:H_2O_2:H_2O$ = 1:1:6* | *10* | *75°C* |
| | | *DI-Rinsing* | *15* | *RT* |
| | | *HCL:$H_2O_2$:$H_2O$ = 1:1:6* | *10* | *75°C* |
| | | *DI-Rinsing* | *15* | *RT* |
| | | *$NH_3OH:H_2O_2:H_2O$ = 1:1:6* | *10* | *75°C* |
| | | *DI-Rinsing* | *15* | *RT* |
| *2.* | *$O_2$-Plasma (Barrel reactor)* | *p=1,33Pa, P=800W, RCA or DI-Rinsing* | *15* | *-* |
| *3.* | *$O_2$-plasma (RIE-reactor)* | *p=10Pa, P=15W, Bias=110V RCA or DI-Rinsing* | *5* | *-* |

***Table 2.1.*** Description of the pre-treatments of the Si wafers before room temperature bonding.

By RCA treatment the native oxide Si surfaces or thermally oxidised Si surfaces can be activated, and the water molecules will attack the most strained Si-O-Si bridges according to the reaction [Ton1]:

$$\text{Si-O-Si} + \text{H-OH} \rightarrow \text{Si-OH} + \text{Si-OH} \qquad (2.1)$$

In this way the number of silanol (Si-OH) species increases especially for native oxide surfaces which contain strained siloxane (Si-O-Si) groups and can be easily attacked by water molecules. The silanol species are very important in the bonding

process of Si wafers because they can polymerize forming siloxane bridges between the surfaces of the two Si wafers. By $O_2$ plasma activation plasma-induced defects are created on the Si surfaces increasing the chemical reactivity.

After surface activation processes the Si wafers were dried in a spin dryer. The wafers were subsequently bonded in air at room temperature using a bond equipment consisting of a wafer holder made from Piacryl and allowing a flat alignment of the wafers. The inspection of the bonding process is realized by a Hamamatsu IR imagining system as shown in the figure 2.1.

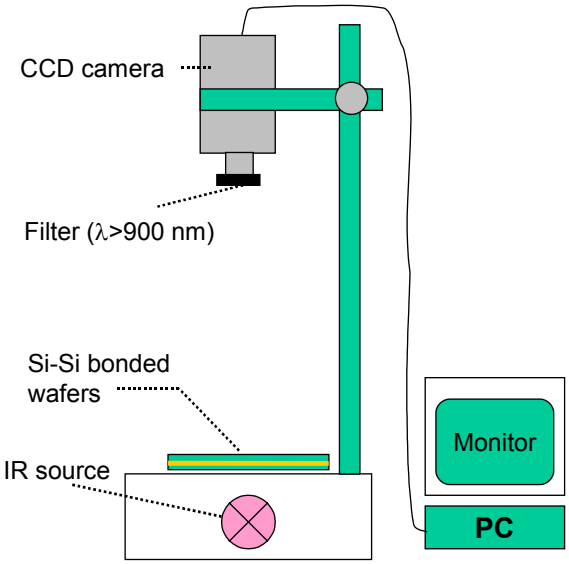


***Fig. 2.1***. Schematic representation of the IR imaging system used to control the bonding quality.

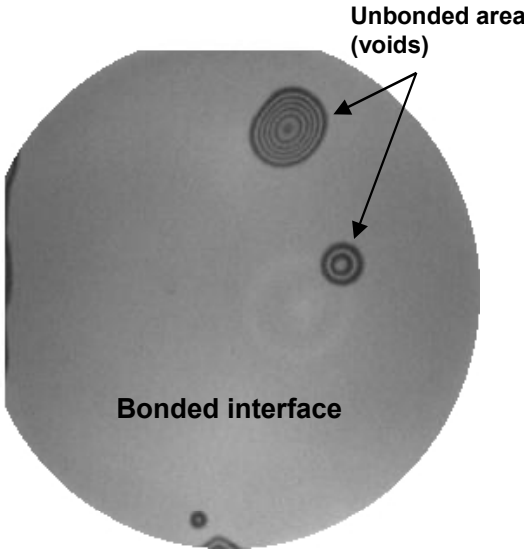


***Fig. 2.2.*** IR transmission image of a Si-Si wafer bond system showing unbonded regions at the interface

The wafers in horizontal position are put together face to face and a low pressure point contact initiates the bonding front, which spreads over the wafers interface within few seconds. IR transmission pictures of the samples are taken after pre-bonding showing voids and other unbonded areas (figure 2.2). After prebonding the samples were annealed using a temperature controlled oven with air flow for 200°C annealing and a furnace tube with nitrogen flow for 400°C and higher temperature. After annealing the samples were inspected

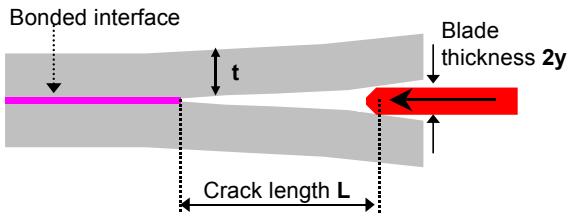


***Fig. 2.3.*** Schematic diagram of the blade test method

again using the IR transmission system in order to detect eventual bubbles generated by annealing. Part of the pre-bonded samples, which were used for *in situ* Multiple Internal Transmission (MIT) infrared investigations were annealed in a low vacuum chamber as will be described in the Chapter 3.

For the measurement of the bond strength the blade test method [Mas88] was used. The wafers are diced into stripes of 10 mm width using a wafer saw. A razor blade (100 µm thickness) is slowly inserted at the bonded interface starting from the wafer edge. The length of the unbonded area is measured using the IR system. From this measurement, the specific bond energy $\gamma$ can be calculated from the geometry of the specimen using the formula:

$$\gamma = \frac{3Et^3y^2}{8L^4} \tag{2.2}$$

where E is the elastic modulus, t is the thickness of Si wafer, 2y is the thickness of the blade and L is the length of the crack. The error in determination of bonding energy by this method is of the order of 10%.

## 2.2. Silica Xerogels

The technology to produce silica xerogels films is based on a sol-gel / spin-on process [Bri90, Win98] and is schematically presented in the figure 2.4. A mixture of tetraethoxysilane (TEOS), water, solvent (alcohol) and a catalyst (acid) is transformed into a gel. TEOS is first hydrolised by the reaction with water:

$$Si(OR)_4 + H_20 \rightarrow (RO)_3SiOH + ROH \tag{2.3}$$

where R is $C_2H_5$ in the case of TEOS. After hydrolysis has started, water or alcohol condensation reactions occur (Eq. 2.4 and 2.5 respectively) forming siloxane bonds (Si-O-Si) and liberating water or alcohol:

$$(RO)_3SiOH + HOSi(RO)_3 \rightarrow (RO)_3\mathbf{Si\text{-}O\text{-}Si}(RO)_3 + H_20 \tag{2.4}$$

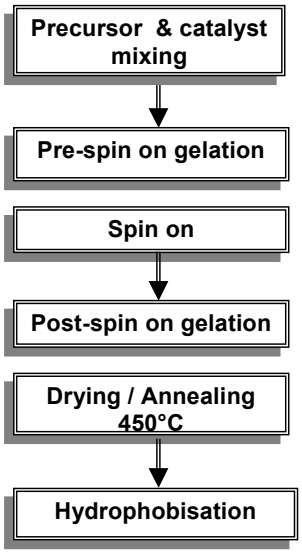


***Fig. 2.4.*** Scheme of the xerogel fabrication process.

$$(RO)_3SiOR + HOSi(RO)_3 \rightarrow (RO)_3\mathbf{Si\text{-}O\text{-}Si}(RO)_3 + R0H \qquad (2.5)$$

Since TEOS is tetrafunctional, a polymerisation phenomenon appears with the formation of three dimensional silica clusters as a result of hydrolysis and condensation reactions. The rates of hydrolysis and condensation can be controlled by the catalyst (monitored by PH values) and by the ratio $H_2O$:TEOS in the initial solution [Bri90]. Spin-on was performed when the precursor solution viscosity was in the region of 10-15 mPa·s, which has been found to produce highly homogeneous films [Sch01]. The solution was spun on Si wafers (4 or 6-inch diameter) at various spin speeds from 1000 to 1500 rpm for 10 s. The silica clusters become attached one to the other forming a porous network in a process called aging [Nit99]. Mixing and aging time as well as the spin speed were varied in order to get samples with different porosities and thicknesses.

After spin-on stress in the film occurs and related capillary forces due to the presence of the solvent into the pores. Depending on the drying process used to remove the solvent from the pores, porous silica has been classified as aerogel (dried supercritically) or as xerogel (dried by solvent evaporation) [Jin97]. For the samples under investigation in this work drying was realized by exposure to air. The xerogel films were then annealed in vacuum at 450°C for 1h.

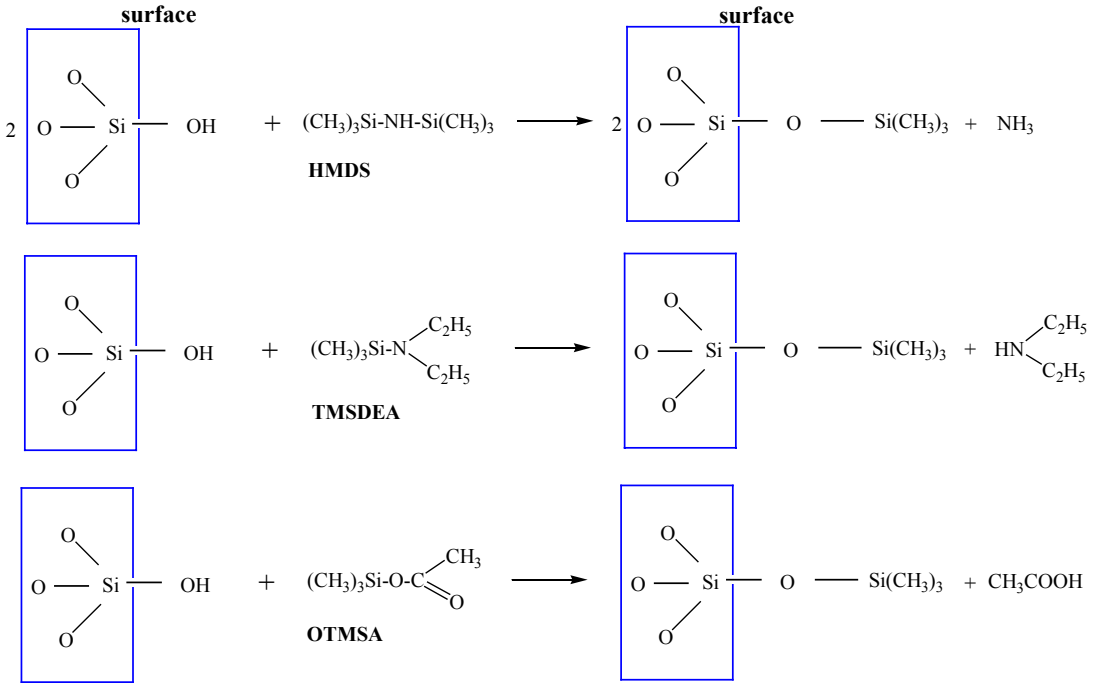


***Fig. 2.5.*** Silylation reaction scheme for different chemicals [Fru02].

Even after annealing the xerogels films contain a large amount of SiOH groups which can readily adsorb water. Adsorbed moisture increases the dielectric constant due to the high polarity of the water molecules. The hydrophilic OH groups can be removed by surface chemical modification and the inner surface of the pores becomes a hydrophobic one. Hydrophobisation is achieved by silylation, that means surface silanol groups react to yield trimethylsilyl (TMS) surface groups. Especially hexamethydisilasane (HMDS) was employed because of its high reactivity with silica surface silanol due to its basic nitrogen [Gun00]. Other hydrophobisation agents were also employed for the samples studied in this work: trimethylsilyldiethylamine (TMSDEA) or trimethylsilylacetate (OTMSA) [Fru02]. Hydrophobisation treatment followed immediately after annealing by exposure of the films to saturated vapors of HMDS, TMSDEA or OTMSA, at room temperature in a close container. The scheme of the reaction of silica xerogels films with these different chemicals is presented in figure 2.5.

# Chapter 3

# Experimental Techniques; Measurement Procedures and Data Evaluation

## 3.1. Infrared Spectroscopy

### 3.1.1. Theoretical basics

The vibrational and rotational motions of constituents of matter have their natural frequencies in the infrared (IR) range (10-10000 $cm^{-1}$). When an IR beam interacts with a sample and the frequency of the radiation matches a natural vibrational frequency of the molecules, a net transfer of energy takes place resulting in a change of the amplitude of the molecular vibration and a corresponding absorption of the radiation [Sko92]. The ratio between the intensity of the beam measured after and before interaction of IR light with the sample plotted as a function of the frequency of the light represents an IR spectrum.

The transition moment for infrared absorption can be written as: $\mathbf{M_{IR}}=<\Psi_i|\,\boldsymbol{\mu}\,|\Psi_j>$, where $\Psi_i$ and $\Psi_j$ are the initial and the final states and $\boldsymbol{\mu}$ is the electric dipole operator: $\boldsymbol{\mu}=\boldsymbol{\mu_0}+(r-r_e)(d\boldsymbol{\mu}/dr)+\ldots$, $\boldsymbol{\mu_0}$ is the permanent dipole moment which is constant. Because $<\Psi_i|\,\Psi_j>=0$, the transition moment for IR absorption can be written as: $\mathbf{M_{IR}}=<\Psi_i\,|\,(r-r_e)(d\boldsymbol{\mu}/dr)|\,\Psi_j>$. To have IR absorption by a molecule it is necessary that the molecule undergoes **a change in the dipole moment ($d\mu/dr\neq0$)** during vibration. Only in these conditions the electric field of the radiation interacts with the molecule and can cause changes in the amplitude of its motion.

Molecular vibrations can be classified in stretching and bending vibrations (see Figure 3.1). Stretching vibration involve a rhythmical movement along the bond axis, so that interatomic distance changes. Bending vibrations are characterized by a change in the angle between two bonds and are of four types: rocking, scissoring, wagging and twisting.

### *Classical model of vibration in a diatomic molecule*

The compression and extension of a bond in a diatomic molecule can be compared to the behaviour of a spring. If a mass *m* is displaced by a distance ***r*** from its equilibrium position by application of a force along the axis of the spring, the restoring force **F** is proportional to the displacement (Hooke's law): $\boldsymbol{F}=-k\cdot\boldsymbol{r}$ where *k* is the force constant. The energy curve is parabolic (see figure 3.2) and has the form $E=1/2\cdot k(r-r_{ech})^2$. Considering a diatomic molecule as a system consisting of two masses $m_1$ and $m_2$ connected by a spring, the vibrational frequency is given by:

$$\bar{\nu}=\frac{\nu}{c}=\frac{1}{2\pi}\sqrt{\frac{k}{\mu}}=\frac{1}{2\pi}\sqrt{\frac{k(m_1+m_2)}{m_1m_2}} \qquad (3.1)$$

where μ is the reduced mass of the system and $\bar{\nu}$ is the wavenumber, a quantity widely used in spectroscopy. Equation (3.1) indicates how the frequency of the absorption should change for a strong bond (larger k values) and its dependence on the masses involved.

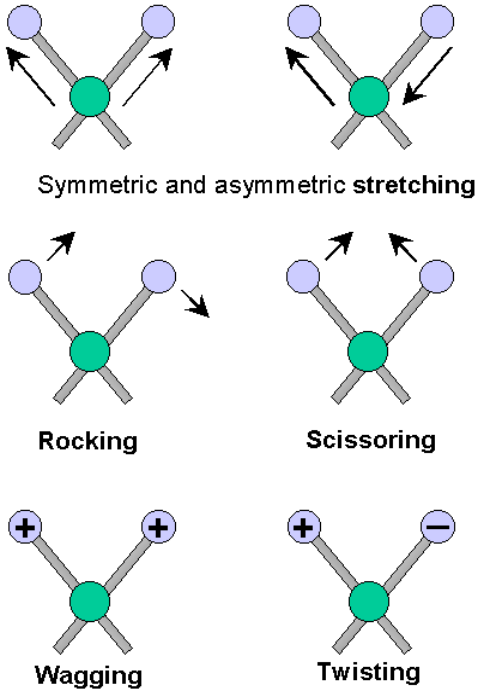


***Fig. 3.1.*** Types of infrared molecular vibrations. Arrows indicate the direction of the atomic movement; + indicates motion from page towards the reader; - indicates motion away from the reader (according to [Sko92]).

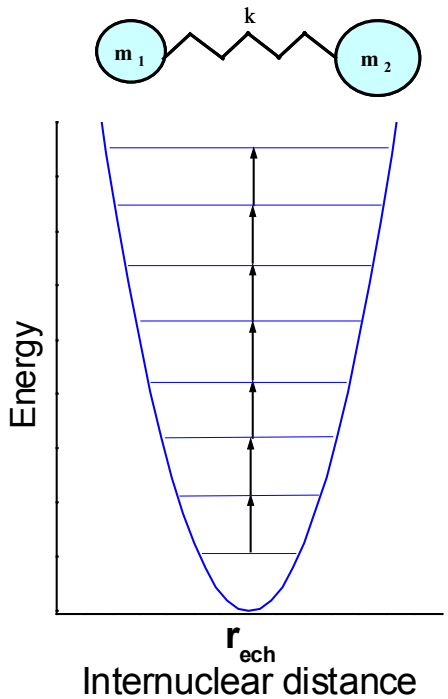


***Fig. 3.2.*** The bond energy diagram in a diatomic molecule considering harmonic oscillator model: classical treatment (parabola) and quantum treatment (energy levels and allowed transitions).

***Quantum treatment***

***a) Harmonic oscillator***. The classical mechanics do not completely describe the behaviour of particles of atomic dimensions. The quantified nature of molecular vibration energies does not appear in equation (3.1). However employing the concept of harmonic oscillator for the development of the wave equations of quantum mechanics, vibrational energies are found to be quantified by vibrational quantum number $\upsilon$ [Ban94]: $$\mathbf{E=(\upsilon+1/2)h\cdot\nu},\ (\upsilon=0,1,2) \qquad (3.2)$$

In this model the allowed vibrational levels are discrete and equidistant (horizontal lines in figure 3.2). Furthermore, quantum theory indicates that the only transitions that can take place are those in which the vibrational quantum number change by unity: $\Delta\upsilon=\pm1$ (transitions indicated by vertical arrows in figure 3.2). Since the vibrational levels are equally spaced, only a single absorption peak should be observed for a given molecular vibration.

***b) Anharmonic Oscillator***

Real molecules do not obey exactly the law of simple harmonic motion. The real bonds are not so homogeneous to follow Hooke's law; if the bond between atoms is stretched too much the molecules can dissociate into atoms.

The shape of the energy curve for a diatomic molecules can be approximated by Morse function: $\mathbf{E=E_{dis}\{1-exp[a(r_{ech}-r)]\}^2}$ where **a** is a constant and $\mathbf{E_{dis}}$ is the dissociation energy (see figure 3.3a). For anharmonic oscillations the vibrational energy can be quantified as follow [Ban94]:

$$\mathbf{E=(\upsilon+1/2)h\cdot\nu\ [1-x_e(\upsilon+1/2)]} \qquad (3.3)$$

where $x_e$ is the anharmonicity constant. Anharmonicity leads to deviation of two kinds: at higher quantum numbers, $\Delta E$ becomes smaller (see the energy levels in figure 3.3 a) and the selection rule is not rigorously followed; transitions of $\Delta\upsilon=\pm2;\ \pm3$ are also observed. Such transitions are responsible for the appearance of overtone lines at frequencies approximately two or three times larger than the fundamental frequency. Infrared spectra are further complicated by the fact that different vibrations in a molecule can interact giving absorption features at frequencies which are equal to the sum or the difference of the fundamental frequencies. The intensity of overtones and combination absorption peaks is generally low.

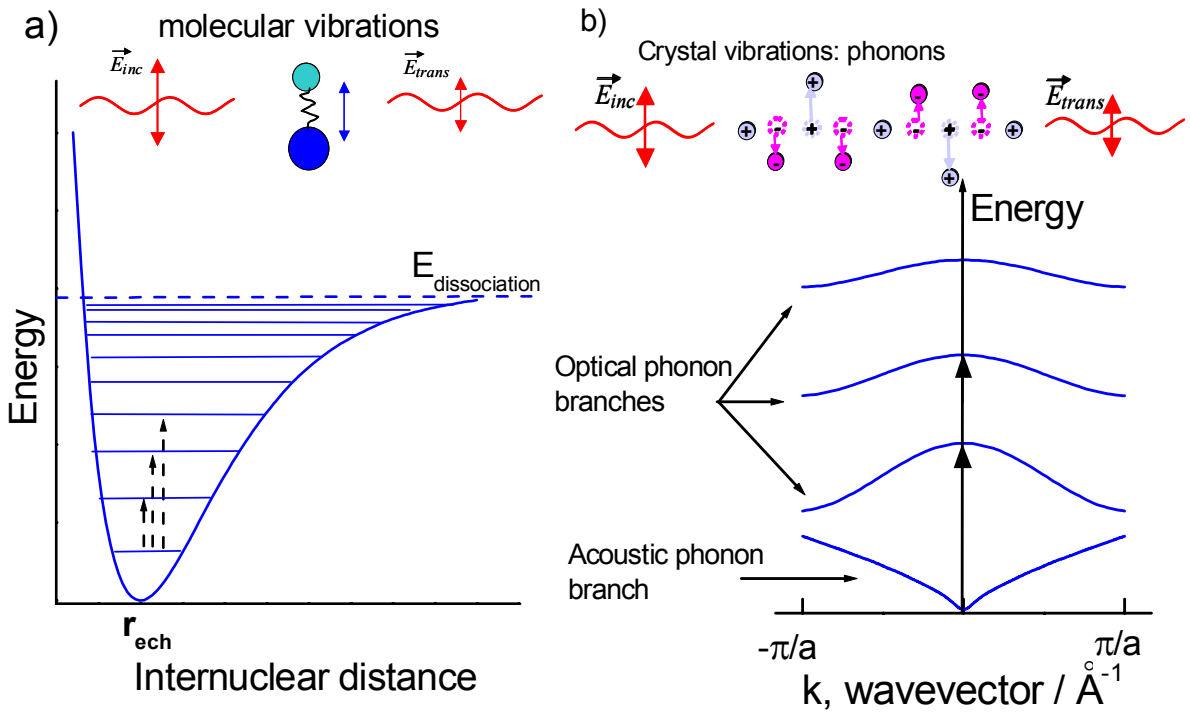


***Fig. 3.3.*** Energy diagram for a diatomic molecule considering the model of anharmonic oscillator (a).The phonon dispersion curves showing by arrows the allowed vibrational transitions between the phonon levels in the reduce-zone scheme according to [Hir02]. (b)

### *Phonons*

In solids besides the molecular vibrations, other vibrations consisting of displacements of atom chains can appear (top of figure 3.3 b). These collective vibrations are called phonons and have a specific frequency. Phonon dispersion curves, which plot energy E versus wavevector **k**, are used to represent the allowed vibrational energies (bottom of figure 3.3b) [Hir02]. Since IR photons have low energy and no mass, their momentum is small compared to that of vibrations in solids. Therefore the excited state created after IR absorption has the same momentum as the initial state. So, only “vertical transitions” between occupied and unoccupied states in the phonon dispersion curves are allowed as shown by vertical arrows in the diagram in figure 3.3 b.

Acoustical phonons correspond to the displacements of the nuclei when a sound wave propagates through the sample, and optical phonons correspond to phonons that can be created by absorption of photons. The phonons can be classified as ***transverse*** acoustical and optical (TA and TO) according to their displacements being perpendicular to the direction of the wavevector **k**, or

***longitudinal*** acoustical and optical (LA and LO) when the displacements are parallel with **k**. In a Si crystal the two atoms in the unit cell are identical, the bonding is purely covalent and the two atoms do not carry charge so that the Si TO phonon is not infrared active. However, Si absorbs in infrared due to multiphonon lattice absorption [Yu99].

***Berreman effect***

In the present work, the LO and TO features of silicon oxide thin films will be analysed. In a thin film there are two normal modes having wavelengths much greater than the film thickness [Ber63]. In one mode the vibrations are parallel to the film surface (TO mode in figure 3.4). In the other vibrations are normal to the film surface (LO mode in figure 3.4). For normal incidence the electric field can couple only with TO modes because the electric field is parallel with the film surface.

In the case of oblique incidence and for p-polarisation the electric field has both a normal and a tangential component relative to the surface of the sample. For a geometry like that plotted in figure 3.4 and in the case of p-polarisation the IR absorption was found to be [Bau96]:

$$(\Delta I)_p \sim \left[ \frac{\varepsilon_s - \sin^2\theta}{|\varepsilon_s|} \cdot \mathrm{Im}(\varepsilon_f) + \sin^2\theta \cdot \mathrm{Im}(-1/\varepsilon_f) \right] \qquad (3.4)$$

where $\theta$ is the incidence angle, $\varepsilon_f$ and $\varepsilon_s$ are the dielectric constants of the film and substrate, respectively. Considering a free standing film ($\varepsilon_s$=1) the absorption modes will be recorded at those frequencies where the imaginary part of the film dielectric function reaches its maximum (TO modes). Additional structures are observed at frequencies where Im ($-1/\varepsilon_f$) has a maximum, thus at the minimum of the dielectric function (LO modes). The geometrical configuration of transmission or reflection of p-polarised IR light in oblique incidence allow the simultaneous detection of TO and LO modes. This effect was first described by Berreman [Ber63]. The TO modes alone can be recorded using s-polarisation for the incident light.

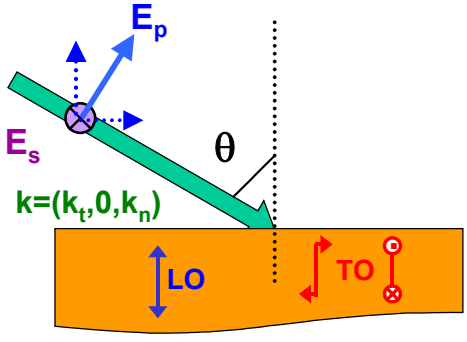


***Fig. 3.4.*** Electric field for s- and p-polarisation. TO and LO modes.

### 3.1.2. Fourier Transform Infrared Spectroscopy. Experimental set-up

In the visible and ultraviolet (UV) range optical spectroscopy usually employs monochromators with dispersive elements in order to obtain monochromatic light from a broad-band light source. Most of the infrared spectrometers, however, are based on two-beam Michelson interferometers (see figure 3.5) and the measurements are performed using Fourier transformation. The principle of Fourier Transform Infrared (FTIR) spectroscopy and its advantages will be discussed in this section.

The Michelson interferometer is a device that divides a beam into two parts and then recombines them after a path difference has been introduced. The radiation from a "white light" source is divided into two parts by a beamsplitter. This is a semitransparent material which reflects ≈50% of the radiation falling on it and transmits the rest. After reflection from a fixed and a movable mirror, respectively, the two beams are recombined at the beamsplitter position: half of the beam returns to the source and the other half after interaction with the sample is focused onto a detector. For different positions of the moving mirror the two beams have different phase shifts with respect to each other. What the spectrometer measures is the signal as a function of the path difference (retardation) $\delta$ between the two beams. This curve I($\delta$) is called interferogram. An example of an interferogram is shown on the left side of figure 3.6. Depending on the retardation induced by the moving mirror the beams can constructively or destructively interfere. The maximum of the interferogram corresponds to equal distances of the two mirrors to the beamsplitter which causes constructive interference for all wavelengths. For this reason the peak is called white light position (WLP) [Bau96].

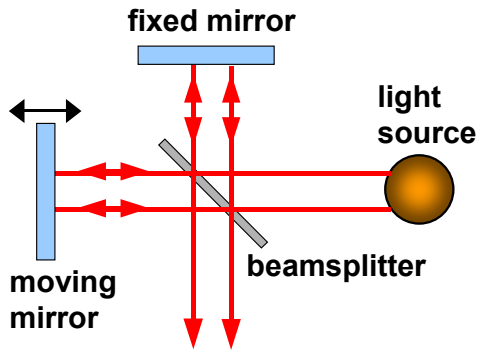


***Fig. 3.5.*** Scheme of a Michelson interferometer.

The desired spectrum in the frequency domain is the Fourier transform of the interferogram [Gri86]: $I(\bar{\upsilon}) = \int I(\bar{\delta}) \exp(-2\pi i \bar{\upsilon} \delta) d\delta$. On the right side of figure 3.6 the

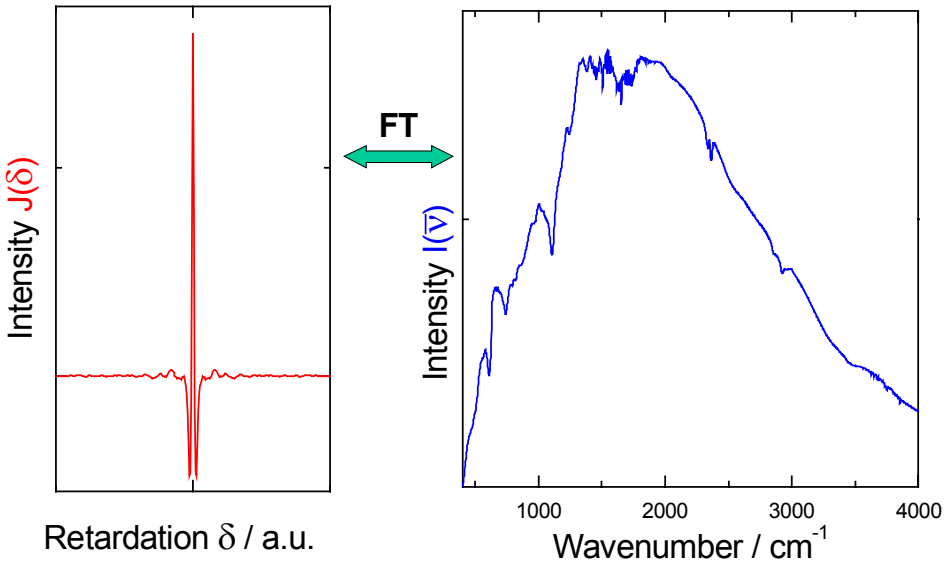


***Fig. 3.6.*** A typical interferogram (left) and the corresponding spectrum obtained by Fourier transformation (right)

spectrum corresponding to the interferogram from the left side is shown. Due to the Fourier transformation a narrow white light position corresponds to a broad frequency distribution of the IR light while a broad interferogram is generated by a narrow frequency distribution. The spectral resolution in a FTIR spectrum is determined by the inverse of the total path of the movable mirror.

The IR spectra shown in this work are measured by means of a Bruker FTIR IFS 66 spectrometer. The set-up of this spectrometer is schematically presented in the figure 3.7. The IR source used is a Globar: an electrically heated silicon carbide rod. For the measurements performed in the mid infrared range (400-4000 $cm^{-1}$) a beam splitter made of KBr is used. For transmission and reflection measurements a deuterated triglycine sulphate (DTGS) detector is employed. DTGS is a pyroelectric detector which is sensitive in the mid infrared range. For Multiple Internal Transmission (MIT) measurements for which the signal is relatively low

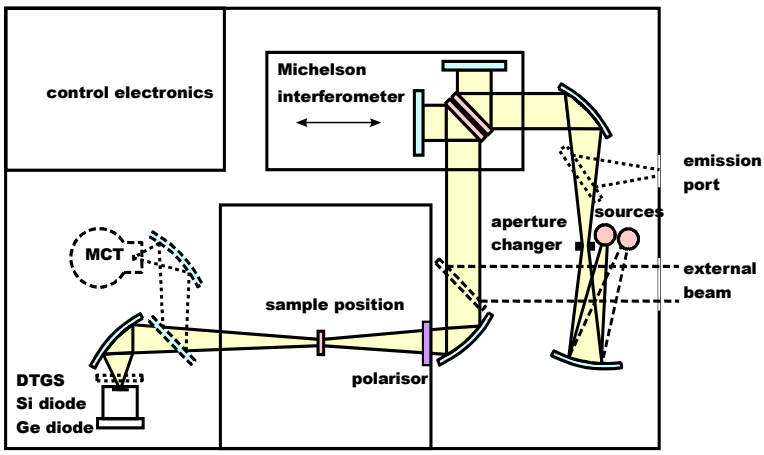


***Fig. 3.7.*** Schematic diagram of FTIR set-up for the Bruker IFS-66 spectrometer

(due to Si multiphonon absorption), a sensitive Mercury Cadmium Telluride (MCT) detector is employed. MCT can be used above 650 $cm^{-1}$, operates at liquid nitrogen temperature, which reduces the noise, and has a faster response and a better sensitivity than DTGS.

FTIR spectroscopy has the following advantages in comparison with the dispersive instruments [Ban94]:

1. *Multiplex advantage*- the total scanning time for FTIR is less than that needed by a dispersive instrument to measure a spectrum of the same sensitivity and resolution. This is due to the fact that in FTIR all the frequencies are measured at once.
2. *Throughput advantage*: since no slit is necessary in FTIR large apertures can be used.
3. *Precision*: The resolution of a FTIR spectrometers is related to the maximum mirror path by the equation: $\Delta\overline{\upsilon} = 1/\delta$ where $\Delta\overline{\upsilon}$ is the resolution and $\delta$ is the maximum path of the mirror. The position of the moving mirror is measured by counting interference fringes from a laser. Knowing the frequency of the laser with great precision, it is possible to measure the mirror position very accurately.

### 3.1.3. Multiple Internal Transmission

Infrared spectroscopy is a powerful technique to probe the chemical reactions and the chemical composition at semiconductor surfaces and interfaces. If polarized light is used, important structural information can also be obtained. In spite of all the advantages of this technique some experimental difficulties have limited the application of IR spectroscopy. Because IR wavelengths are much larger than the characteristic thickness of thin films, IR spectroscopy probes both surface and bulk vibrations. So, the absorption by surface vibrations is often covered by the stronger absorption generated by the substrate vibrations. In other cases even if the substrate is an IR transparent material, the vibrations in a film having thickness in the monolayer range are difficult to be detected using traditional reflection and transmission geometries.

To overcome the sensitivity problem special geometries, such as Attenuated Total Reflection (ATR) (figure 3.8. a) and Multiple Internal Reflection (MIR) (figure 3.8. b) are often used to enhance the detection of vibrational modes in thin films. ATR geometry is based on a trapezoidal crystal with relatively high refractive index. This crystal is in intimate optical contact with the sample under study. The IR radiation enters into the crystal and is several times internally reflected until it exits at the other end. The internal reflections create an evanescent wave, which extends beyond the surface of the crystal into the sample placed on its surface. Part of the radiation is absorbed by the sample, the IR absorption intensity being proportional with the number of reflections of the IR beam in the crystal. A modified ATR geometry is the MIR geometry shown in the figure 3.8.b. In this case the ATR crystal is the substrate itself. By means of these geometries, using a large number of passes these methods are sensitive down to submonolayer coverage on the surfaces.

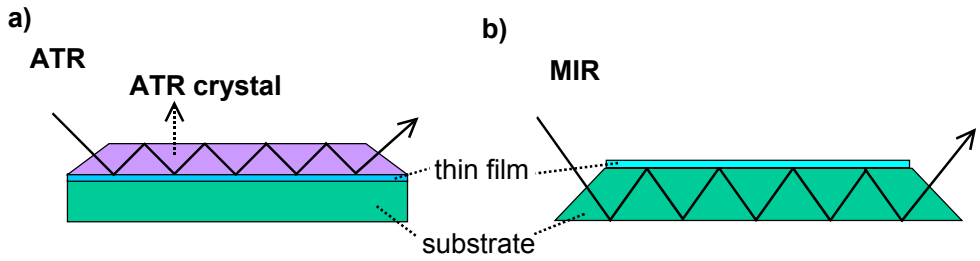


***Fig. 3.8.*** Schematical representation of Attenuated Total Reflection (ATR) and Multiple Internal Reflection (MIR) geometries.

The ATR technique was extended to study buried interfaces in its variant Multiple Internal Transmission (MIT). This geometry was successfully applied for characterization of the buried interface of two silicon bonded wafers [Fei94, Wel96a, Rei95, Mil00] and GaAs bonded wafers [Han01]. This geometry is schematically shown in the figure 3.9 a. The IR radiation enters into the system through the beveled edges of the Si-Si bonded wafers and is total internally reflected at the outer surfaces. The radiation is transmitted through the interface rather than reflected, even under angular conditions where total internal reflection is observed for bulk media, because the interface is much thinner than the wavelength leading to "tunneling" [Wel96b]. In this way the IR response of the interface is strongly enhanced due to the manifold interaction of the IR light with the buried interface.

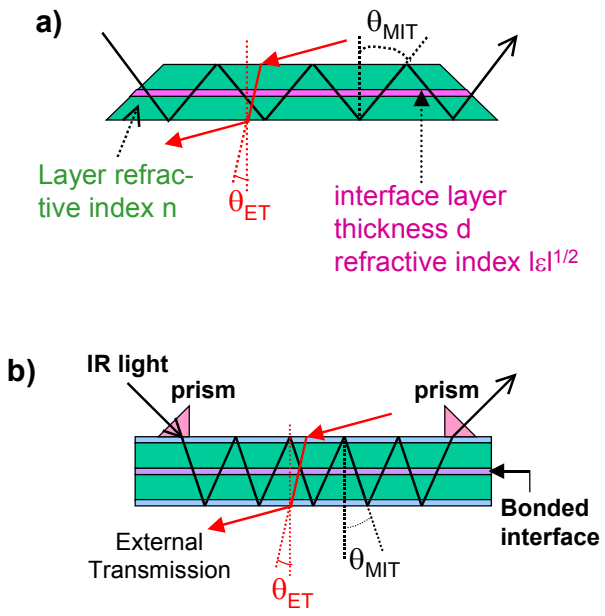


***Fig. 3.9.*** Multiple Internal Transmission geometries used by Chabal and co-workers [Cha95, Wel96a,b] (a) and in our laboratory (b) to study the bonded interface in Si-Si bonded wafers. The path of the light in the case of external transmission (ET) is also plotted.

In our laboratory a modified MIT geometry using two-coupling prisms was employed for the investigation of interfaces in Si-Si bonded wafers [Mil99, Mil00]. This MIT configuration is schematically presented in figure 3.9.b. A picture of the experimental set-up used for *ex situ* MIT measurements is shown in figure 3.10. Two prisms made of an IR transparent material (KRS5 or ZnSe) are gently pressed onto the surface of the Si wafer in order to get an intimate optical contact. The shape of the prisms is plotted in the right-down corner in figure 3.10. The IR light enters in the Si-Si bonded system via one prism, undergoes multiple internal reflection in the sandwiched structure (the thin bonded interface is tunnelled) and is guided out from the system by the second prism. The faces of the prisms are optically polished which allows a good and reproducible optic contact between the prism and the wafer by applying a slight pressure. KRS5 prisms with an angle $\alpha$ = 62° (providing an internal angle of 38°) were employed and the distance

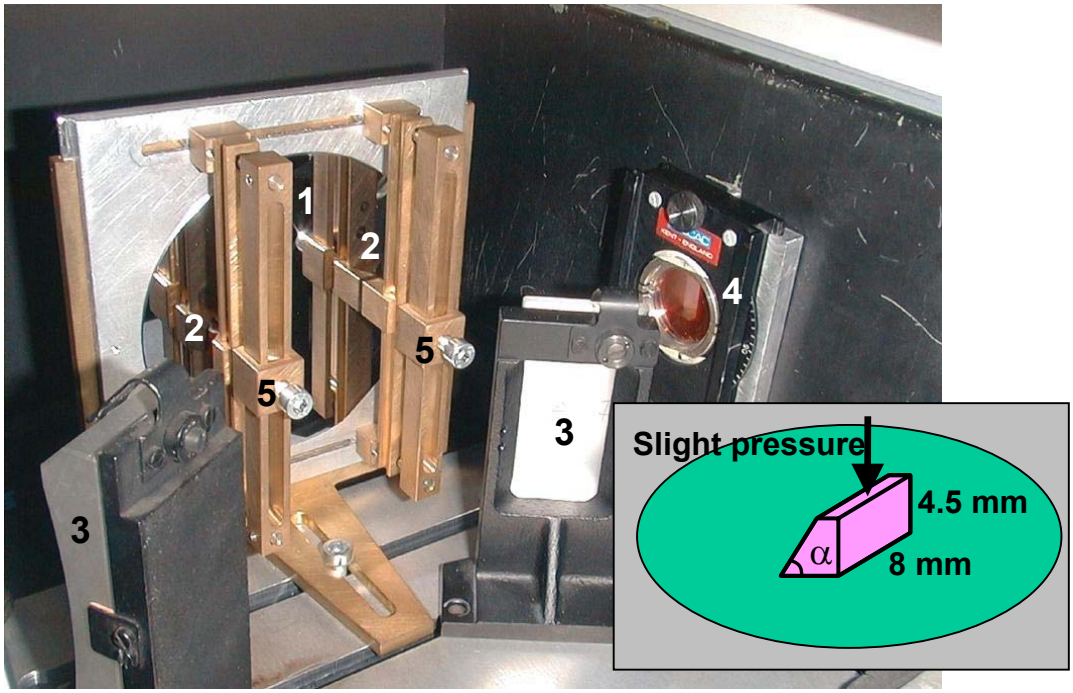


***Fig. 3.10.*** Picture of the set-up used for *ex situ* MIT measurements: the wafer (1), the prisms (2), the mirrors for alignment (3) the polariser (4) and the screws (5) for adjusting the optical contact prism-wafer are indicated on the picture.

between the prisms can be varied between 20 and 70 mm which corresponds to ~ 30 up to 100 passes of the IR light through the interface.

In contrast to the MIT geometry introduced by Chabal and the co-workers [Wel96a, Fei94] which uses cut bevels on the Si-Si bonded wafers the configuration employed in this work does not require additional sample preparation and is thus completely non-destructive. This is advantageous especially for RT bonded wafers where the cutting and polishing of the bevels can induce debonding of the wafers. Another advantage of our geometry is that the distance between the prisms can easily be varied and in this way different regions of the interface probed by the IR radiation can be studied.

In figure 3.11 a transmission IR spectrum of a Si-Si bonded wafer is plotted together with the MIT spectrum for the same sample. It can be seen that the MIT spectrum provides complementary information to the external transmission (ET) spectrum. ET gives valuable information about the structure of the oxide at the interface in the region of optical phonons in silicon oxide [Que00, Him01a]. On the other hand, using ET the chemistry of the interface (region above 1500 $cm^{-1}$) cannot be studied due to the low sensitivity. The solution for detection of H containing

species from the buried interface is to use the MIT geometry. In the MIT spectrum the features corresponding to Si-H stretching vibrations at the $Si/SiO_2$ interface (2100 $cm^{-1}$) or in the oxide layer (2270 $cm^{-1}$) and the absorption features of O-H stretching vibrations in water molecules (broad band centred at 3400 $cm^{-1}$) and in isolated silanol species (3740 $cm^{-1}$) can clearly be observed.

Chabal [Cha88] showed that the absorption for p-polarisation in the case of transmission of the IR light through a three-layer system is:

$$\left(\frac{\Delta I}{I_0}\right)_p = \frac{2\pi d}{\lambda}\cdot\frac{1}{2\cos(\theta)}\left[\cos^2(\theta)\,\mathrm{Im}(\tilde{\varepsilon}) + n^4\sin^2(\theta)\,\mathrm{Im}\left(\frac{-1}{\tilde{\varepsilon}}\right)\right] \qquad (3.5)$$

where $(\Delta I/I_0)$ is the absorption, $\theta$ is the internal angle, d and $\tilde{\varepsilon}$ are the thickness and the dielectric constant of the interface layer. The absorption is divided into two terms: one proportional to the imaginary part of $\tilde{\varepsilon}$ and the other to the imaginary part of $-1/\tilde{\varepsilon}$, which describe the component of absorption parallel and normal to the interface, respectively [Cha95]. Considering equation (3.5) the component of absorption normal to the interface is enhanced in respect to the parallel component by a factor:

$$\frac{\Delta I_\perp}{\Delta I_{II}} = \frac{n^4\sin^2(\theta)}{|\tilde{\varepsilon}^2|\cos^2(\theta)} \qquad (3.6.)$$

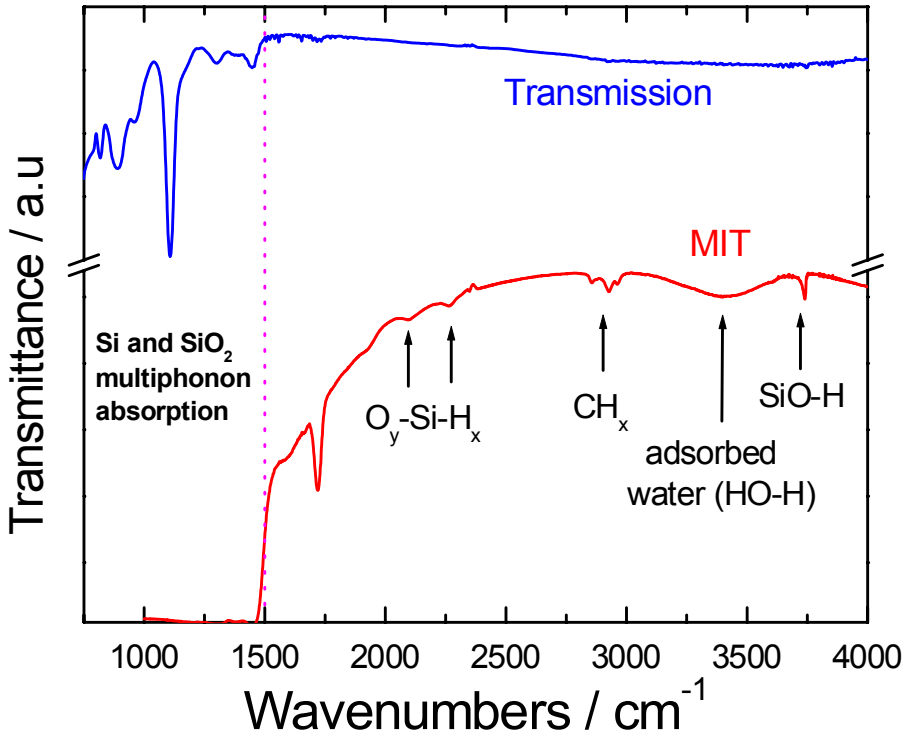


***Fig. 3.11.*** IR external transmission (ET) spectrum and the corresponding multiple internal transmission spectrum for a Si-Si bonded wafer.

In the case of external transmission (ET) the internal angle $\theta$ can never be larger than $sin^{-1}(1/n)$. This means for silicon ($n_{Si}$=3.42) $(\theta_{ET})_{max} \approx 17°$. Considering that for the silicon oxide interfacial layer we have $\left|\tilde{\varepsilon}\right|^{1/2} \approx 1.3$ [Wel96b] the enhancement factor given by equation (3.6) in the case of external transmission is ~7.5. In the case of MIT geometry the internal angle in our experiments is ~38° which gives an ***enhancement factor per pass*** of ~50.

The ratio between the sensitivity of the MIT geometry and that of the ET geometry for the components of absorbance perpendicular to the interface is enhanced by the following factor:

$$\left(\frac{\Delta I_{MIT}}{\Delta I_{ET}}\right)_{\perp} = N\frac{\sin^2\theta_{MIT}}{\sin^2\theta_{ET}}\frac{\cos\theta_{ET}}{\cos\theta_{MIT}} \tag{3.7}$$

where N is the number of passes and $\theta_{MIT}$ and $\theta_{ET}$ are the internal angles for MIT and ET, respectively (as plotted in figure 3.9). In this case $\theta_{MIT}$~38° and considering that $\theta_{ET}$=16.3° for external transmission at the Brewster angle we obtain an enhancement of perpendicular absorption of ~5.4 per pass for MIT compared with the ET geometry. Under these conditions considering the number of passes we obtain that the sensitivity of MIT is larger by more than 2 orders of magnitude compared with the sensitivity of ET for the absorption perpendicular to the interface. This fact provides the reason for using p-polarised light. Another reason is that p-polarised light interacts with the bonds normal to the interface which are more involved in the bonding mechanism. In the MIT spectrum of figure 3.11 the absorption features of the chemical species at the interface can easily be seen, while the region below 1500 $cm^{-1}$ becomes practically opaque due to Si multiphonon absorption.

Another advantage of the two-coupling prisms MIT geometry is that using prisms with different angles made of different materials (KRS5, ZnSe, Si, Ge) the internal angle $\theta_{MIT}$ can be tuned so that the sensitivity ratio $(\Delta I_{MIT}/\Delta I_{ET})_{\perp}$ can be further improved. It was also found [Wel96b] that the sensitivity of the MIT configuration is 20 times that of the traditional MIR. Considering these enhancement factors the interpretation of MIT spectra for p-polarisation is straightforward: the outer surface absorption are negligible compared to the perpendicular component of the interface absorption.

### 3.1.4. Heating chamber for *in situ* MIT measurements

Part of the room temperature Si-Si bonded wafers were further annealed in a small home built low-vacuum annealing chamber placed in the air-purge box of the spectrometer. Pictures of the experimental set-up used are shown in the figure 3.12: heating plate and MIT configuration (a) and the chamber with the electrical and vacuum connectors (b). The IR light coming from the spectrometer is polarized by the polariser (1) and guided by the mirror (2) through the IR windows (3) on the first prism (4). The windows are made of $CaF_2$, which is an material transparent above 1500 $cm^{-1}$. The prisms are made of ZnSe and have an angle $\alpha$=60° which provide the same internal angle $\theta_{MIT}$=38° as KRS5 62° prisms used for *ex situ* measurements. KRS5 prisms were not used for measurements during annealing for safety reasons (KRS5 material contains thallium which can be evaporated during annealing). ZnSe was the best material for annealing up to 400°C considering its mechanical, thermal and optical properties. The prisms (4) will couple the light inside the Si-Si bonded wafer (5). The IR light will be internal reflected several times in the sample until the second prism (4') will guide the light out of the sample. The light will be further transmitted through the windows (3') and by reflection on the mirror (2') directed to the detector.

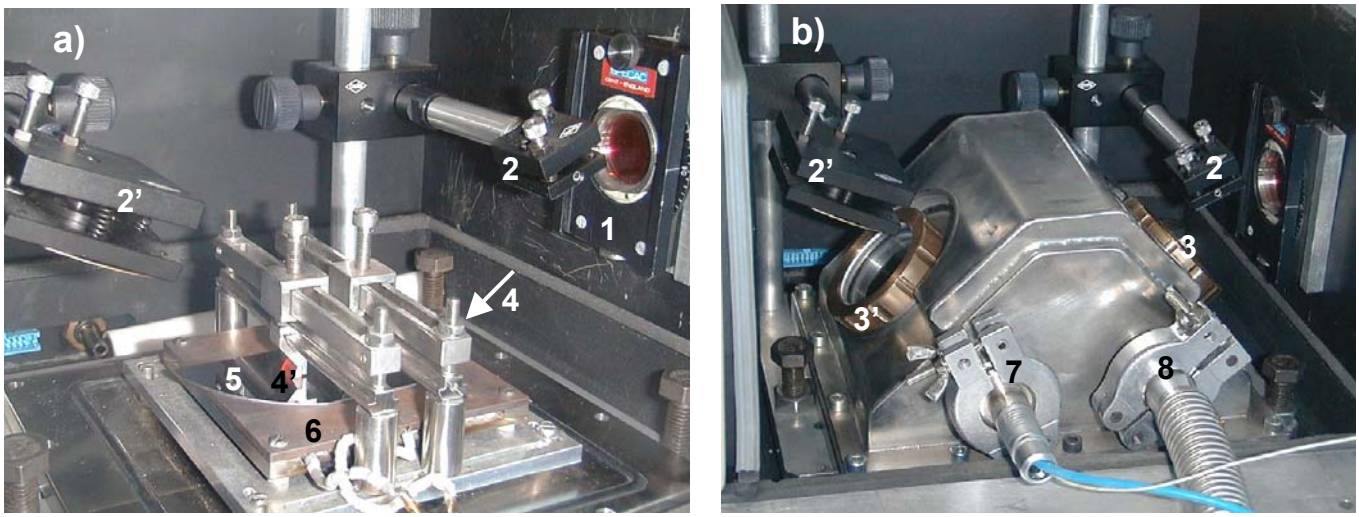


***Fig. 3.12.*** Experimental set-up for *in situ* MIT measurements: MIT geometry and heating plate (a); annealing low-vacuum chamber (b).

As can be seen in the pictures, the mirrors are adjustable by screws that allow a good alignment of the light into the system. The heating plate (6) can be electrically heated by a current applied through the connector (7). The same connector allows

the measurement of the temperature using a thermocouple which is placed on the heating plate. The temperature was calibrated prior the measurements. A vacuum of ~ $5 \cdot 10^{-3}$ mbar is realised in the chamber by a mechanical pump connected to the system by the vacuum connector (8). The experimental set-up presented above allows to record IR spectra for the RT bonded samples during annealing. This makes a real-time monitoring of the chemical species present at the interface and their evolution with annealing temperature possible. For the doping level of the present Si wafers the IR radiation is totally absorbed by free carriers at temperatures higher than 230°C. The MIT configuration we applied should also work at higher temperatures for samples produced using semi-insulating Si wafers. However, even for the doping concentration of the samples under study the MIT geometry used allowed the monitoring of the chemical species and the understanding of the bonding mechanism up to temperature slightly above 200°C, which is the temperature range desired for technical applications.

# 3.2. Variable Angle Spectroscopic Ellipsometry

## 3.2.1. Principles. Experimental set-up

Spectroscopic ellipsometry is an optical technique which measures the changes of the polarization state of a polarized light beam after reflection from the sample under study (see figure 3.13). The change is measured by the ellipsometric parameters $\psi$ and $\Delta$. $\psi$ is the ratio of the amplitudes of the Fresnel reflection coefficients for the electric field component with polarization in the plane of incidence (p-polarization) to that with polarization perpendicular to the plane of incidence (s-polarization). $\Delta$ is the phase retardation between the two Fresnel reflection coefficients $r_p$ and $r_s$. The ratio $\rho$ of these reflection coefficients is measured by the ellipsometer [Azz92]:

$$\rho = \frac{r_p}{r_s} = \tan\psi \cdot e^{i\Delta} \tag{3.8}$$

Changes in $\psi$ and $\Delta$ depend on the thickness, roughness, porosity, refractive index (n), extinction coefficient (k) of the layers and substrate. For a given sample, the magnitude of the change in $\psi$ and $\Delta$ is different at different angles of incidence [Sun02a]. A larger change gives more accurate results, and for this reason data are usually taken at various incident angles to find the angles that give the biggest change in $\psi$ and $\Delta$. For semiconductor materials most precision can be acquired at angles around the Brewster angle. Variable Angle Spectroscopic Ellipsometry (VASE) uses a large number of angles and wavelengths for data acquisition in order to improve the analysis precision.

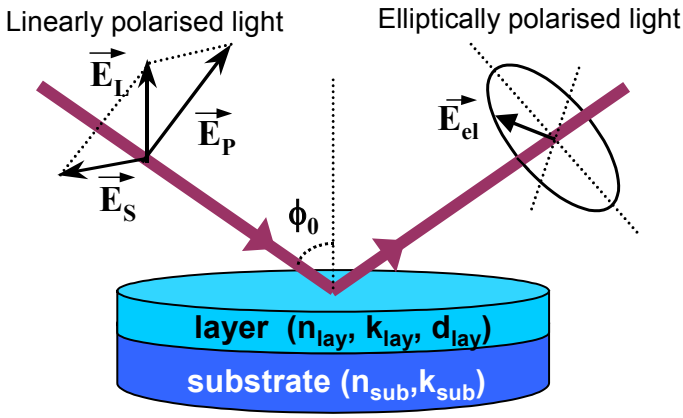


***Fig. 3.13.*** Interaction of linear polarized light with a sample.

The ellipsometric $\psi$ and $\Delta$ data measured on a sample can be directly converted into the *pseudo*-optical constants or *pseudo*-dielectric function <ε> of the sample as follows [Woo99]:

$$\langle\varepsilon\rangle = \langle\varepsilon_1\rangle + i\langle\varepsilon_2\rangle = \left(\langle n\rangle + i\langle k\rangle\right)^2 = \sin(\phi)\cdot\left[1+\tan(\phi)^2\cdot\left(\frac{1-\rho}{1+\rho}\right)^2\right] \tag{3.9}$$

where $<\varepsilon_1>$ and $<\varepsilon_2>$ are the real and imaginary part of the *pseudo*-dielectric function; <n> and <k> are the *pseudo* refractive index and *pseudo* extinction coefficient and $\phi$ is the incidence angle. These quantities are called *pseudo* because they are not a property of a certain material, but describe the average properties of the sample in the region penetrated by the light.

***Fig. 3.14.*** Woollam VASE Ellipsometer. Optical fiber (1), polarizer (2), sample (3), analyser (4) and autoretarder (5) are marked on the picture by numbers.

The Ellipsometric measurements presented in this work were measured using a rotating analyzer VASE Woollam ellipsometer (see figure 3.14). The light (250-1700 nm spectral range) from a short arc xenon lamp is guided through an optical fiber (1) from a monochromator to the input polarizer unit (2). The changes in the polarization of the linearly polarized light will be analyzed by the rotating analyzer (4) in terms of $\psi$ and $\Delta$ ellipsometric parameters after reflection on the sample (3). An automatic $\psi$ and $\Delta$ spectroscopic scan can be realized at different angles of

incidence. The precision in measuring the incidence angle is 0.01°. Using this type of ellipsometer the "handedness" of the ellipsometric Δ parameter cannot be determined. Δ can range from 0° to 360° but for Δ>180° the system will report $\Delta_{meas}=360°-\Delta_{real}$. In this way the values for the measured Δ are between 0° and 180°, so there is no distinction between left and right handed polarization.

This disadvantage was overcome in December 2001 by upgrading the VASE system with an autoretarder (5). This device changes the input polarization state to well known polarizations. By measurements with multiple input conditions, the resulting data have maximum confidence and Δ can be accurately measured between 0° and 360° (or any other interval of a length of 360°). In figure 3.15 we present Δ ellipsometric spectra for a xerogel film on a Si substrate measured without (woAR) and with autoretarder (AR). We can observe the mirroring of the spectra by the line Δ=180° which indicates that $\Delta_{woAR}=360°-\Delta_{AR}$ for Δ>180°.

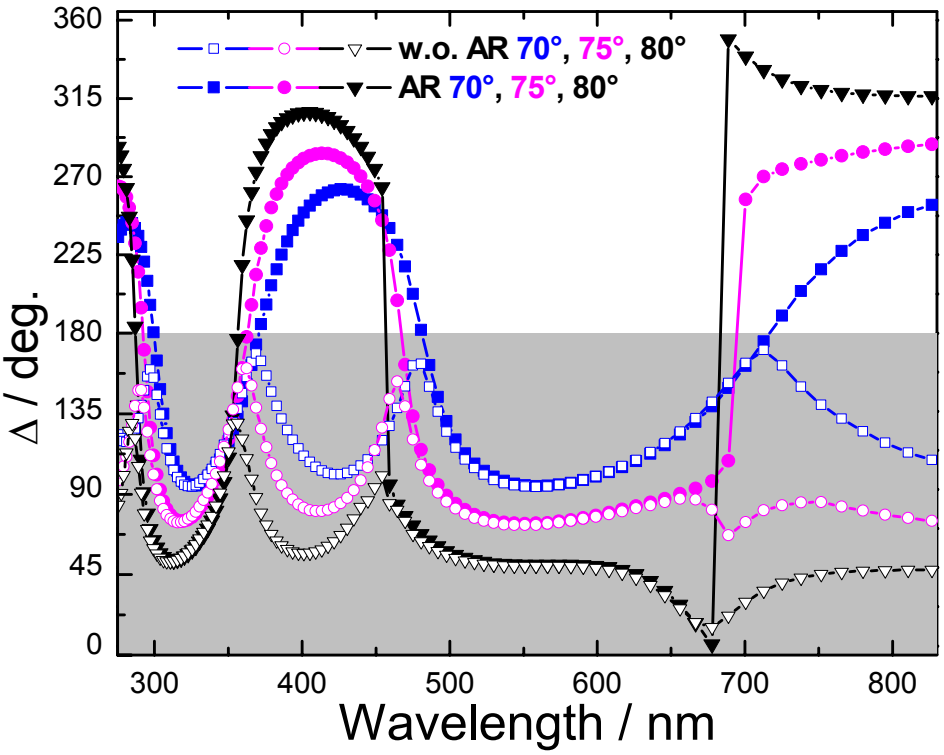


***Fig. 3.15.*** Δ ellipsometric spectra for a xerogel film on Si sample measured without (open symbols) and with (filled symbols) autoretarder.

To extract useful information about a sample (thickness, optical constants, roughness of the layers) the experimental data must be compared with the data generated using a model which describes the optical response of the sample. The algorithm for analyzing the VASE data is schematically presented in figure 3.16.

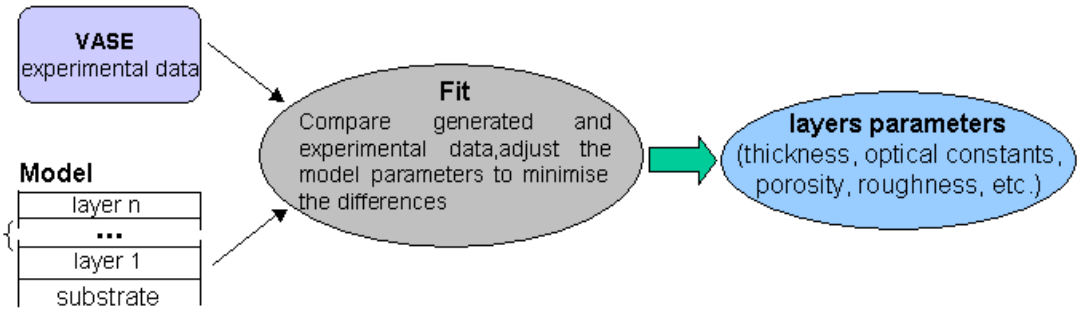


***Fig. 3.16.*** Analysis procedure for VASE data.

Analytic expressions (Fresnel equations applied to the assumed model) can be written for predicting $\psi$ and $\Delta$ as a function of optical constants and thicknesses of the layers. The expression of calculating $\psi$ and $\Delta$ will be not presented here, but can be found in standard references [Azz92]. In the case of complex material systems, a matrix multiplication procedure is used, each layer and boundary being represented by a matrix. The software WVASE [Joh95] is capable to do the matrix multiplications, predicting the ellipsometric data for a multilayer structure.

The unknown parameters in the model are adjusted in order to get the best fit between the model and the experimental data. The algorithm of doing this fit is to minimize the Mean Square Error (MSE) value which is used to quantify the differences between the experimental and predicted data [Woo99]:

$$MSE = \sqrt{\frac{1}{2N-M} \cdot \sum_{i=1}^{N} \left[ \left( \frac{\psi_i^{\mathrm{mod}} - \psi_i^{\mathrm{exp}}}{\sigma_{\psi,i}^{\mathrm{exp}}} \right)^2 + \left( \frac{\Delta_i^{\mathrm{mod}} - \Delta_i^{\mathrm{exp}}}{\sigma_{\Delta,i}^{\mathrm{exp}}} \right)^2 \right]} \qquad (3.10)$$

where N is the number of measured $\psi$ and $\Delta$ pairs, M is the number of fit parameters, $\sigma_\psi^{exp}$ and $\sigma_\Delta^{exp}$ are the standard deviations of the experimental data points. From equation (3.10) it can be seen that noisy measurements with corresponding large standard deviation will not be strongly weighted in the fit.

## 3.2.2. Models for data evaluation

To extract material properties from the analysis of VASE data it is very important to build a model which describes the optical response of the sample and have enough flexibility to accurately fit the experimental data [Joh95].

*Cauchy dispersion relation*

For the parametrization of the refractive index of transparent materials the Cauchy dispersion relation is well suited:

$$n(\lambda) = A_n + \frac{B_n}{\lambda^2} + \frac{C_n}{\lambda^4} + \cdots \tag{3.11}$$

where $A_n$, $B_n$, $C_n$, are constants which can be fit parameters. Some of the xerogel samples under study in this work absorb radiation at the UV edge of the spectrum. The optical response of these samples has been modeled by adding to the Cauchy dispersion an *Urbach absorption relation* [Joh95]:

$$k(\lambda) = A_k \cdot \exp\left[ B_k \left( \frac{1}{\lambda} - \frac{1}{C_k} \right) \right] \tag{3.12}$$

where $A_k$, $B_k$ and $C_k$ are constants with $C_k$ representing the band edge.

*Effective Medium Approximations*

For the determination of porosity in the xerogel films, which are a mixture of silicon oxide and voids, Effective Medium Approximation (EMA) models were employed. EMA models are the most appropriate tool to calculate optical constants of heterogeneous materials which are mixtures of constituents of different optical constants [Ohw97]. For light waves with wavelengths much longer than the dimensions of the inhomogeneities the heterogeneous materials can be treated as a homogeneous material with an effective dielectric constant $\varepsilon_{eff}$ by means of the Bergman EMA theory. In this approximation $\varepsilon_{eff}$ depends on the dielectric constants of the constituents $\varepsilon$, of the host material $\varepsilon_h$ and the topology of the system, as follow [Bau96]:

$$\varepsilon_{eff} = \varepsilon_h \left( 1 - f \int_0^1 \frac{g(f,c)}{\frac{\varepsilon_h}{\varepsilon_h - \varepsilon} - c} dc \right) \tag{3.13}$$

where *f* is the volume fraction of the component with the dielectric constant ε, c is the degree of connectivity of the component and *g(f,c)* is called spectral density and describes the topology of the system. The function *g(f,c)* is difficult to be calculated even if the topology is known and because of this, simple mixing equations as presented below can simplify the formula (3.13).

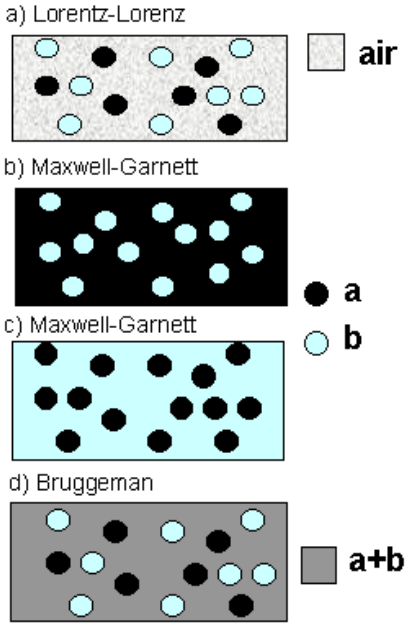


***Fig. 3.17.*** Schematic representations of effective medium theories [Ohw97].

For isotropically disordered systems consisting of two media **a** and **b** having the dielectric constants $\varepsilon_a$ and $\varepsilon_b$ embedded in a host medium with dielectric constant $\varepsilon_h$, the dielectric constant $\tilde{\varepsilon}$ can be written in the approximation of spherical inclusions as:

$$\frac{\tilde{\varepsilon}-\varepsilon_h}{\tilde{\varepsilon}+2\varepsilon_h}=f_a\cdot\frac{\varepsilon_a-\varepsilon_h}{\varepsilon_a+2\varepsilon_h}+f_b\cdot\frac{\varepsilon_b-\varepsilon_h}{\varepsilon_b+2\varepsilon_h} \qquad (3.14)$$

where $f_a$ and $f_b$ are the volume fractions of the media **a** and **b**. The approximation given by equation (3.14) has three different particular cases depending on how the components are embedded into the host matrix (figure 3.17) [Ohw97]:

*1). Lorentz-Lorenz* approximation ($\varepsilon_h$=1, figure 3.17 a) considers that the host medium is air, so that the dielectric constant $\tilde{\varepsilon}$ of the mixture can be written as:

$$\frac{\tilde{\varepsilon}-1}{\tilde{\varepsilon}+2}=f_a\cdot\frac{\varepsilon_a-1}{\varepsilon_a+2}+f_b\cdot\frac{\varepsilon_b-1}{\varepsilon_b+2} \qquad (3.15)$$

*2). Maxwell-Garnett* (figure 3.17 b and c) assumes that one of two media **a** and **b** is the host medium ($\varepsilon_h=\varepsilon_a$ or $\varepsilon_h=\varepsilon_b$). Considering as host medium the component **b**, $\tilde{\varepsilon}$ becomes:

$$\frac{\tilde{\varepsilon}-\varepsilon_b}{\tilde{\varepsilon}+2\varepsilon_b}=f_a\cdot\frac{\varepsilon_a-\varepsilon_b}{\varepsilon_a+2\varepsilon_b} \qquad (3.16)$$

3) *Bruggeman*

The Lorentz-Lorenz method cannot exclude the presence of voids and for Maxwell-Garnett approximation $\tilde{\varepsilon}$ is dependent on the choice of the host medium. To solve

this problem the *Bruggeman* theory (figure 3.17 d) assumes that the inclusions should be considered as being embedded in the effective medium itself ($\varepsilon_h = \tilde{\varepsilon}$), so neither phase should be given a preference. In these conditions $\tilde{\varepsilon}$ can be calculated using the relation:

$$0 = f_a \cdot \frac{\varepsilon_a - \tilde{\varepsilon}}{\varepsilon_a + 2\tilde{\varepsilon}} + f_b \cdot \frac{\varepsilon_b - \tilde{\varepsilon}}{\varepsilon_b + 2\tilde{\varepsilon}} \qquad (3.17)$$

Silica xerogel films consist of a porous structure which is an isotropic mixture of silicon oxide and voids, as can be seen in the Scanning Electron Microscopy (SEM) picture in figure 3.18. It should be noted that Maxwell-Garnett, Lorentz-Lorenz and Bruggeman expressions are all related and differ only in the choice of the host medium. In this work the Maxwell-Garnett approximation was preferred because it considers the xerogels as a host silica matrix with the pores "seen" as voids embedded into the matrix. For a direct comparison of VASE results with Ellipsometric Porosimetry (EP) results the Lorentz-Lorenz approximation was used because the software to treat EP data is based on this approximation. However, when using the three different EMA models described above to fit the $\psi$ and $\Delta$ ellipsometric spectra of silica xerogel films very close values (differences below 2%) were obtained for the porosity of the films $f = V_{pores}/V_{film}$ and for MSE.

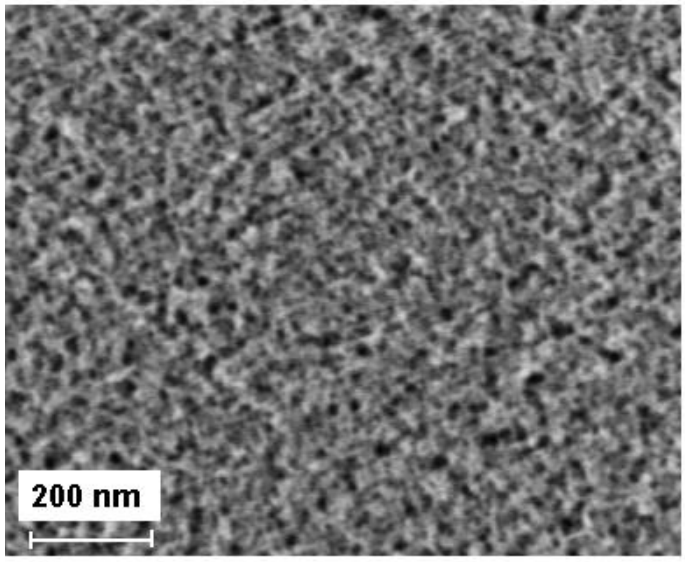


***Fig 3.18.*** SEM picture of a silica xerogel sample.

### 3.2.3. Ellipsometric Porosimetry

Ellipsometric porosimetry (EP) is a method which uses the changes of the optical characteristics of porous films during adsorption and/or desorption of an adsorbate in/from the pores, and determines the amount of the adsorbate inside the pores [Bak00a, Bak00b]. The EP results shown in this work were obtained at IMEC Leuven using an experimental set-up (figure 3.19) consisting of a high-vacuum chamber equipped with a pumping system and a source of an adsorptive liquid which allow admission of the vapors into the chamber at controllable pressure. The system is coupled with an one-wavelength ellipsometer ($\lambda$= 632.8 nm) which measures the $\psi$ and $\Delta$ values during adsorption and desorption of the adsorbent in the pores of the xerogel film.

The porosity values are determined as in the case of classical ellipsometry by using EMA models for data evaluation. Considering the Lorentz-Lorenz approximation (Eq. 3.15) the relation $\varepsilon=n^2$, and the pores being initially filled with air ($\varepsilon_b$=1) the porosity of the film can be calculated as:

$$f = 1 - \left[\frac{n_r^2 - 1}{n_r^2 + 2}\right] \Big/ \left[\frac{n_s^2 - 1}{n_s^2 + 2}\right] \qquad (3.16)$$

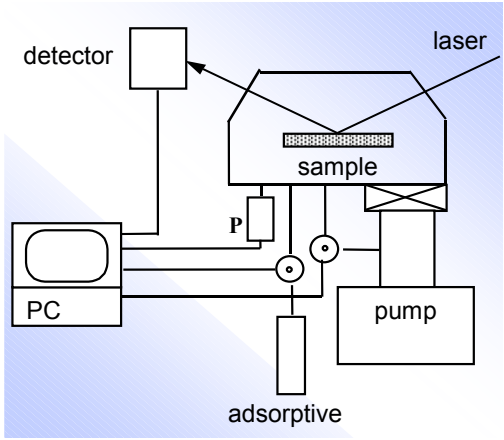


***Fig. 3.19.*** Schematic representation of the system used for EP measurements.

where $n_r$ is the measured refractive index of the porous film and $n_s$ is the refractive index of the skeleton. In the case of adsorption of a substance inside the pores the adsorptive vapors condenses in the pores even if the vapor pressure P is less than the equilibrium pressure of a flat liquid surface $P_0$ [Bak00b]. Near to the equilibrium pressure $P=P_0$, the Lorentz-Lorenz EMA model can be also applied considering that the pores are filled with an adsorptive liquid of a known refractive index. Using several adsorbents and applying Lorentz-Lorenz EMA in each case, it was found that the refractive index of the skeleton is equal with the refractive index of silica.

The dependence of the adsorptive volume on the relative pressure $P/P_0$ is an adsorption or desorption isotherm. Typical adsorption/desorption isotherms of toluene in/from a xerogel film are shown in figure 3.20.a. The porosity can be

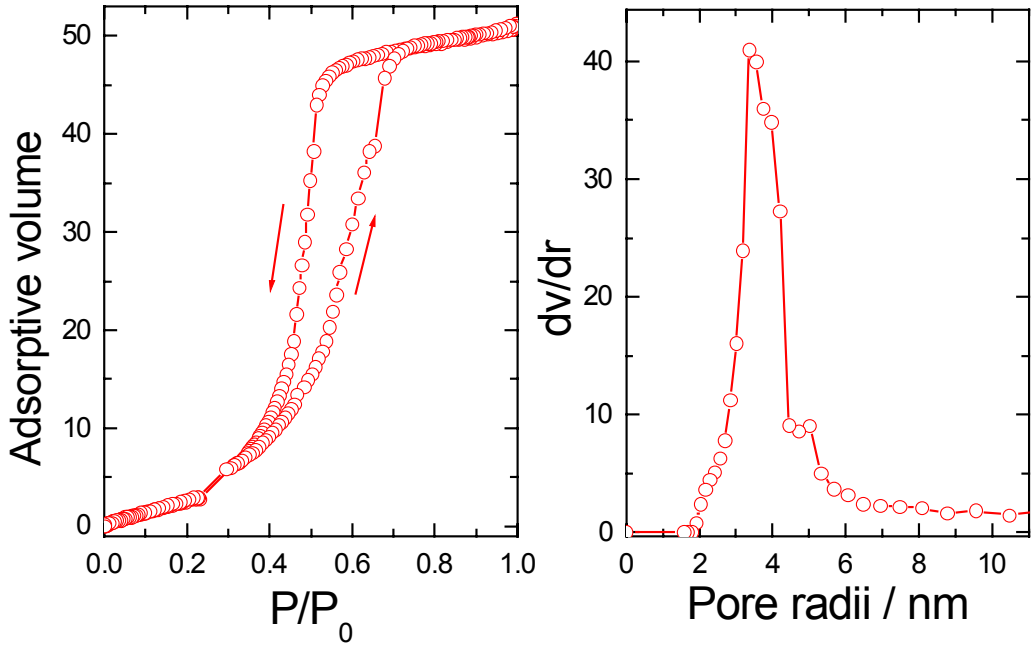


***Fig. 3.20.*** Typical adsorption and desorption isotherms of the toluene in/from the pores of a xerogel film (a) and the corresponding pore size distribution (b).

determined from the saturation values of these isotherms. The porosity determined in this way is the “open” porosity because it refers to the open pores which are accessible to the liquid adsorption. By comparing “open” porosity obtained from EP with “full” porosity obtained from VASE important information about the degree of connectivity of the pores can be obtained.

It was found that the radii of the pores, r, have a dependence on the relative pressure $P/P_0$ and can in the case of cylindrical pore be approximated by the Kelvin equation [Bak00a]:

$$\frac{2}{r} = -\frac{RT}{\gamma V_L}\ln\left(\frac{P}{P_0}\right) \tag{3.17}$$

where $\gamma$ and $V_L$ are surface tension and molar volume of the adsorbed liquid. Using Kelvin and Brauner-Emmet-Teller (BET) equations [Bak00b] the pore size distribution (PSD) can be calculated from the desorption isotherms. The calculated PSD for the desorption isotherm in figure 3.20.a is shown in figure 3.20.b.

# Chapter 4

# Properties of Si—Si bonded wafers.

## 4.1. High temperature Si—Si wafer bonding with RCA and $O_2$ plasma pretreatment.

This chapter presents an investigation of the influence of annealing on the properties of oxide layers (layer thickness, strain relaxation) which are formed at surfaces and interfaces in Si-Si wafers bonds using spectroscopic methods (ellipsometry and IR spectroscopy) and High Resolution Transmission Electron Microscopy (HRTEM). Prior to bonding the Si wafers were cleaned in RCA solution and treated by an $O_2$ plasma. After bonding the samples were annealed in nitrogen for 6h at 400°C, 800°C and 1100°C, respectively.

### 4.1.1. Determination of surface oxide thickness

The imaginary part of the pseudo-dielectric function (Im <ε>) for prebonded, i.e. room temperature bonded without any further annealing step, and 800°C and 1100°C annealed Si-Si wafer bonds is plotted in figure 4.1. The features in the spectra at 3.3 and 4.2 eV correspond to $E_1$ and $E_2$ interband critical points of Si, respectively. Annealing obviously causes changes in (Im <ε>) (red shift of $E_1$ and decrease of Im<ε> near $E_2$) that can be explained by an increasing surface silicon oxide thickness. The values for the surface oxide thickness were

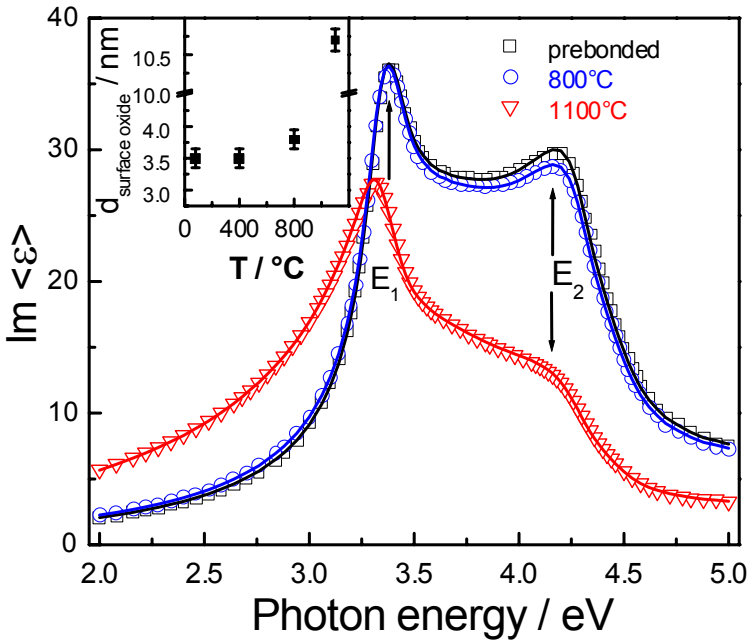


***Fig. 4.1.*** Experimental (symbols) and simulated (lines) imaginary part of the pseudo-dielectric function for Si-Si bonded wafers annealed at different temperatures. Inset shows the surface oxide thickness determined from the best fit to the experimental data.

determined from the best fit to the experimental pseudo-dielectric function spectra, by means of the WVASE 32 program [Joh95]. The pseudo-dielectric function used in the calculation considers the dependence of Fresnel reflection coefficients on the refractive indices of the surface layer ($SiO_2$) and the Si substrate and on the thickness of the surface layer. In this curve fitting procedure, optical constants in the visible range for $SiO_2$ and Si taken from literature [Jel92,Pal85] were used and the thickness of the surface layer was the variable parameter. The surface oxide thicknesses as a function of annealing temperature are shown in the inset to figure 4.1. The surface oxide thickness increases from (3.5 $\pm$ 0.2) nm for the prebonded sample and up to a value of (10.7 $\pm$ 0.2) nm for the sample annealed at 1100°C.

### 4.1.2. Evaluation of the "reststrahlen" band: Strain relaxation of the surface oxide with annealing.

The changes in the thickness and structure of the surface and interface silicon oxide layers upon annealing can be evidenced by infrared spectroscopy in the spectral range of the "reststrahlen" band of $SiO_2$ (950-1300 $cm^{-1}$). The IR transmission spectra of Si-Si wafer bonds measured with p-polarized light at oblique incidence (70°) are presented in figure 4.2. by solid lines. Due to the Berreman effect [Ber63] the experimental geometry used allows both TO and LO vibrations in $SiO_2$ to be observed. Indeed, the IR spectra shown in figure 4.2. reveal two absorption features at 1107 $cm^{-1}$ and at about 1250 $cm^{-1}$. The band at 1250 $cm^{-1}$ assigned to LO phonons undergoes changes in intensity and frequency position. The shift of LO phonons from 1247 $cm^{-1}$ for the prebonded sample to 1256.5 $cm^{-1}$ for the sample annealed at 1100°C will be discussed later. The strong feature at 1107 $cm^{-1}$, however, corresponds to absorption due to interstitial oxygen in silicon bulk and only the weak shoulder appearing at 1050 $cm^{-1}$ is due to the TO phonon line in silicon oxide. The inset to figure 4.2 shows the decrease of the absorption band at 1107 $cm^{-1}$ of about 0.5% which occurs as a result of annealing. This indicates that diffusion of interstitial oxygen from bulk silicon to the surfaces and buried interface [Ahn90] with further formation of silicon oxide takes place.

The IR transmission spectra of Si-Si bonded wafers contain information on both surface and buried interface oxides. In order to distinguish between the surface

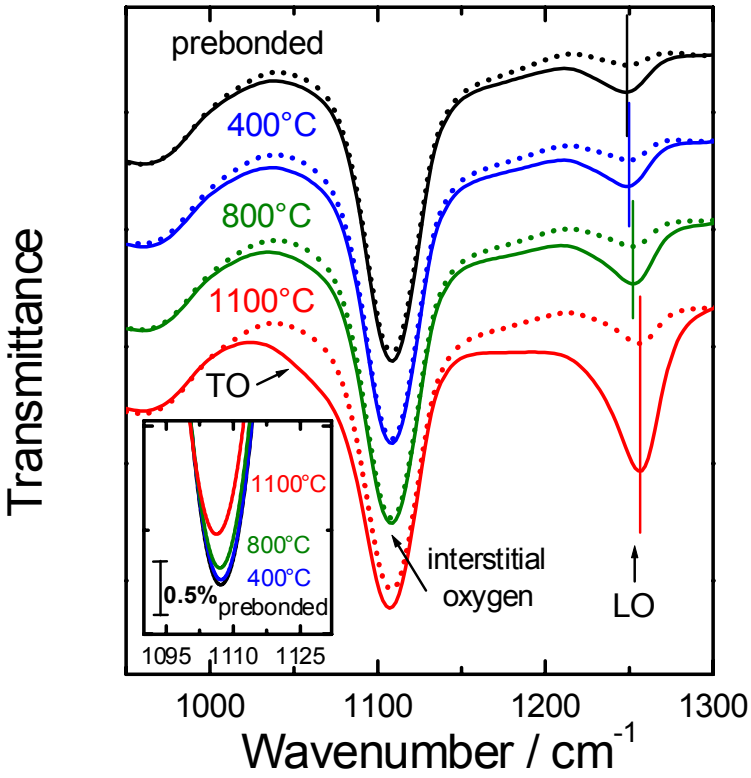


***Fig. 4.2.*** IR transmission spectra of as-prepared (solid lines) and etched Si-Si bonded wafers (dotted lines). Spectra of the samples annealed at different temperatures are equidistantly shifted.

and interface contributions in the IR spectra of the bonds, the surface oxide of Si-Si bonded wafers was removed by chemical etching in HF (40%) solution for 2-5 minutes. After etching, the samples were measured again in the same geometry. No differences in the spectra of samples etched for 2 and 5 minutes were observed. It can thus be concluded that the etching process entirely removes the surface oxide but does not affect the interface oxide. The spectra of Si-Si bonded wafers after etching are presented in figure 4.2 by dotted lines. The same shift of the LO frequency position is observed for etched and non-etched samples upon annealing. This behaviour

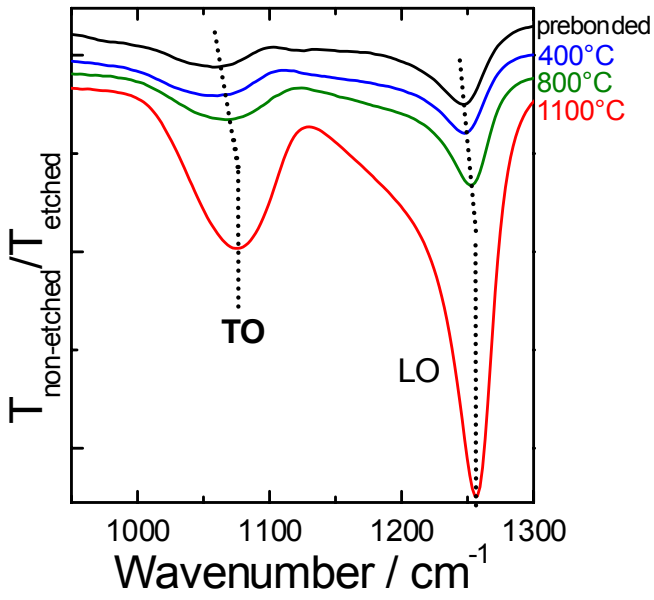


***Fig. 4.3.*** IR response of the surface silicon oxide of the Si-Si bonded wafers.

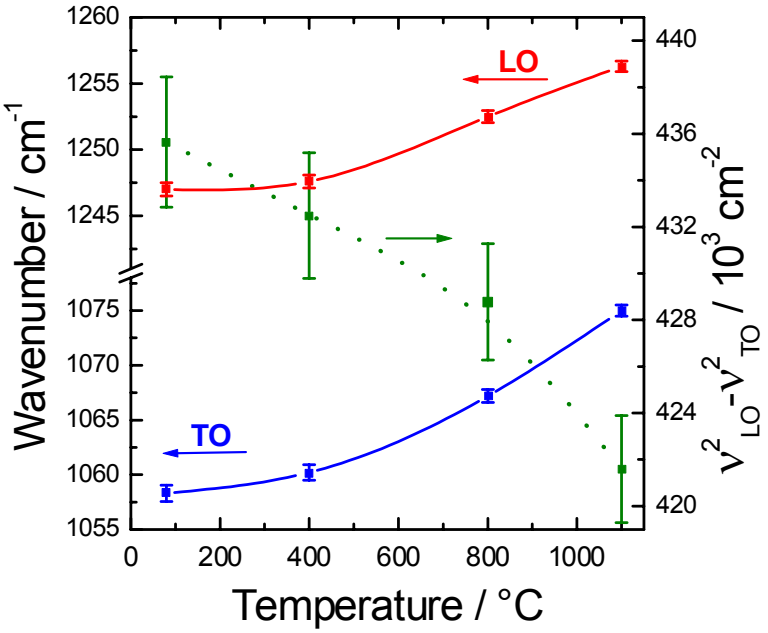


***Fig. 4.4.*** Dependence of TO and LO frequency position and $\nu_{LO}^2$-$\nu_{TO}^2$ value in the surface oxide as a function of annealing temperature. Solid and dotted lines are included as guides for the eye.

suggests that the internal structure of the oxide at the surface and the interface is very similar. While no changes are observed in the frequency position of LO modes before and after etching, the intensity of these modes and the shoulder appearing at 1050 $cm^{-1}$ decrease significantly after etching.

In order to obtain the IR response of the surface oxide, the spectra of non-etched Si-Si bonded wafers (solid lines in figure 4.2) were divided by the spectra of the samples etched in HF (dotted lines in figure 4.2). Spectra obtained as a result of this normalization procedure are shown in figure 4.3. This procedure allows the TO phonon modes of the surface oxide located at about 1050 $cm^{-1}$ to be clearly distinguished. The increasing intensity of both LO and TO modes upon annealing is explained by the increase of surface oxide thickness confirming the ellipsometric results. With increasing temperature, both vibrational modes shift towards higher frequencies but the magnitude of the shifts differs for TO and LO modes.

For a detailed analysis of the spectral changes the TO and LO frequencies and the $\nu^2_{LO}$-$\nu^2_{TO}$ value are plotted in figure 4.4 as a function of annealing temperature. The error bars of $\nu^2_{LO}$-$\nu^2_{TO}$ values are derived from the errors in the determination of LO and TO frequencies. Apparently both $\nu_{TO}$ and $\nu_{LO}$ increase with annealing temperature. The magnitude of the TO shift is larger, leading to a decrease in LO-TO splitting. There are two possible reasons for such a change occurring in the

$\nu^2_{LO}$-$\nu^2_{TO}$ value, namely strain relaxation and changes in stoichiometry. Improving stoichiometry at a silicon/silicon oxide interface with increasing oxide thickness, i.e. an increasing $SiO_2$ content in a $SiO/SiO_2$ mixture, is accompanied by an increase of LO-TO splitting [Que00]. The decrease of the $\nu^2_{LO}$-$\nu^2_{TO}$ value with annealing temperature, which was experimentally observed can consequently not be explained by improving stoichiometry. Therefore, only strain relaxation can be responsible for the behaviour of TO and LO phonons.

The central-force network model [Gal79] allows the relation between LO and TO frequency positions, $\nu^2_{LO}$-$\nu^2_{TO}$ values and strain in surface silicon oxides to be established. Using this model the frequencies of TO and LO modes of the asymmetric O stretch vibrations in $SiO_2$ depend on the Si-O-Si bridge bond angle as follows [Leh82]:

$$\nu_{TO} = \sqrt{\frac{2}{m}}\left(\alpha \sin^2\frac{\theta}{2} + \beta\cos^2\frac{\theta}{2}\right)^{1/2} \tag{4.1}$$

$$\nu_{LO} = \sqrt{\frac{2}{m}}\left(\alpha \sin^2\frac{\theta}{2} + \beta\cos^2\frac{\theta}{2} + \gamma\right)^{1/2} \tag{4.2}$$

where $\alpha$, $\beta$ are the central and non-central force constants, $\gamma \sim \rho/(2m+M)$; $m$ and $M$ are the masses of O and Si atoms, $\rho$ is the density of $SiO_2$. Taking into consideration the ratio $\beta/\alpha \approx 0.16$ [Gal79], $\beta$ can be neglected and the relations can be written as:

$$\nu_{TO} = \nu_0 \sin\frac{\theta}{2} \tag{4.3}$$

$$\nu^2_{LO} - \nu^2_{TO} \sim \rho/(2m+M) \tag{4.4}$$

were $\nu_0 = \sqrt{2\alpha/m}$ was determined to be 1134 $cm^{-1}$ assuming that a TO frequency position at 1078.5 $cm^{-1}$ corresponds to completely unstrained vitreous silica ($\theta$ = 144°) [And00]. Using the experimental values of $\nu_{TO}$, it was found that the Si-O-Si bond angle increases from 137.7° for the prebonded sample to 143° for the sample annealed at 1100°C. Increasing annealing temperature thus leads to an increase of TO frequency position that correlates with the increase of Si-O-Si bridge angle $\theta$. At the same time, one can see from equation (4.4) that the decrease of the $\nu^2_{LO}$-$\nu^2_{TO}$ value is obviously connected with a decreasing atomic density $\rho$. Consequently increasing annealing temperature also results in a reduction of strain in surface oxides, manifested by increasing $\theta$ and decreasing $\rho$. The evolution of the optical phonons with annealing observed in our IR experiments is consistent with that of

vitreous silica [Ish97] rather than wet chemical [Gur99] or thermally grown oxide [Ish97].

The frequency positions of LO phonons observed in the IR spectra of oxides are exactly the same for etched and non-etched bonds. If the LO-TO splitting is also the same it is very likely that the internal structure of surface and interface oxides is very similar.

### 4.1.3. Determination of buried interface thickness: growth of interface oxide with annealing.

While the thickness of the surface oxide can be determined precisely from ellipsometry measurements, the characterisation of the interface oxide is not possible due to a small penetration depth of the light in Si in the visible and UV spectral range. However, the buried oxide thickness can be evaluated from IR spectra of Si-Si wafer bonds.

The buried oxide thickness was determined from the best fit of the IR spectra of etched Si-Si bonded [Him01a]. In the simulation, the IR transmission spectra were calculated using the E-H matrix method applied for a multi-layer system [Azz92, Joh95]. In the calculation of IR transmission spectra of etched Si-Si bonded wafers the propagation of light through the multilayered structures is completely described by the dielectric function $\tilde{\varepsilon}$ and the thickness *d* of each layer. This model considers that propagation of light in a layer is governed by linear equations and the continuity of the tangential field across an interface between two isotropic media can be written as a 2×2 matrix [Azz92]. Following this approach the complex reflectance and transmittance coefficients $\tilde{r}$ and $\tilde{t}$ can be determined as follows:

$$\begin{pmatrix} 1 \\ \tilde{r} \end{pmatrix} = \tau \begin{pmatrix} \tilde{t} \\ 0 \end{pmatrix}, \tau = \begin{pmatrix} T_{11} & T_{12} \\ T_{21} & T_{22} \end{pmatrix};$$
$$R = \left|\tilde{r}\right|^2 = \left|\frac{T_{21}}{T_{11}}\right|^2, T = \left|\tilde{t}\right|^2 = \left|\frac{1}{T_{11}}\right|^2 \qquad (4.5)$$

In the case of *n* layers sandwiched between two semiinfinite ambient media (0), the elements of the matrix $\tau$ can be deduced from:

$$\tau = I_{01}\prod_{k=1}^{n}\left(L_k I_{k,k+1}\right)I_{n,0} \tag{4.6}$$

were $I_{k,k+1}$ are the matrices of the interface between *k* and *k+1* media, and $L_k$ is the matrix of propagation in the layer *k*. These matrices can be written as:

$$I_{k,k+1} = \begin{pmatrix} \frac{1}{t_{k,k+1}} & \frac{r_{k,k+1}}{t_{k,k+1}} \\ \frac{r_{k,k+1}}{t_{k,k+1}} & \frac{1}{t_{k,k+1}} \end{pmatrix}; L_k = \begin{pmatrix} e^{j\beta_k} & 0 \\ 0 & e^{-j\beta_k} \end{pmatrix}, \beta_k = \frac{2\pi\tilde{n}_k}{\lambda} d_k \cos\Phi_k \tag{4.7}$$

were $t_{k,k+1}$ and $r_{k,k+1}$ are Fresnel's coefficients of transmission and reflection at the *k,k+1* interface, $\tilde{n}_k$, $d_k$, $\beta_k$ are the complex indices of refraction, thickness and phase thickness of layer *k*, respectively. $\phi_k$ is the angle between the direction of light propagation in the layer *k* and the normal to sample surface. This angle can be calculated from the angle of incidence using Snell's law:

$$\tilde{n}_0 \sin\Phi_0 = \tilde{n}_1 \sin\Phi_1 = \cdots = \tilde{n}_n \sin\Phi_n \tag{4.8}$$

The extinction coefficient of Si which is very sensitive to the concentration of interstitial oxygen (band at 1107 $cm^{-1}$) atoms in bulk Si, was determined from the best fit to an IR transmission spectrum of an etched single Si wafer. Thus, the phonon absorption in Si bulk was automatically taken into account. The extinction coefficient of Si obtained and the literature data for silicon oxide [Pal85] were then used for the simulation of the IR transmission spectra of etched Si-Si bonded wafers taking the oxide thickness as a fitting parameter. The interface oxide layer was represented as a $SiO_2$ layer clad by two thin (0.7 nm) intermixed $SiO_2$/SiO layers (with

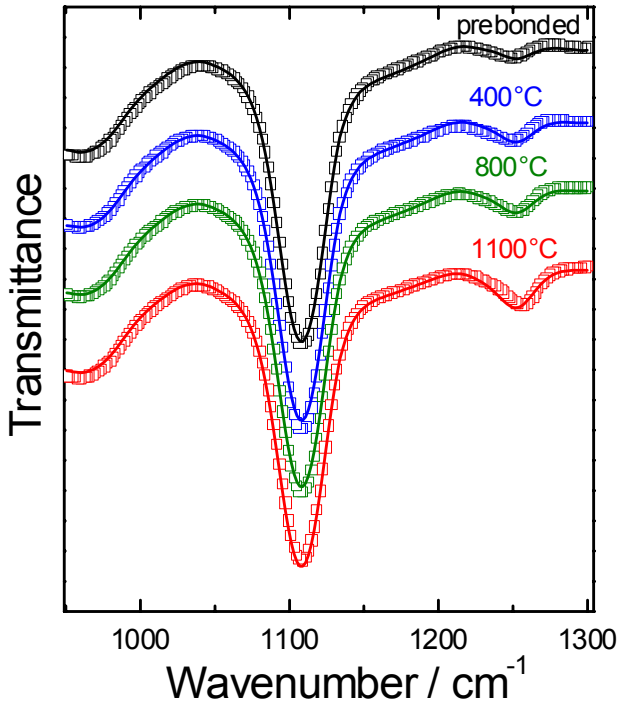


***Fig. 4.5.*** Experimental (symbols) and calculated (lines) IR transmission spectra of etched Si-Si bonded wafers.

40% of $SiO_2$) to describe the $Si/SiO_2$ interface region according to the arguments of Queeny *et al.* [Qui00]. The IR spectra calculated using this model are shown in figure 4.5 (solid lines) together with the experimental ones (symbols). One can easily see that a very good agreement between calculated and experimental spectra was obtained.

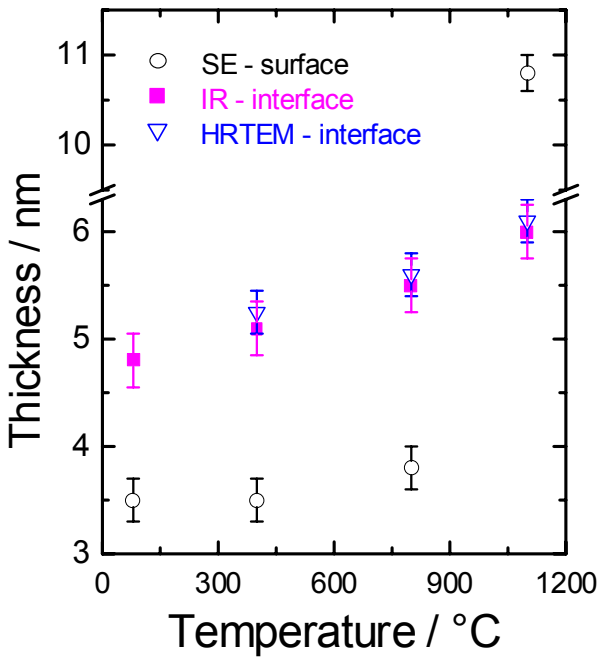


***Fig. 4.6.*** Surface (ellipsometry results are shown by circles) and interface (IR and HRTEM data are squares and triangles, respectively) oxide thicknesses as a function of annealing temperature.

The change of interface oxide thickness of Si-Si bonded wafers with annealing temperature evaluated from the calculation is shown in the figure 4.6 by filled squares together with the values of surface thickness determine from ellipsometry (open circles). The buried oxide layer thickness increases continuously from (4.8 ± 0.25) nm for the prebonded sample, i.e. room temperature bonded without any further annealing step, up to (6.0 ± 0.25) nm for the sample annealed at 1100°C. However, in a previous study [Wel96b] a saturation of the oxide thickness with annealing above 800°C was found from analysis of MIT absorption by LO phonons in the buried oxide.

In order to verify the buried oxide thicknesses determined using IR spectroscopy, HRTEM measurements were additionally performed [Him01b]. The cross sectional HRTEM images of the bonded wafers are shown in figure 4.7. The values of interface oxide layer thickness obtained from HRTEM images are also shown in figure 4.6 by triangles. Obviously, the results deduced from infrared spectroscopy correspond very well with those of HRTEM measurements. The HRTEM characterization of the prebonded sample is not available because a low bond energy leads to wafer debonding during HRTEM sample preparation. Thus, up to now the IR spectroscopy is the only non-destructive method which allows the buried interface oxide thickness even for the prebonded sample to be evaluated.

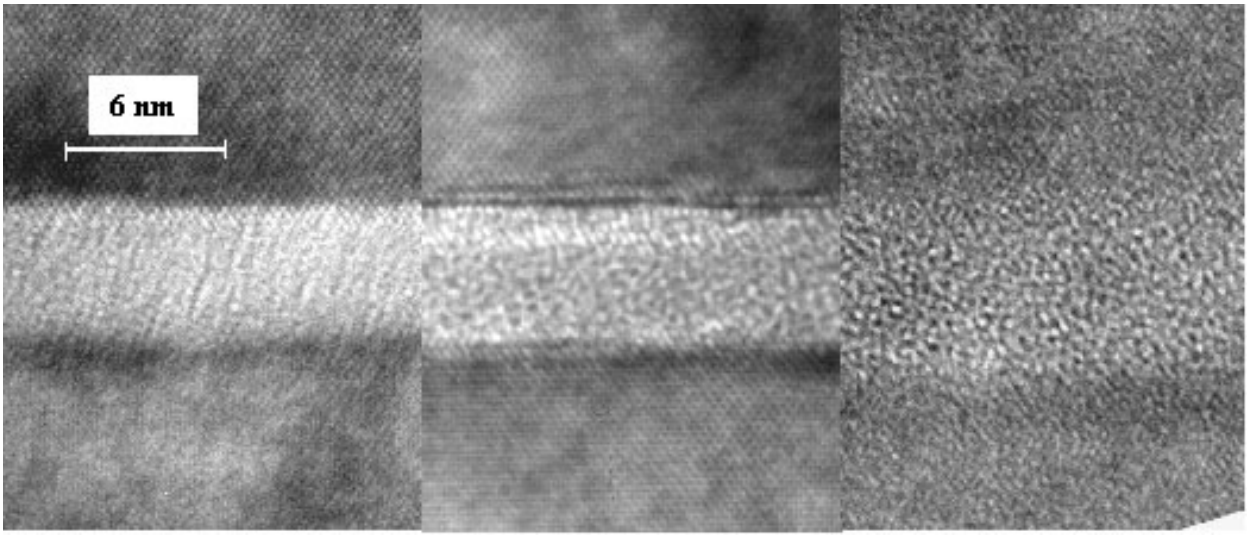


***Fig. 4.7.*** Cross sectional HRTEM images of the interface regions of the bonds annealed at 400°C (a), 800°C (b) and 1100°C (c).

Understanding of interface oxide formation requires not only the thickness and internal structure but also the chemical species to be determined. Figure 4.8 shows MIT spectra of Si-Si bonded wafers annealed at different temperatures in the spectral range of OH and SiH bands. Due to strongly enhanced absorption at the interface [Wel96b], only the chemical species absorbed at buried interface can be observed. It is clearly observable that the spectrum of the prebonded sample is dominated by the

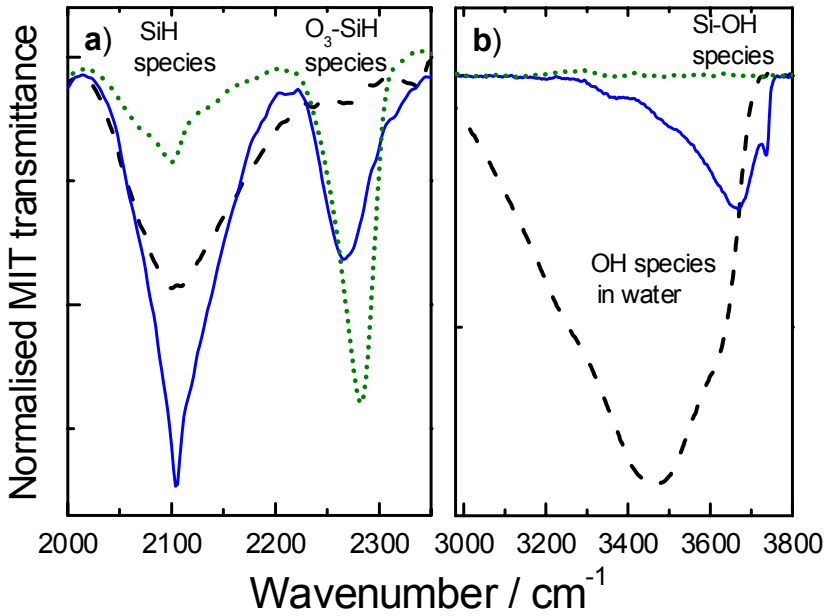


***Fig.4.8.*** p- polarized IR MIT spectra of the prebonded (dashed lines) and annealed at 400°C (solid lines) and 800°C (dotted lines) Si-Si wafer bonds measured in the spectral regions of SiH and $O_3$–SiH species (a) and OH and Si–OH species (b). The spectra were normalised with respect to spectrum of the sample annealed at 1100°C.

absorption at 2105 $cm^{-1}$ assigned to Si-H stretch modes in dihydride species at the (100) silicon surface [Cha86] (figure 4.8.a) and by the broad absorption band centered at 3460 $cm^{-1}$ attributed to O-H stretch vibrations of water molecules adsorbed at the interface of prebonded wafers (figure 4.8.b). Annealing of Si-Si bonded wafers at 400°C causes a strong decrease of the absorption band centered at 3460 $cm^{-1}$ due to loss of the water at the interface. In addition, new features appear at 3680 $cm^{-1}$ and 3737 $cm^{-1}$ attributed to O-H stretch vibrations in H bonded silanol (Si-OH) groups and to isolated (not H bonded) silanol groups at the buried interface, respectively [Fei94]. The decomposition of water causes an increased absorption by Si-H stretch vibrations at 2105 $cm^{-1}$. At the same time a new band at 2270 $cm^{-1}$, which corresponds to the Si-H vibrations in $O_3$-Si-H species appears. Further annealing of samples at 800°C leads to a disappearance of silanol species. This fact is accompanied by the decrease of intensity of the SiH band at 2105 $cm^{-1}$ and the increasing absorption by $O_3$-Si-H species at 2270 $cm^{-1}$. The frequency position of $O_3$-Si-H band is shifted towards higher frequencies with annealing from 400°C to 800°C. This relates to diffusion of hydrogen atoms located near the buried interface into the oxide layer [Mil99].

The MIT measurements performed on Si-Si bonded wafers show the role of the chemical species in the growth of buried oxide with annealing. In the temperature range below 400°C, decomposition of water determines the increase of buried interface thickness by oxidizing the crystalline Si. Further annealing induces the condensation and formation of silanol species which again leads to an increase of interface oxide thickness. This is consistent with the model of wafer bonding [Wel96a]. The growth of oxide during this last step of annealing (800°-1100°C) is determined by the diffusion of oxygen from silicon bulk in silicon oxide layers. This mechanism is suggested by the attenuation of interstitial oxygen band (at 1107 $cm^{-1}$) in the IR transmission spectra upon annealing as can be seen from the inset of figure 4.2.

# 4.2. Low temperature wafer bonding

Significant progress has been achieved in understanding and optimizing Si-Si wafer bonding processes, especially at high temperature [Ton99]. However, microelectronic applications require bonding processes at low temperatures (below 400°C). In this subchapter a comparative analysis of IR response of low temperature Si-Si bonded wafers prepared using different surface activation treatments is presented and mechanisms for low temperature bonding are proposed.

## 4.2.1. Monitoring of chemical species at buried interfaces during annealing of RCA, $O_2$-plasma and RIE Si—Si bonded wafers.

In order to achieve hydrophilic Si surfaces different wet chemical treatments and surface plasma activation were used as presented in Table 4.1. For each process (RCA, $O_2$ plasma and RIE) three sets of RT samples were produced. One set of samples was annealed in $N_2$ for 6h at 200°C and another set was annealed in the same condition at 400°C. The RT bonded samples were further annealed in a small low-vacuum annealing chamber placed in the air-purge box of the spectrometer. The spectra were recorded at different temperatures in the range 30°-225°C. With increasing annealing temperature the absorption of IR light by free carrier increases. The spectra measured during annealing are corrected for the carrier absorption by multiplying each spectrum to get the same transmittance level as for the samples at RT.

| Sample (native oxide) | Pre- treatment |
|---|---|
| RCA | RCA |
| $O_2$ plasma | $O_2$ plasma (barrel reactor) + DI water rinsing |
| RIE | Reactive Ion Etching (RIE) – $O_2$ plasma + DI water rinsing |

***Table 4.1.*** Description of the pre-treatments of the Si wafers before room temperature bonding.

At room temperature bonding of two hydrophilic wafers is realised by the hydrogen bonding between the water molecules adsorbed on the two surfaces [Ton99]. The MIT IR spectra for all RT bonded samples (RCA,$O_2$ plasma, RIE) in figure 4.9 are dominated by a broad absorption band between 3000-3800 $cm^{-1}$

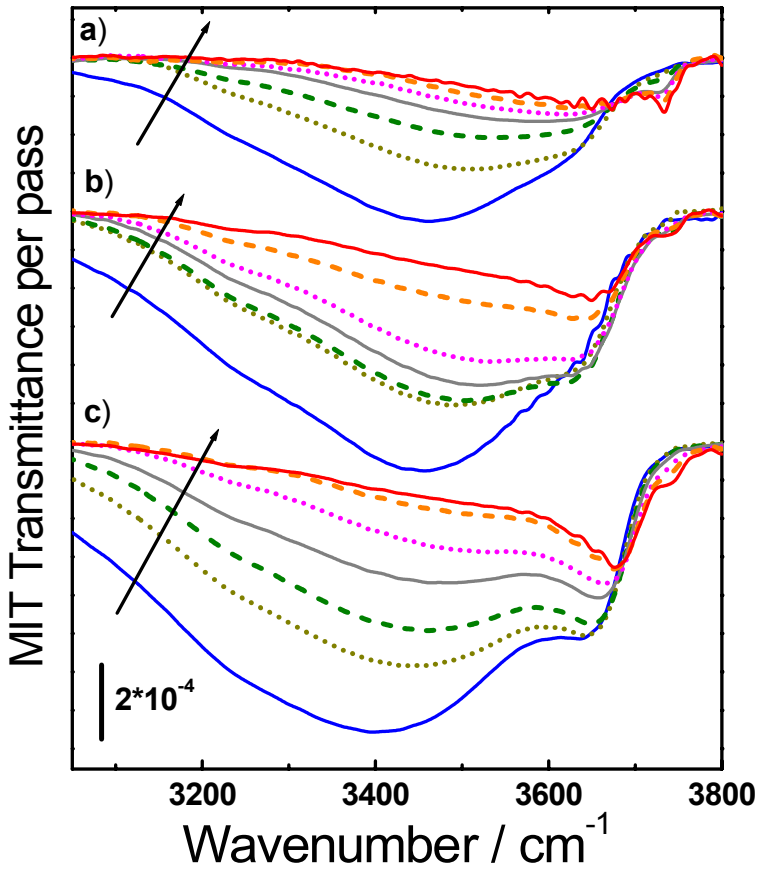


***Fig. 4.9.*** *In situ* MIT IR spectra recorded during annealing in the region of water and SiO-H absorption for a) RCA b) $O_2$ plasma and c) RIE samples. The temperature increases in the direction of the arrows in the order: 30°, 100°, 125°, 150°, 175°, 200° and 225°C.

corresponding to the stretching vibrations of different hydroxyl groups [Him02b]. The RIE and $O_2$ plasma samples contain more molecular water (bands centred at ~ 3400-3450 $cm^{-1}$) at the interface compared to the RCA sample, because the plasma activation produces a more reactive surface able to adsorb more water. During annealing most of the molecular water diffuses away from the bonded interface or into the oxide layer reaching the Si crystal and oxidising it.

With increasing annealing temperature different rearrangements of the water and hydroxyl species take place. For all samples heating induces a reduction in the intensity of the band at 3400 $cm^{-1}$ indicating the loss of water at the interface. Part of the water molecules attack the most strained Si-O-Si bonds leading to an increasing number of OH groups (slow fracture effect [Mic84]):

$$H_2O + \equiv Si–O–Si\equiv \Rightarrow \equiv Si–OH + HO–Si\equiv \qquad (4.9)$$

At 150°C a band centred at 3500-3550 $cm^{-1}$ corresponding to H stretching vibration of the surface SiOH species which is hydrogen bonded to molecular water [Bri90] can be distinguished. At the same time a band at 3737 $cm^{-1}$ develops as observed for the RCA sample while in the other two samples a band at 3650 $cm^{-1}$ (in RIE sample) and a shoulder at the same frequency (in $O_2$ plasma sample) appear. This means that in the RCA sample isolated (no H bonded) SiOH species are formed while for the other samples the SiOH species are mutually H-bonded [Bri90]. In the case of the RCA sample the isolated SiOH groups do not contribute to the bonding mechanism. For $O_2$ plasma and RIE treated samples the SiOH groups are H bonded to either vicinal SiOH from the same surface or to SiOH from the opposite surface and are therefore involved in the bonding mechanism of the two silicon wafers. Further increasing of the annealing temperature determine the polymerisation of the SiOH species with formation of siloxane [Gös99]:

$$\equiv Si–OH + HO–Si\equiv \Rightarrow \equiv Si–O–Si\equiv + H_2O \qquad (4.10)$$

reflected by the decrease of intensity at 3650 $cm^{-1}$ especially in the spectra for $O_2$ and RIE samples. When this polymerisation appears between species at opposite surfaces Si-O-Si bridges are formed at the interface contributing to the increasing bonding energy.

Formation of Si-O-Si bridges is limited by the contact area of the two surfaces and by the number of Si-OH groups at the two Si surfaces. It is expected that the plasma activation processes will increase the surface density of Si-OH groups [Sun02b], increasing concomitantly the probability of strong Si-O-Si formation. In very good agreement with this statement are the values that are obtained for bonding energies (see figure 4.10.) using the blade test method. The measured surface

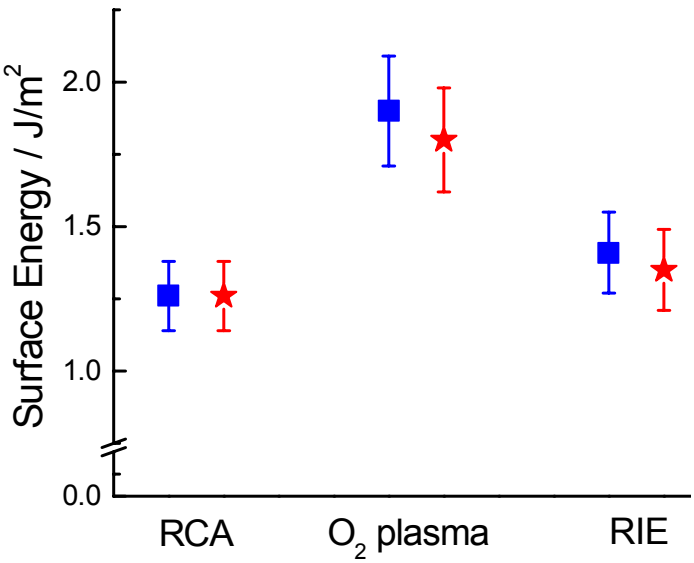


***Fig 4.10.*** Surface energies determined by the blade method for RCA, O2 plasma and RIE; 200°C (squares) and 400°C (stars) annealed samples

energies for the samples annealed at 200°C are 1.25 J/m$^2$, 1.4 J/m$^2$, and 1.9 J/m$^2$ for RCA, RIE and $O_2$ plasma, respectively. The bonding energy of the RT samples are below 200 mJ/m$^2$ and for this reason they cannot be accurately measured using the blade test method.

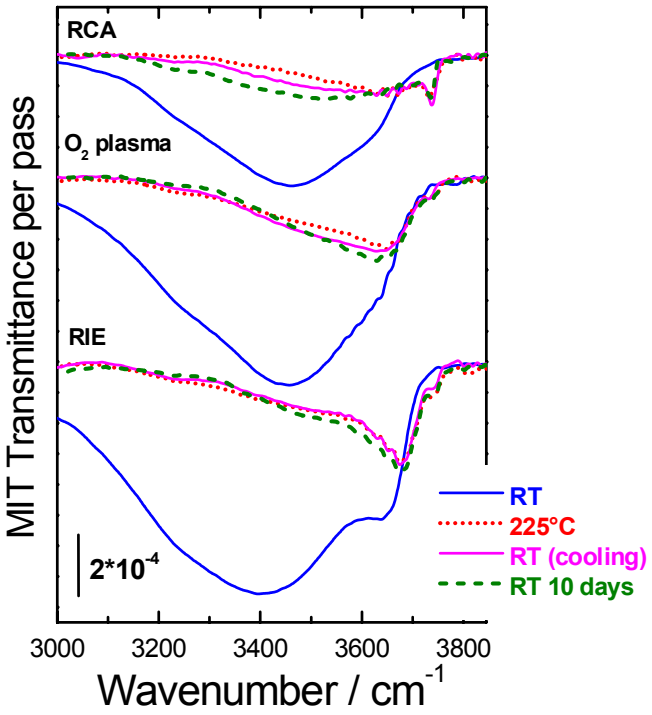


***Fig. 4.11.*** MIT IR spectra of Si-Si bonded sample at RT, 225°C and after cooling and storage in air for 10 days

In figure 4.11 the MIT IR spectra of the RT samples measured at room temperature, at 225°C and after cooling and storage in air are shown. It can be observed that even after 10 days of storage in air very little water is reabsorbed at the interface. This means that the rearrangement of the molecules at the interface which is caused by annealing at 225°C is stable in time after cooling at RT and storage in air.

The water molecules formed by condensation (Eq. 4.9) can diffuse into the thin oxide layer reaching the $Si/SiO_2$ interface. Here, water dissociates oxidising the surrounding crystalline Si and producing Si-H species [Wel96a, Wel96b] or $H_2$ [Gös99]:

$$H_2O \rightarrow Si/SiO_2 \Rightarrow SiO_2 + 2\,(O_x)SiH \qquad (4.11)$$

$$Si + 2\,H_2O \Rightarrow SiO_2 + 2H_2 \qquad (4.12)$$

where $(O_x)SiH$ denotes hydrogen bound to a Si atom which is bound to x oxygen atoms (x=0 when H is bonded to crystalline Si and x=3 when H is bonded to a Si atom in the oxide layer).

Experimental evidence was found for both reactions in the temperature range of 200°-400°C. On one hand, it can be observed in figure 4.12 that for the $O_2$ and RIE treated samples the band corresponding to the stretching vibration of H at the $Si/SiO_2$ interface at 2105 cm$^{-1}$ [Oga92] is increasing in intensity. On the other hand, it

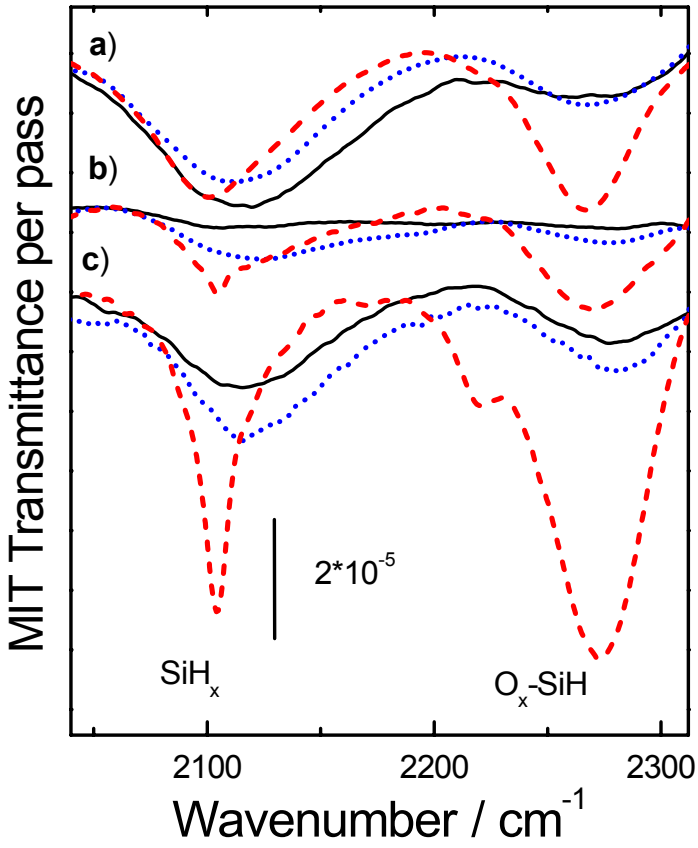


***Fig. 4.12.*** *Ex situ* MIT IR spectra in the region of $O_y$-Si-$H_x$ vibrations measured at room temperature for a) RCA b) $O_2$ plasma and c) RIE samples. The spectra correspond to RT prebonded samples (——); 200°C annealed sample (·····); and 400°C annealed samples (- - - - ).

is observable for all samples that with increasing bonding temperature the band at 2270 $cm^{-1}$ increases in intensity. This band was attributed to H stretching inside $SiO_2$ (as $O_3SiH$ groups) [Oga92].

The $H_2$ molecules produced by the decomposition of water can diffuse into the silicon oxide interfacial layer producing $O_3SiH$ species. Moreover, it is observed that in the RIE sample with more molecular water at the interface at RT the band at 2270 $cm^{-1}$ at 400°C is stronger compared to the other two samples. For RIE and RCA treated samples having a larger absorption by $O_y$-Si-$H_x$ species at 400°C IR transmission images reveal that small bubbles are formed at the interface. In figure 4.13 the IR transmission images for RIE sample before and after annealing at 400°C are shown.

In the RCA and RIE samples, where generation of bubbles at 400°C was observed, we found that the increasing of surface and interface oxide thickness with annealing is faster compared to that of the $O_2$ plasma sample. In figure 4.14 the

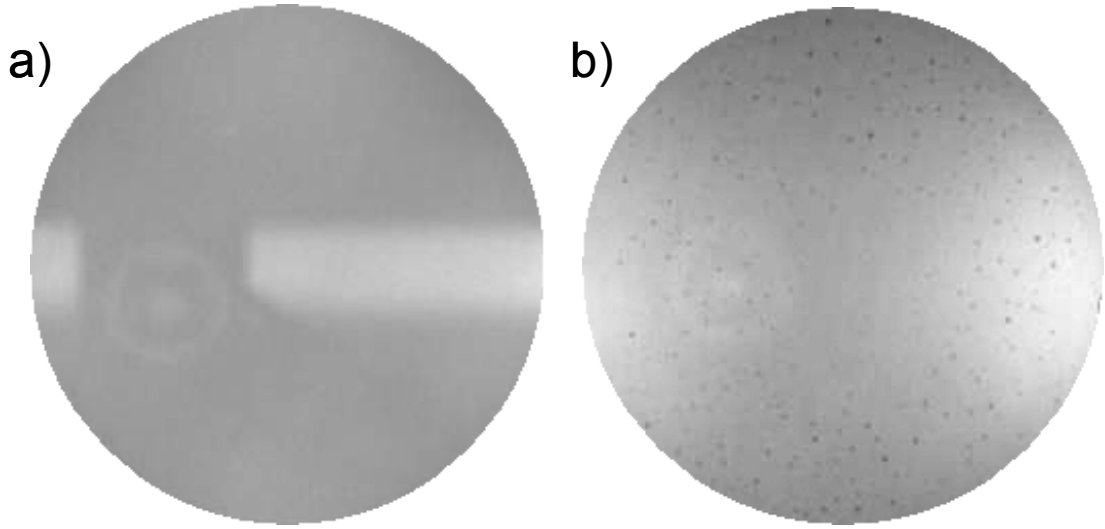


***Fig. 4.13.*** IR transmission image of prebonded (a) and annealed at 400°C (b) RIE sample.

transmission spectra of Si-Si bonded wafers in the region of LO stretching in silicon oxide are presented. As we have shown in section 4.1.3 of this work, the intensity of LO absorption correlates with the oxide thickness. We can see from figure 4.14 that when the temperature changes from RT up to 400°, the intensity of LO mode it is stronger increased for RCA and RIE samples compared with the $O_2$ plasma sample suggesting an accelerated oxidation process.

This fact correlates very well with the appearance of bubbles in RCA and RIE samples generated by the $H_2$ molecules due to oxidation of crystalline Si by water according to equation (4.12). A second argument for the statement above is that the intensity of the band at ~ 2270 $cm^{-1}$ in figure 4.12. for RCA and RIE samples is higher increased than for $O_2$ plasma sample when the annealing temperature rises from RT up to 400°C. This indicates that in RCA and RIE samples the molecular

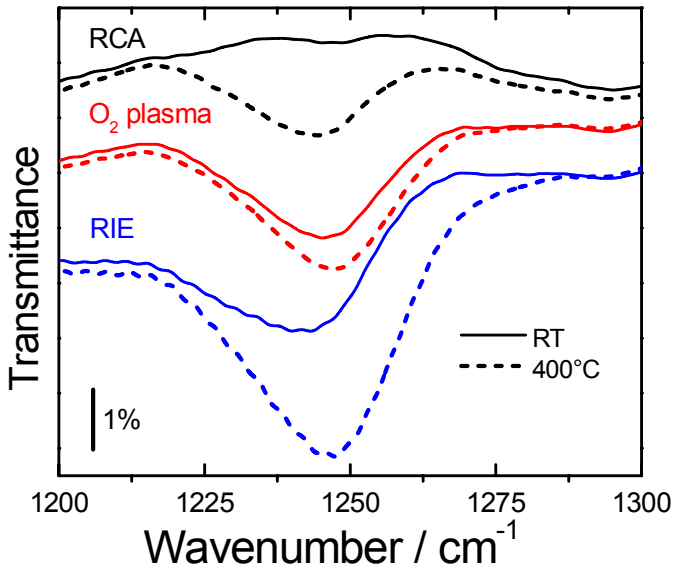


***Fig. 4.14.*** Transmission spectra (70°, p-polarisation) of RT and 400°C Si-Si bonded wafers, in the region of LO mode in silicon oxide.

$H_2$ formed during oxidation will be partially dissolved in the thin oxide (band at 2270 $cm^{-1}$) and the rest will form bubbles at the interface [Gös99].

The bubble generation will decrease the bonding energy because it destructs the intimate contact of the two Si surfaces and the formation of strong Si-O-Si bridges. In the $O_2$ plasma sample we have seen that the oxidation process is not so pronounced, and in this case the few $H_2$ molecules produced will be dissolved in the oxide and no bubbles are formed. Consequently the bonding strength for $O_2$ plasma sample is larger compared to those of RCA and RIE samples as can be observed from figure 4.10.

### 4.2.2. MIT investigation of Si-$SiO_2$ / Si bonded wafers

In the previous section it was shown that the exposure to oxygen plasma is more effective in the formation of strong Si-Si bonded wafers than the wet chemical (RCA) surface activation at low temperatures. However, the bonding energy is limited by bubble formation at the bonded interface. In the case of wafers covered with thin native oxide, the $H_2$ produced according to equation (4.12) cannot be dissolved in the thin oxide layer and will accumulate in the bubbles. The solution to avoid this problem is to use Si wafers covered by thick (1µm) thermal oxide. The $H_2O$ molecules present at the interface cannot penetrate the thick silicon oxide layer and reach the Si/ $SiO_2$ interface (to oxidise Si according to equation (4.12)). The water will be trapped at the interface, obstructing the formation of Si-O-Si bridges. The combination of thin oxide (favouring the consumption of water) and thick oxide (which will dissolve $H_2$ molecules) has thus been identified to be the most favourable for the formation of strong wafer bonding [Krä98].

In this section we present a study of Si-$SiO_2$ / Si bonded wafers with different pre-treatments for Si wafers:

- wet chemical activation: RCA or K1 (solution of $NH_3OH$: $H_2O$: $H_2O_2$ );
- RIE oxygen plasma treatment followed by deionised water rinsing.

The samples were bonded in air at RT and annealed at 200°C in $N_2$ atmosphere for 8h. A RCA sample was bonded in low vacuum (1 mbar) and annealed by the same procedure.

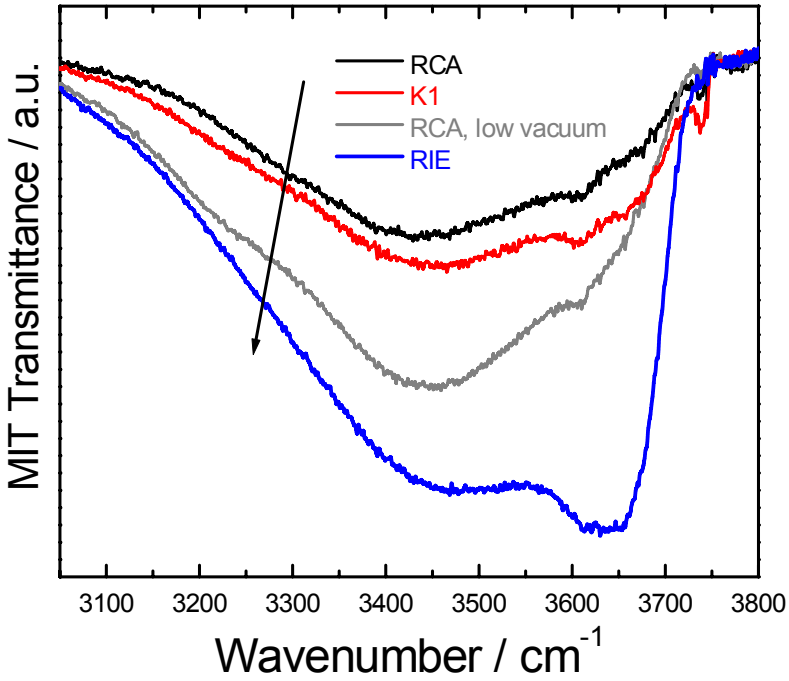


***Fig. 4.15.*** MIT IR spectra in the region of water and SiO-H stretching vibrations for 200°C Si-$SiO_2$ / Si bonded wafers with RCA, K1 and RIE pre-treatments.

Figure 4.15 shows the MIT IR spectra of the Si-$SiO_2$ / Si bonded wafers annealed at 200°C in the region of water and SiO-H absorption. It can be clearly seen that the spectra of RIE sample is dominated by a strong absorption band at 3650 $cm^{-1}$. This band correspond to coupled Si-OH groups which will polymerize favoring formation of Si-O-Si bridges (Eq. 4.10). For this sample we expect a much larger bonding energy than for the other three samples.

In good agreement the blade test method performed to determine the strength of the bonds showed that the value for the surface energy for RIE sample is more than double than that for the other samples (see figure 4.16). It

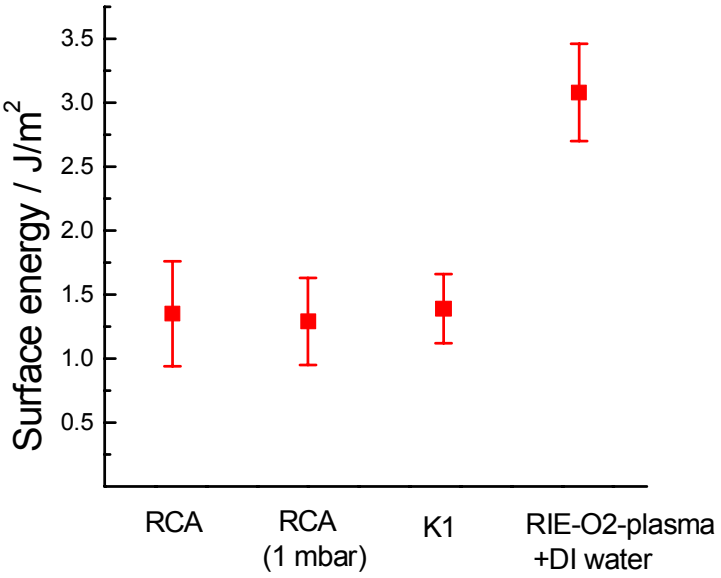


***Fig. 4.16.*** Surface energies determined by blade method for 200°C annealed Si-$SiO_2$ / Si bonded wafers with RCA, K1 and RIE pre-treatments.

should be pointed out that IR images show bubble free interfaces for all the samples confirming that the thick oxide layer dissolved most of $H_2$ formed by silicon oxidation. Unlike to [Ton98] an improvement of surface energy for the RCA sample by bonding in vacuum (1mbar) could not be observed.

Thus surface energy for the RIE sample is much higher than in the case of the plasma treated sample with thin interfacial oxide (see previous section). This fact reveals the benefit of using thick interfacial oxides. The value of more than 3000 mJ/m$^2$ for the RIE sample is surprisingly high, because in this temperature range a saturation of ~ 1660 mJ/m$^2$ is expected [Ton99, Han00]. This saturation value corresponds to a density of 4.6 / nm$^2$ OH groups for the hydrated silica surface, supposing that the Si-OH groups are able to be converted entirely into Si-O-Si.

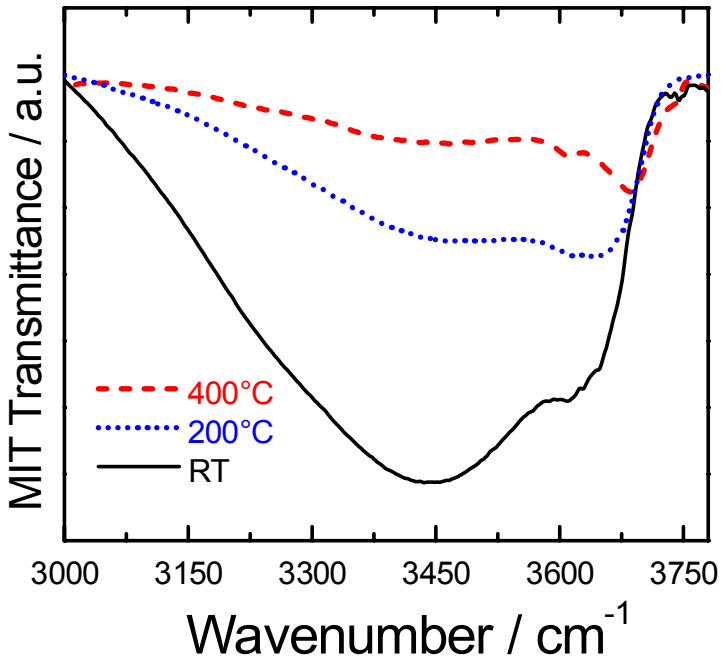


***Fig. 4.17.*** Evolution with annealing of the MIT IR spectra for RIE Si-$SiO_2$ / Si bonded wafers.

In figure 4.17 the evolution of MIT IR spectra of RIE sample with annealing up to 400°C is presented. As can bee seen a strong shoulder at 3650 cm$^{-1}$ exists even for the RT bonded sample. This means that the RIE process will provide a surface coverage by OH groups higher than 4.6 / nm$^2$. It was found that damages of the surface layer by the oxygen plasma can presumably accommodate a high concentration of OH groups [Sun02b]. A second effect of the plasma exposure is the formation of a disordered surface structure which will increase the water removal from the bonded interface allowing the formation of covalent bonds [Ami00]. Both

these effects of RIE oxygen plasma treatment can explain the value of 3000 mJ/m$^2$ for the surface energy of the RIE sample annealed at 200°C.

Such a high bonding energy for the RIE sample is very well suited for technical applications. Low temperature silicon wafer bonding technology based on the RIE oxygen plasma treatment was successfully used for the fabrication of Microscanner arrays in the Center of Microtechnologie Chemnitz [Ges00]. Debonding experiments in most of the cases lead to a fracture in the silicon rather than in a separation at the bonded interface [Ges00]. This can be explained by the fact that the energy of Si-O bonds (4.5 eV) is larger than the energy of Si-Si bonds (1.9 eV) [Ton 99].

# 4.3. Mechanisms for low temperature silicon wafer bonding.

In the previous section it was shown that the highest bonding energy was obtained for Si-$SiO_2$ / Si bonded wafers activated by RIE oxygen plasma. Figure 3.18. shows schematically the low temperature bonding mechanism for the Si-$SiO_2$ / Si system. The buried interface consist of a thin and a thick oxide layer, and the bonded interface (region where the two silica surfaces come into contact). The diagram presents the chemical reactions and atomic rearrangements which take

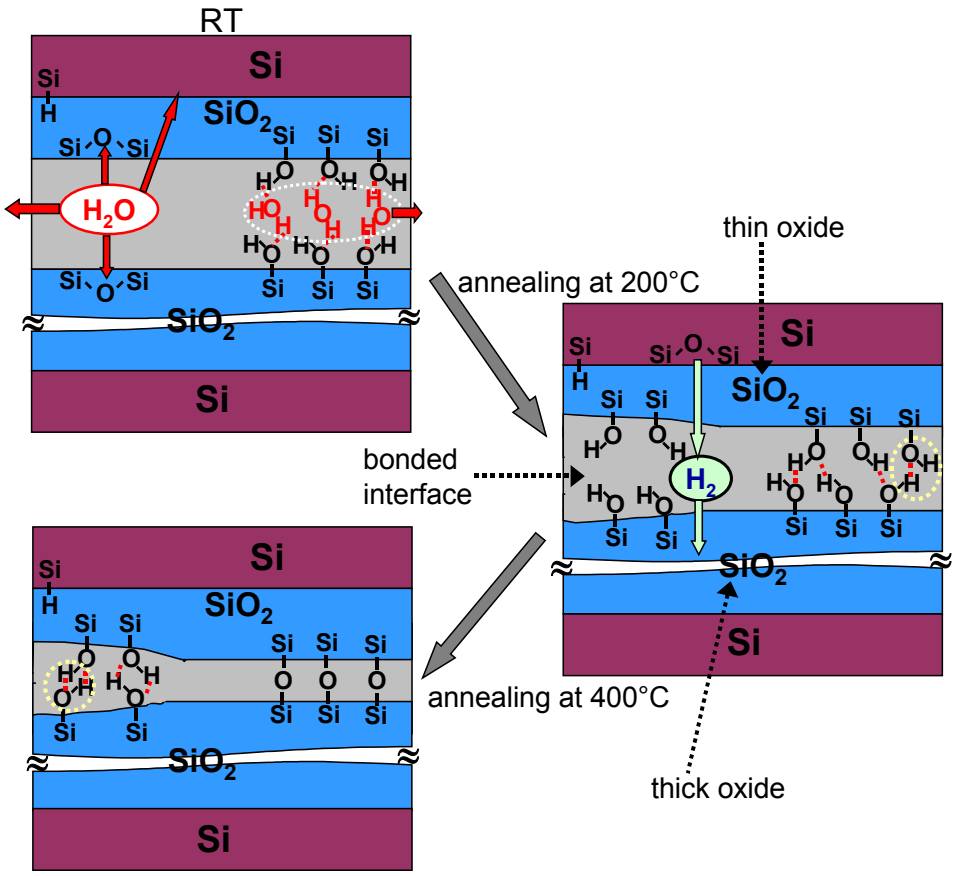


***Fig. 4.18.*** Schematic diagram of low temperature wafer bonding mechanism for Si-$SiO_2$ / Si bonded wafers

place at the buried interface as indicated by IR spectra and IR transmission images of the investigated bonded wafers.

At RT the bonding is realized via hydrogen bridges formed between adsorbed water molecules and terminal Si-OH groups from silica surfaces. With annealing

water molecules trapped at the interface can diffuse away or through the thin oxide and react at the $Si/SiO_2$ interface forming additional oxide. During this oxidation process molecular hydrogen is formed. Since the thick thermal oxide has an open structure the hydrogen molecules can be dissolved in the oxide reducing the bubble formation and the gas pressure at the bonded interface [Ton99].

On the other hand, molecular water will react with the strained Si-O-Si groups at the silica surface forming Si-OH species. RIE plasma activation process will produce a very reactive surface so that the density of Si-OH groups which cover the silica surface will be very high. This fact is very important for the bonding process because when two Si-OH groups from the opposite surfaces come into contact, strong covalent Si-O-Si bridges are formed by a condensation reaction. The thin oxide will favor the consumption of the resulting water (which cannot diffuse trough the thick layer), while the thick oxide will dissolve the hydrogen molecules formed (which cannot be dissolved within the thin oxide layer).

# Chapter 5

# Properties of porous low-k xerogel films.

## 5.1. Determination of thickness, porosity and optical constants of xerogel films.

In order to extract the information contained in the ellipsometric spectra a model describing the structure of the sample and its optical response is usually applied. In figure 5.1.a. typical Ψ ellipsometric spectra of a xerogel sample are plotted by symbols. The spectra are measured at angles of incidence $\varphi_0$ near the Brewster angle of Si, namely 69°, 71°, 73°, 75° and 77. Since the xerogel films are formed from a porous $SiO_2$ structure, they can be considered transparent in the visible region

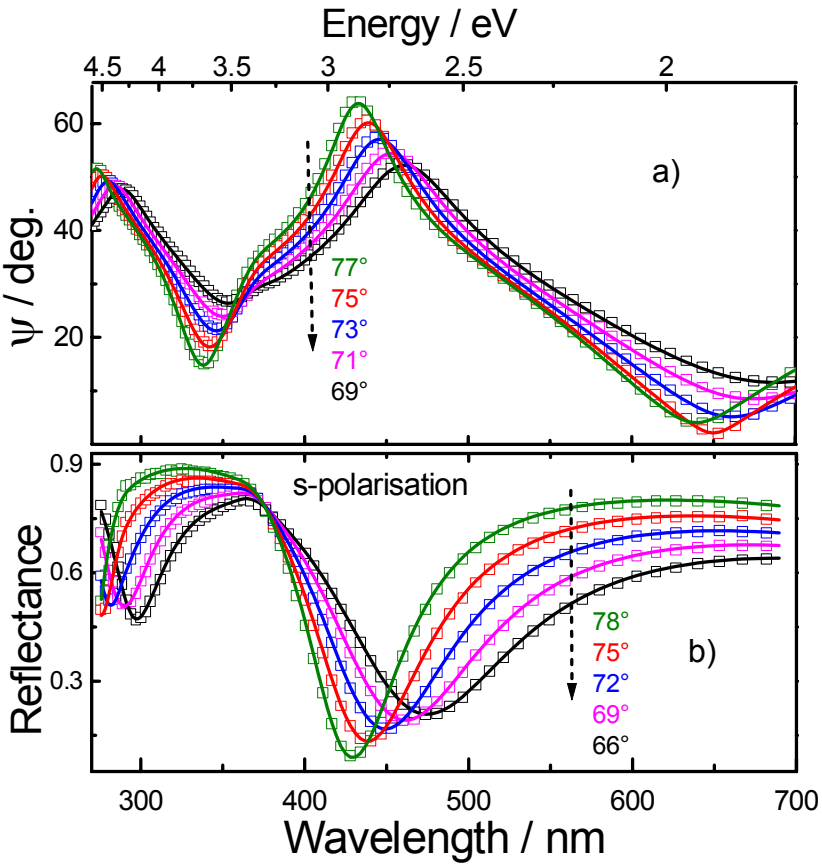


***Fig. 5.1.*** Ψ ellipsometric (a) and reflectance (b) spectra of a xerogel films on a Si substrate. The symbols are experimental data and solid lines are the fits obtained using a Cauchy model.

due to the absence of absorption features in $SiO_2$ below 5 eV. In order to analyse the ellipsometric data a model consisting of a film having a Cauchy dispersion relation and a Si substrate was employed. The Cauchy dispersion relation: $n(\lambda) = a_n + b_n / \lambda^2$ describes very well the refractive index of transparent materials. The parameters $a_n$ and $b_n$ and the thickness $d$ of the film were considered as fitting parameters in the calculation of $\Psi$ and $\Delta$ values. The fits obtained are plotted by solid lines in figure 5.1.a. This procedure allows both thickness and refractive index to be determined simultaneously.

Additionally, reflectance measurements on the same sample were performed for s-polarised light and angles of incidence near the Brewster angle. The reflectance spectra are shown in figure 5.1.b. by symbols. To analyse the reflectance data the same optical model as for ellipsometric data was applied. The values obtained for thickness and optical constants by analysing $\Psi$ and $\Delta$ ellipsometric data and reflectance spectra are in very good agreement. The values of refractive indices obtained are plotted in figure 5.2. while a difference smaller than 1 nm for the thickness value was obtained from these two different measurements.

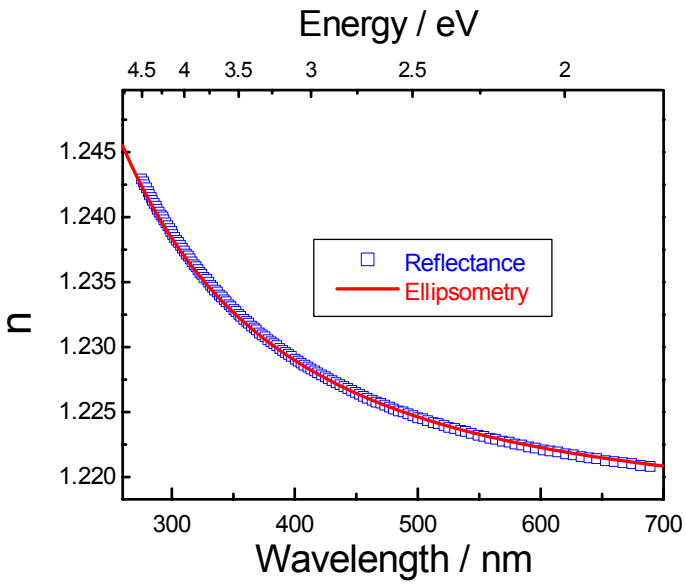


***Fig. 5.2.*** Optical constants of a silica xerogel film obtained from reflectance (squares) and ellipsometric (line) measurements.

Different silica xerogel films were prepared using an acid catalysed sol-gel method as described in section 2.2. The films were spun on 6 inch Si (100) substrate from a TEOS solution and gelated in a solvent atmosphere before being dried. The variation of process parameters allowed the porosity and dielectric constant to be varied. The processes used and labelled A to E are described by the parameters as given in table 5.1.

| Process | Mixing time (min.) | Aging time (min.) | Spin speed (rot/min). |
|---|---|---|---|
| A | 100 | - | 1000 |
| B | 120 | - | 1150 |
| C | 124 | 201 | 1150 |
| D | 126 | 205 | 1150 |
| E | 135 | 207 | 1400 |

***Table 5.1.*** Variation of the parameter of the sol-gel spin coating process: mixing time, aging time and spin speed.

The values and the errors in the determination of the parameters $a_n$, $b_n$ and thickness $d$, obtained by applying the procedure described above are given in the table 5.2. The errors are calculated as a summation of the errors provided by the fitting procedure and of the statistical errors given by performing measurements in several points (typically 4 for each sample).

| Process | Cauchy | | | EMA |
|---|---|---|---|---|
| | $a_n$ | $b_n \cdot 10^3$ | d / nm | $f$ / % |
| A | $1.257 \pm 8 \cdot 10^{-3}$ | $2.24 \pm 0.07$ | $430.8 \pm 7.5$ | $40.4 \pm 3.3$ |
| B | $1.252 \pm 3.5 \cdot 10^{-3}$ | $2.14 \pm 0.05$ | $449.2 \pm 6.7$ | $43.4 \pm 2.6$ |
| C | $1.198 \pm 3.5 \cdot 10^{-3}$ | $1.83 \pm 0.02$ | $574.5 \pm 5.1$ | $55.3 \pm 1.5$ |
| D | $1.191 \pm 1.8 \cdot 10^{-3}$ | $1.78 \pm 0.05$ | $624.2 \pm 6.5$ | $56.7 \pm 1.7$ |
| E | $1.184 \pm 3 \cdot 10^{-3}$ | $1.64 \pm 0.06$ | $557.5 \pm 8.7$ | $58.6 \pm 2.1$ |

***Table 5.2.*** The values and the errors of the optical parameters, thickness and porosity determined by fitting of the ellipsometric data using Cauchy and EMA models.

Typical fits obtained by means of this model are plotted in figure 5.3 by solid lines. They agree very well with the experimental data for samples C, D, and E over the whole spectral range. For samples A and B, however, the fits and the experimental data diverge above 4 eV which means that these samples become absorbent in this region. Therefore, for these two samples, an Urbach absorption was considered in addition to the Cauchy dispersion. The refractive indices of xerogel films obtained using this model [Him01c] are plotted in figure 5.4. by continuous lines together with the literature data for the refractive index of $SiO_2$ [Pal85]. The refractive indices of xerogel films are clearly lower compared to those of $SiO_2$ due to the porous structure of the xerogels. As can be seen the refractive index decreases from sample A to sample E. The reason of this change in the refractive index will be discussed later. The n values obtained are indeed suitable for electronic applications.

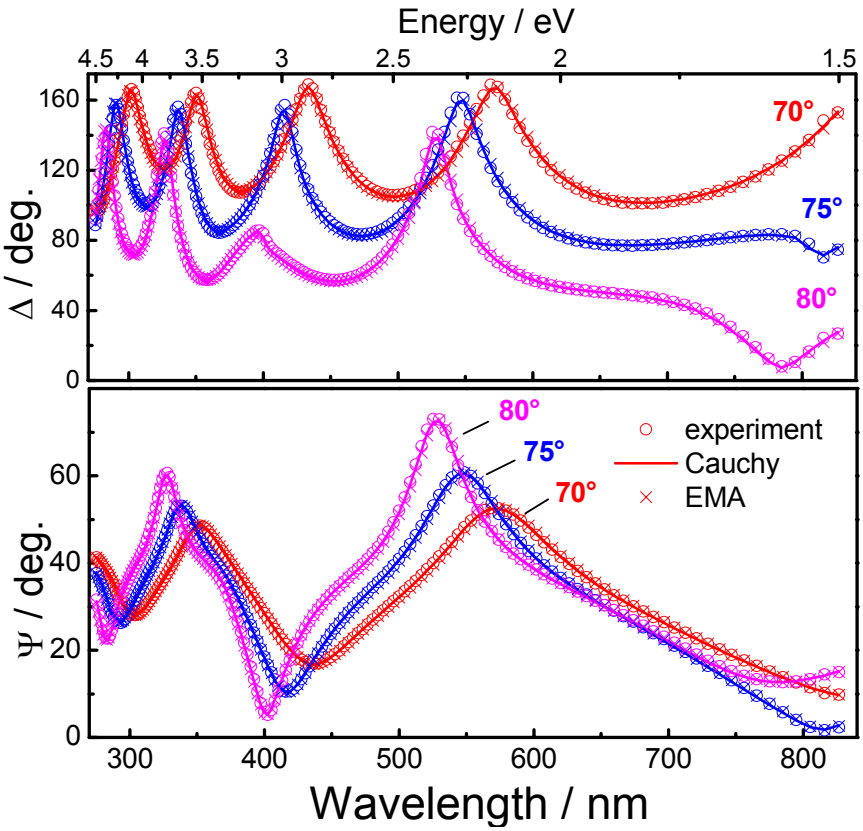


***Fig. 5.3.*** Ψ and Δ ellipsometric spectra of a silica xerogel film on a Si substrate. Symbols are the experimental points, continuous lines are the fits obtained using a Cauchy model and crosses lines are the fits obtained using EMA model. The spectra refer to sample C.

The extinction coefficients are plotted in the inset of figure 5.4. Consideration of Urbach absorption in the case of samples C, D and E results in k=0 which supports that these samples are indeed completely transparent. The absorption in the ultraviolet (UV) region of the spectra in the case of samples A and B is due to the fact that these samples were produced without aging. This clearly influences the polymerisation of Si-O-Si networks, leading to a less porous structure with some Si-Si bonds, which can explain the absorption in the short wavelength region of the spectra [Sas95].

Having the thicknesses of the films determined using the Cauchy model, an Effective Medium Approximation (EMA) was applied in order to determine the values of the film porosity. Maxwell-Garnet EMA was used because this approximation assumes spherical inclusions of one medium (voids) embedded in the host material ($SiO_2$). In this way the xerogel material is seen as a mixture $SiO_2$/voids. Considering that the inclusions of voids which have the dielectric constant of air (=1) are embedded in a $SiO_2$ matrix, the dielectric constant of the mixture $SiO_2$/voids ($\varepsilon$) is given by:

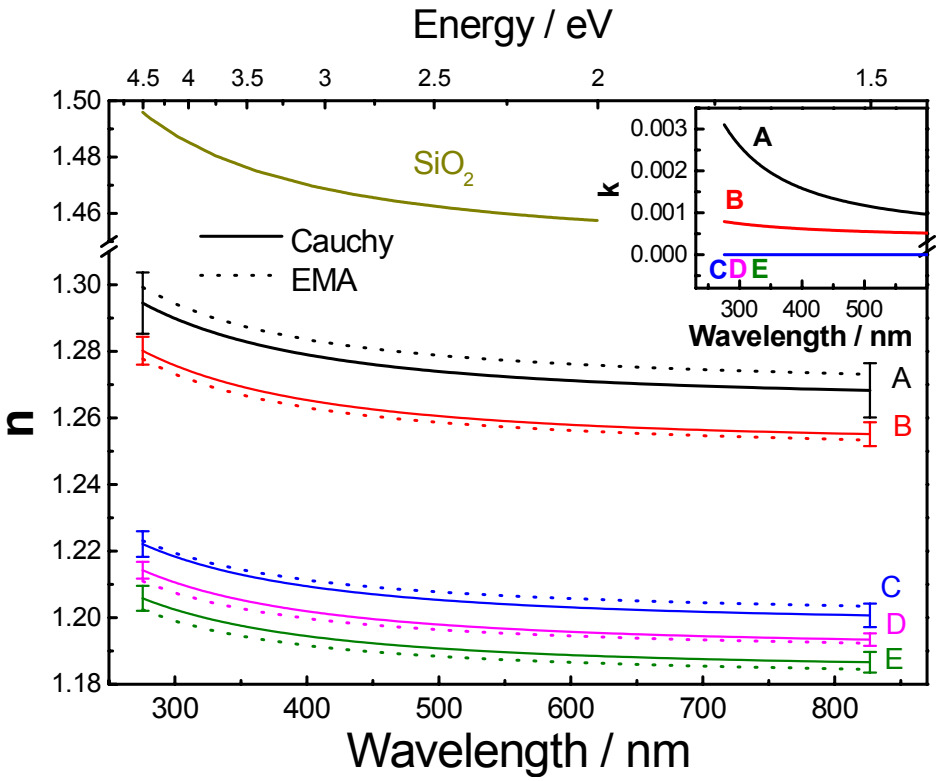


***Fig. 5.4.*** The refractive index of the xerogel films: solid lines are the calculated using Cauchy model and dotted lines are calculated using EMA model. The inset shows the extinction coefficient obtained considering Urbach absorbance.

$$\frac{\varepsilon-\varepsilon_{SiO_2}}{\varepsilon+2\varepsilon_{SiO_2}} = f\frac{1-\varepsilon_{SiO_2}}{1+2\varepsilon_{SiO_2}} \tag{5.1}$$

where $f = Volume_{voids}/Volume_{film}$ defines the porosity of the film, and $\varepsilon_{SiO2}$ the dielectric constant of $SiO_2$. In this model the thickness was fixed and the experimental spectra are fitted in order to determine the porosity *f* of the films. Typical fitting results obtained in this way are plotted in figure 5.3 as indicated by crosses. The results are also summarised in table 5.2. Taking into account the relation $\varepsilon=n^2$, the n values obtained are plotted by dotted lines in figure 5.4. A comparison with the n values obtained using the Cauchy model reveals fairly good agreement between the refractive indices calculated using Cauchy and EMA models within error bars of Cauchy values.

Figure 5.5 shows the refractive index at 632.8 nm and porosity values for the different processes A to E. As can be seen the decrease of the refractive index from 1.271 to 1.188 is accompanied by an increase of the porosity of the films from 40.4% to 58.6% when going from process A to process E. The increase of the porosity is obviously related to the increase of the mixing time. With increasing mixing time, more hydrolysis and condensation reactions can take place and this determines the

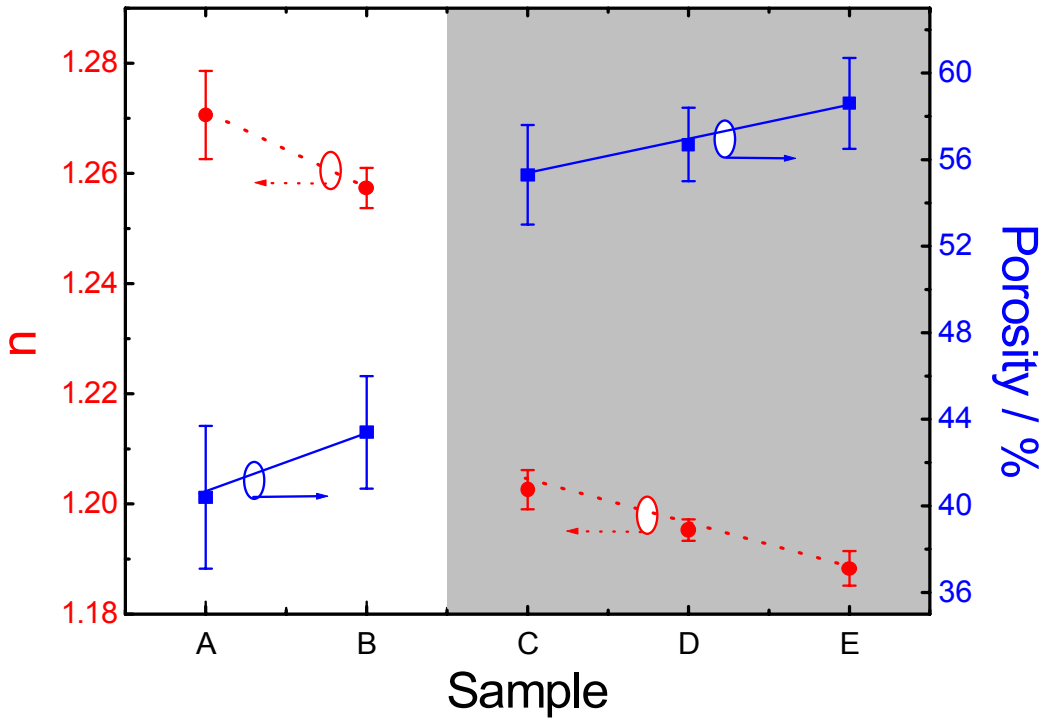


***Fig. 5.5.*** Porosity (squares) and refractive index (circles) at 632.8 nm for samples A to E obtained by variation of the process parameters as presented in Table 5.1.

formation of longer ≡Si-O-Si≡ chains and consequently a more porous ≡Si-O-Si≡ network. The samples can be grouped in A and B, on one hand, and C,D, and E, on the other hand (plotted in the figure 5.5 as non-shaded and shaded regions, respectively). This grouping is also due to differences in the preparation conditions.

### 5.1.1. Reliability of thickness determined using Cauchy model.

Very close thickness values were obtained by applying the Cauchy model to evaluate ellipsometric and reflectance data. The thickness obtained from Cauchy model was further used by EMA models in order to determine the porosity of the films. The algorithm for calculation of thickness and porosity is based on the minimisation of MSE value (Eq. 3.10.) as described in section 3.2.1. The thickness (for Cauchy model) or porosity (for EMA model) are the ones at which the lowest MSE values are obtained.

The fitting procedure performed using the EMA model using the Cauchy thickness and other thicknesses revealed that the thickness determined with the Cauchy model is reliable. In figure 5.6 the minima of MSE values for the EMA

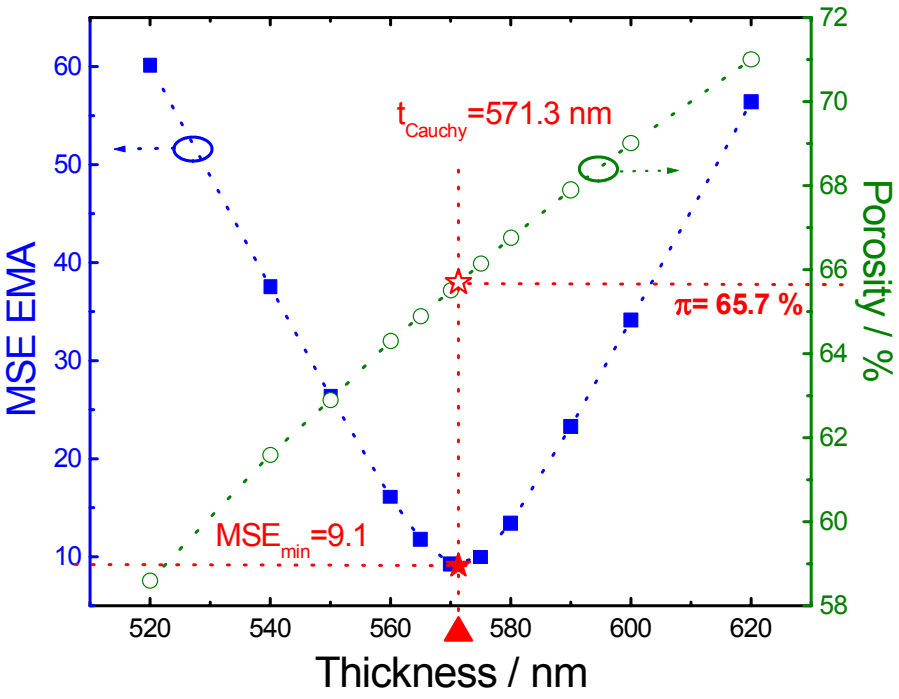


***Fig. 5.6.*** Plot of **MSE** values (filled squares) of EMA model as function of thickness.

calculations obtained by performing fits for different fixed thicknesses are plotted. It can be clearly seen that the minimum of MSE values for the EMA model is obtained for the thickness determined by the Cauchy model. The porosity values obtained at each fixed thickness are plotted in figure 5.6. by open circles. The porosity of the film will correspond to the minimum of MSE. For the example presented in figure 5.6 the film has a thickness of 571.3 nm and a porosity of 65.7%.

# 5.2. Hydrophobisation processes for porous low-k silica xerogel films.

## 5.2.1. FTIR investigation of the hydrophobisation mechanism.

Despite of excellent electrical properties porous silica xerogels films suffer in the as-deposited state from water adsorption caused by surface silanol groups. To overcome this problem and to get a sufficient reliability for further integration steps the films have to be made hydrophobic. Hydrophobisation is achieved by silylation, that means surface silanol groups are reacted to yield trimethylsilyl (TMS) Si-$(CH_3)_3$ surface groups as shown in figure 5.7. This treatment removes H atoms from the hydrophilic surface Si-OH groups and replaces them with TMS groups which are less polar and hydrophobic [Jin97]. In this section an FTIR investigation of silylation of xerogel films using hexamethyldisilazane (HMDS), trimethylsilyldiethylamine (TMSDEA) and trimethylsilylacetate (OTMSA) is presented. The schemes of the balance reactions for the chemicals above were shown in figure 2.5 in section 2.2.

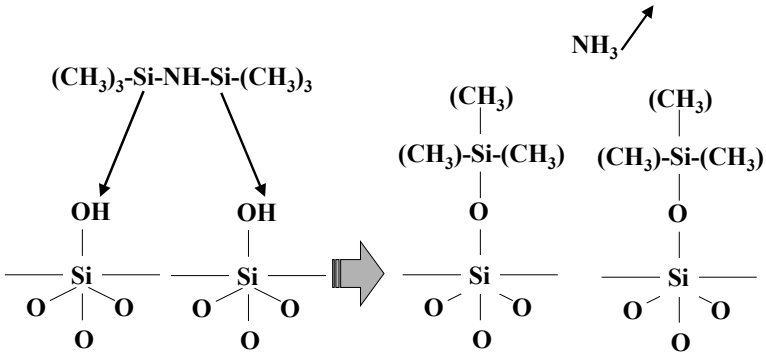


***Fig. 5.7.*** Scheme of the hydrophobisation reaction of silica with HMDS.

The HMDS attack leads to the obvious destruction of surface silanols as can be observed in the FTIR spectra of figure 5.8. The spectra were recorded in oblique incidence (70°) for p-polarised light and were normalized with respect to the spectrum of the Si substrate. The sharp absorption band at about 3737 $cm^{-1}$ is related to the O-H-stretching vibration of free or single (non-hydrogen-bonded) silanol groups. They are clearly visible in the spectra of the untreated sample. While the absorption at 3700 $cm^{-1}$ is due to O-H-stretching of bonded silanols, the broad absorption band centered at 3500 $cm^{-1}$ is caused by O-H vibrations of adsorbed molecular water. Si-O stretching and bending vibrations of Si-O-Si units are related to absorption bands at 1000-1300 $cm^{-1}$ and 800 $cm^{-1}$. The features at 935 $cm^{-1}$ and 985

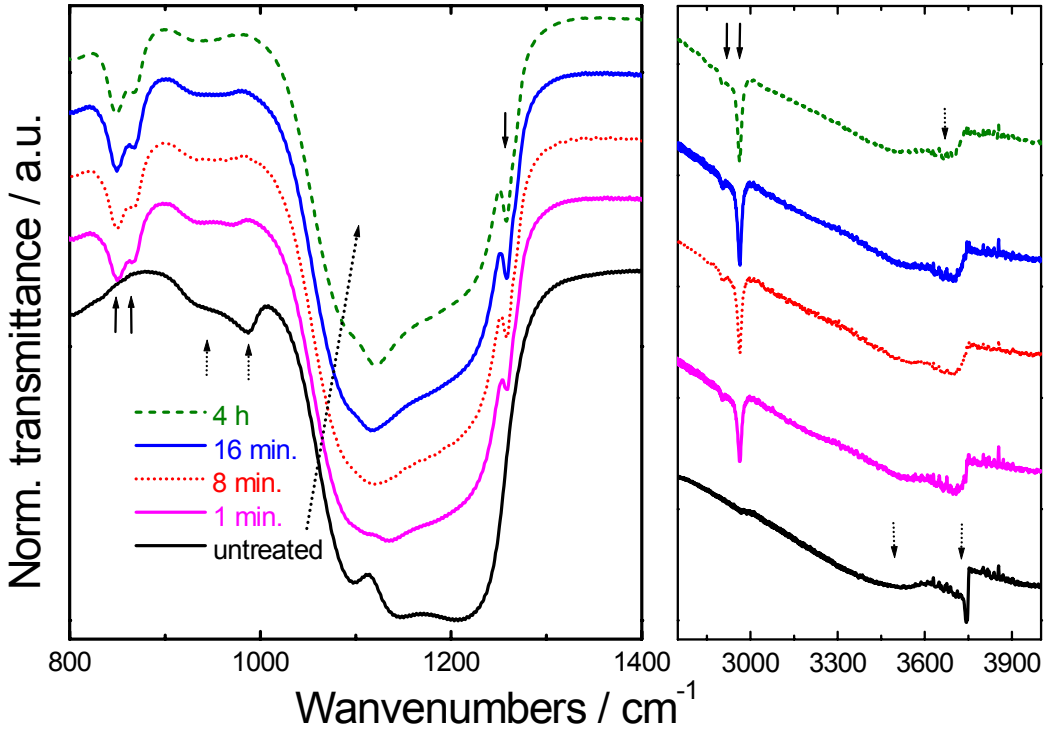


***Fig. 5.8.*** FTIR-spectra of untreated and HMDS treated samples. The treatment time increases from 1 minute up to 4 h and the order of the corresponding spectra is indicated by the arrow.

$cm^{-1}$ are related to oxygen stretching in non-bridged Si-O units (in isolated and hydrogen-bonded Si-OH groups respectively) [Par93, Kyt97]. The absorption bands at 2962 $cm^{-1}$ and 2904 $cm^{-1}$ can be related to asymmetric and symmetric C-H stretching modes in TMS groups, the band at 1257 $cm^{-1}$ is due to their bending, and the bands at 848 $cm^{-1}$ and 866 $cm^{-1}$ due to their rocking vibrational modes [Ben00]. The bands related with the absorption by CH and OH species are indicated in the figure by solid and dotted arrows respectively.

The spectrum of the 1 minute treated sample in figure 5.8 illustrates the rapid initial reaction of HMDS with isolated silanols. This reaction is indicated by rapid increasing of CH related bands together with the decrease of the bands due to isolated silanol groups. That means there should be a rapid but not full coverage of the surface by TMS-groups in a short time (<1min). The surface load by TMS-groups increases then continuously but more slowly until about 4h exposure time. The retarded reaction after the rapid initial step was explained by the reaction of HMDS with non-hydrogen-bonded silanols [Gun00] and is indicated by the slow decrease of the absorption bands at 935 $cm^{-1}$ and 3700 $cm^{-1}$ .

Further modification of the spectra are observable in the region of absorption bands caused by Si-O vibrations. The shape of the broad absorption band at 1000-1300 $cm^{-1}$ is changed continuously with increasing exposure time. The changes of the Si-O-Si network vibrations will be analysed in detail in the next section.

A remark is necessary regarding the decrease of the band corresponding to isolated surface silanols in FTIR spectra after a 1 minute treatment. Haukka *et al.* [Hau94] have shown that single OH groups can also form hydrogen bonds to neighboring methyl of TMS-groups, so that a part of the free silanols become H-bonded silanols. That makes the definition of a reaction rate based on the intensity of absorption bands related to single OH-groups uncertain. But looking at the changes described above in the FTIR-spectra related to C-H-vibrations and Si-O-vibrations, however, an estimation of the reaction rate based on comparison seems to be possible.

The most important difference between the selected silylating agents is expected to be in their reactivity. Figure 5.9 contains FTIR spectra comparing HMDS, TMSDEA and OTMSA treated samples. Single surface silanols are visible only in spectra of the OTMSA treated sample (1min) indicating a slower hydrophobisation

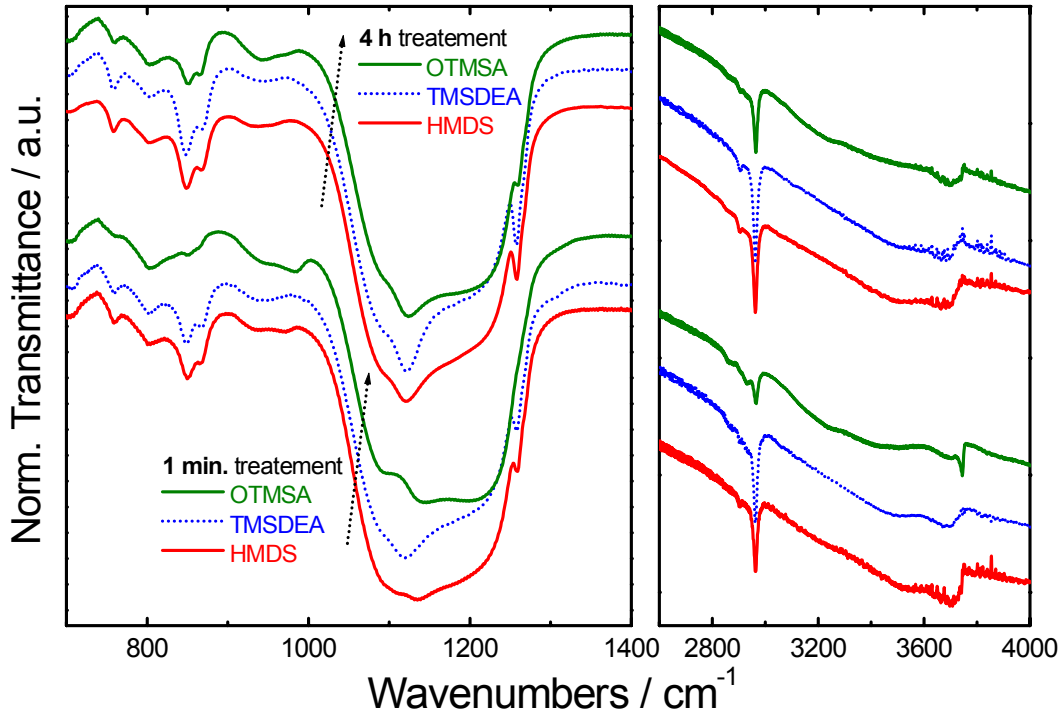


***Fig. 5.9.*** Comparison of FTIR spectra of samples silylated by HMDS, TMSDEA or OTMSA (the spectra are in the order indicated by the arrows) for 1min (bottom) and for 4 hours exposure time (top).

reaction. From the spectra in figure 5.9 it is obvious, that the reaction rate for TMSDEA should be higher than for HMDS and OTMSA. This was also confirmed by $^{29}$Si-NMR studies for TMSDEA treated sample [Frue02]. The sudden change related with structural changes between untreated samples and short time treated samples is generally bigger than that observed between short time treated samples and long time treated samples. Besides the reaction rate, the efficiency of a hydrophobisation agent is connected also to the porosity changes that the treatment will induce in the sample (which affect directly the static dielectric constant) as will be shown in the next section.

Long term stability studies for HMDS treated xerogel films regarding effects of water adsorption were also performed. The adsorption of water is visible as increasing absorption band intensity in FTIR spectra with storage time. The longer the treatment was performed the weaker was the water absorption and the deterioration of the electrical film properties. Samples treated more than 4 hours did not show any degradation of electrical behaviour due to water absorption. This was also proved for storage times exceeding 6 months [Frue02].

Interesting insight is provided by the comparison of FTIR results with those from ellipsometry. Figure 5.10 presents the absorbance spectra of samples A to E (see Table 5.1) in the region of CH vibrational modes after HMDS treatment, normalised with respect to the thickness and the porosity value of the films. Assuming that the TMS groups have the same distribution on the inner surface of the pores, the integrated intensity of the spectra in figure 5.11 is a measure of the pore surface area per pore volume unit. This integrated intensity in the region 2850-3000 cm$^{-1}$ is plotted in figure 5.11 together

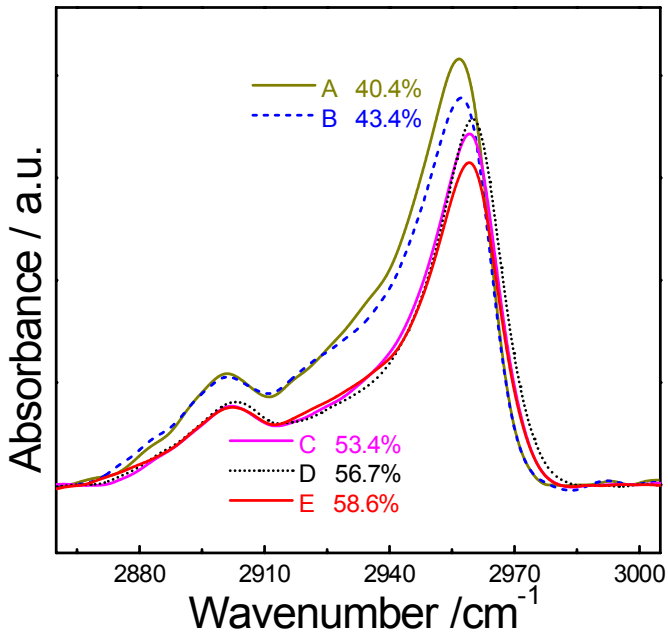


***Fig. 5.10.*** The normalised absorbance spectra of the xerogel films in the region of CH stretching vibrations.

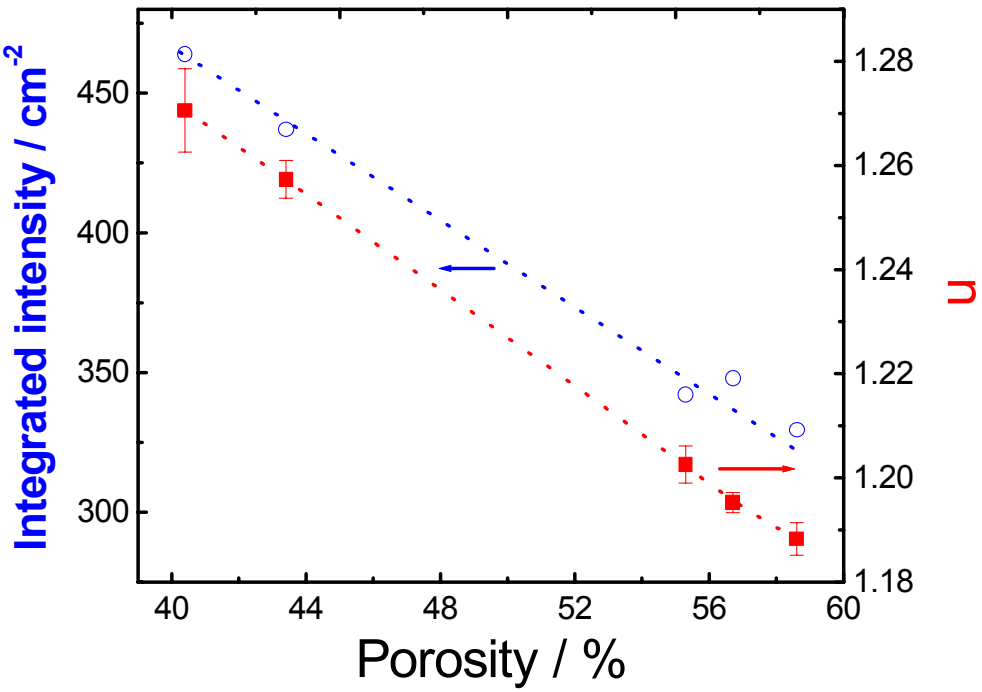


***Fig. 5.11.*** CH integrated intensity and refractive index (at 632.8 nm) as function of the porosity. (Dotted lines are guides to the eye.)

with the n values as a function of film porosity. As can be seen the less porous films have a larger integrated intensity. This means that the films with lower porosity have a larger pore surface area per pore volume unit. At a first view this behaviour is surprising, but it can be explained by the fact that in the films with a lower porosity the pores are smaller but their number is larger compared with the pores in the films with higher porosity.

This result obtained from IR spectroscopy is in very good agreement with ellipsometric porosity (EP) studies which show that the mean pore radii are smaller and the pore surface area per pore volume unit is larger in the case of lower porosities [Mur02]. Considering figure 5.10 again it can also be observed that the peak frequency of the CH bands for samples A and B is shifted to lower wavenumbers by ~ 3.5 $cm^{-1}$ compared to that of samples C,D, and E. We suppose that this shift is due to the formation of H bridges in the small pores (samples A and B) which can slightly decrease the strength of CH bonds. This behaviour seems to be similar to that of Si-OH species: when the OH· · ·O distance decreases the H bonding strength increases and the bond strength of O-H stretching decreases resulting in a similar downshift of the respective absorption feature [The90].

### 5.2.2. Influence of the hydrophobisation process on the porosity of silica xerogel films.

In this section the effect of the HMDS treatment on the porosity of xerogels films will be investigated. The porosity was calculated from ellipsometry data by means of the method described in section 5.1 FTIR was used to correlate the changes in porosity with the structural changes in Si-O-Si network.

The spectra simulated using the Cauchy model are depicted in figure 5.12 as dots, together with the experimental data (open triangles and circles) for an as-prepared and HMDS-treated xerogel film. As is readily apparent, there is a very good match between experimental and calculated spectra, indicating the reliability of the optical constants and thickness obtained in this way. The values of $a_n$ and $b_n$ and the errors in their determination are given in table 5.3. The errors are calculated as a summation of the errors arising from the fitting procedure and of the statistical errors of measurements performed at three different points on the samples.

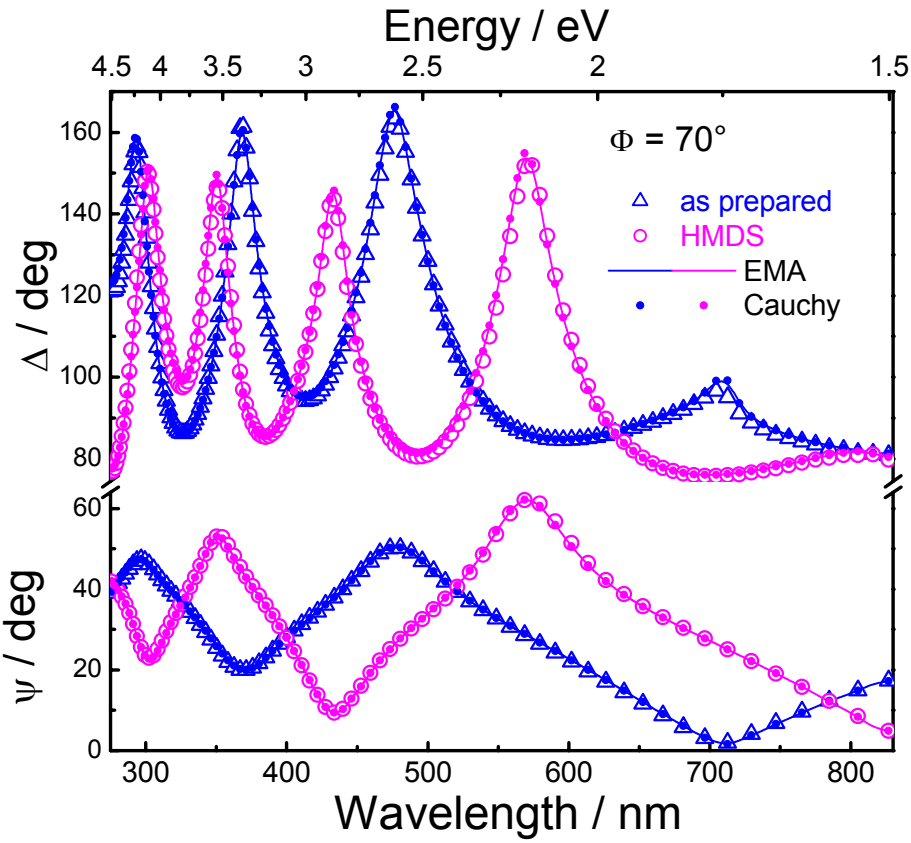


***Fig. 5.12.*** Experimental ψ and Δ spectra (for 70° incidence angle) of an as-prepared (triangles) and HMDS treated (circles) xerogel film, and the fitted spectra considering Cauchy (dotted lines) and EMA (solid lines) models.

Figure 5.13 shows the refractive indices obtained using the method described above. For comparison purposes literature data for the refractive index of $SiO_2$ [Pal85] are presented in the same plot. After treatment with HMDS the refractive index increases from 1.148±0.005 to 1.216±0.005 (values at =632.8 nm). The reason for this increase will be given later. At the same time, the thickness of the xerogel remains almost the same for as-prepared (570±5 nm) and HMDS (582±8 nm) films.

| Sample | Cauchy parameters | |
|---|---|---|
| | $a_n$ | $b_n$ x$10^3$ |
| As prepared | 1.146±3·$10^{-3}$ | 1.07±0.02 |
| HMDS treated | 1.212±5·$10^{-3}$ | 1.91±0.03 |

***Table 5.3.*** Values of, and errors in, the Cauchy parameters $a_n$ and $b_n$ for as-prepared and HMDS-treated films

The dielectric constant of a porous dielectric $\varepsilon_r$ can be determined using the Lorentz-Lorenz effective medium approximation (EMA) [Ohw97]:

$$\frac{\varepsilon_r - 1}{\varepsilon_r + 2} = f\frac{\varepsilon_a - 1}{\varepsilon_a + 2} + (1-f)\frac{\varepsilon_s - 1}{\varepsilon_s + 2} \qquad (5.2)$$

where ***f*** =*(pore volume/film volume)* is the relative film porosity and $\varepsilon_a$ and $\varepsilon_s$ are the dielectric constants of air and the film skeleton, respectively. Because $\varepsilon=n^2$, and $\varepsilon_a$ =1 the porosity of the films can be calculated from:

$$f = 1 - \left[\frac{n_r^2 - 1}{n_r^2 + 2}\right] \Big/ \left[\frac{n_s^2 - 1}{n_s^2 + 2}\right] \qquad (5.3)$$

where $n_r$ is the measured refractive index of the porous film and $n_s$ the refractive index of the skeleton.

Taking $n_s=n_{SiO2}$, the porosity ***f*** of the xerogel films can be determined by curve fitting of the experimental spectra. From the simulated spectra for the EMA model, shown in figure 5.12 by solid lines, values for the porosity of $f_{as\text{-}prepared}$=(65±3)% and $f_{HMDS}$=(50±3)% were

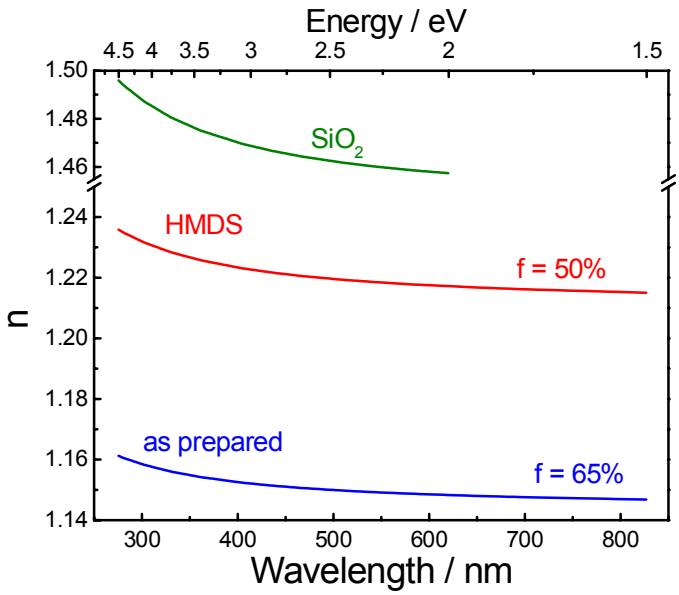


***Fig. 5.13.*** Refractive indices obtained by use of the Cauchy model for the as-prepared and HMDS-treated xerogel films, compared with the literature [Pal85] refractive index of $SiO_2$.

obtained. Very similar values (differences <2%) were obtained when other EMA models were used (Bruggeman and Maxwell-Garnet). Reduction of the porosity by ~15% also explains the increase of the refractive index by ~0.07, as is apparent from figure 5.13.

The rate of the porosity reduction as a function of HMDS treatment time was also established for samples treated for different times. An as-prepared sample was cut into several pieces which were exposed to HMDS for different time. In figure 5.14 it can be seen that the porosity will reduce by ~ 13% after 16 minutes of treatment. On the other hand, it is obvious that the most important decrease in porosity occurs after a few minutes, thereafter the porosity will decrease more slowly, showing a saturation tendency. This observation is in very good agreement with the rapid initial reaction of HMDS with silica found by FTIR investigations (see figure 5.8). The first reaction step is followed by a slower step reflected here by the slower rate of decreasing porosity with increasing treatment time above 5 minutes.

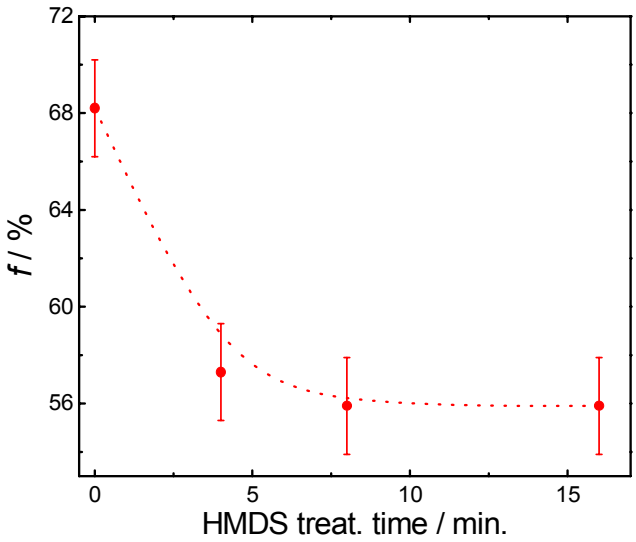


**Fig. 5.14.** Porosity reduction function of treatment time for a HMDS treated sample.

The same behaviour in the reduction of porosity was found for the treatments with all hydrophobisation substances investigated (HMDS, TMSDEA, and OTMSA). Since the initial pore volume was not exactly the same for all as-prepared samples, the relative porosity (*pore volume / initial pore volume*) decrease during the treatment with HMDS, TMSDEA, and OTMSA is shown in table 5.4. FTIR results

| Exposure time / min. | HMDS | TMSDEA | OTMSA |
|---|---|---|---|
| | *pore volume / initial pore volume* in % | | |
| 0.5 | 88 | not determ. (n.d) | n.d. |
| 1 | 87.9 | 82.1 | 95.4 |
| 2 | 85.8 | n.d. | n.d. |
| 4 | 83.8 | n.d | n.d. |
| 8 | 81.8 | 79 | 94.9 |
| 16 | 81.8 | 79.8 | 93.4 |
| 240 | n.d. | 77.7 | 92.7 |

***Table 5.4.*** Relative porosity decrease of xerogels films as a function of exposure time for different chemicals.

shown in the previous section indicate that TMSDEA has a higher reactivity than HMDS and OTMSA. In correspondence a faster porosity reduction was found for TMSDEA treated samples.

Even if the better hydrophobisation was achieved by TMSDEA treatment, the static dielectric constant was found to be lower for HMDS treated samples [Fru02]. This can be explained by the fact that for TMSDEA samples the reduction of the dielectric constant due to removal of water by hydrophobisation, is opposed to an increase due to porosity reduction. For HMDS the porosity reduction is smaller and the corresponding increase of the dielectric constant will be smaller than for TMSDEA. Once again the combination of FTIR and VASE proved to be a powerful method for the investigation of silica xerogels films.

By FTIR investigations (see section 5.2.1) it was observed that hydrophobisation is accompanied by important changes in IR spectra in the region of Si-O-Si vibrations (1000-1300 $cm^{-1}$ spectral range). In the following part the changes of the bands corresponding to Si-O-Si vibrations will be analysed in detail. Figure 5.15 a) and b) show by symbols the IR absorption spectra for as-prepared and HMDS treated xerogel film, respectively. The absorption spectra are derived from transmission measurements at normal incidence for unpolarised light. The spectra are dominated by a strong band at ~ 1080 $cm^{-1}$ and an asymmetric high frequency shoulder.

The region from 900 $cm^{-1}$ up to 1350 $cm^{-1}$ was decomposed in peaks using Gaussian functions. To decompose the region of Si-O-Si four Gaussian components were found to be sufficient to provide an acceptable fit. The Gaussian components obtained by curve fitting are plotted in figure 5.15. a) and b) by dotted lines while the fits obtained are plotted as solid lines. The region of Si-O-Si vibrations can be decomposed in peaks centred at 1081, 1132, 1154 and 1205 $cm^{-1}$.

The band at 1081 $cm^{-1}$ can be attributed to TO modes in silicon oxide corresponding to the asymmetrical stretch ($AS_1$) motion in which adjacent O atoms execute motion *in-phase* to each other [Kir88]. Kirk revealed that in a disordered system a second TO mode at ~ 1200 $cm^{-1}$ corresponding to *out of-phase* asymmetric stretching ($AS_2$) motion of adjacent O atoms exists. Under oblique incidence and p-polarised light the corresponding $AS_1$-LO and $AS_2$-LO will appear due to the Berreman effect [Ber63]. Kirk showed that due to disorder induced coupling of the modes an inversion of LO-TO splitting for the $AS_2$ mode will occur.

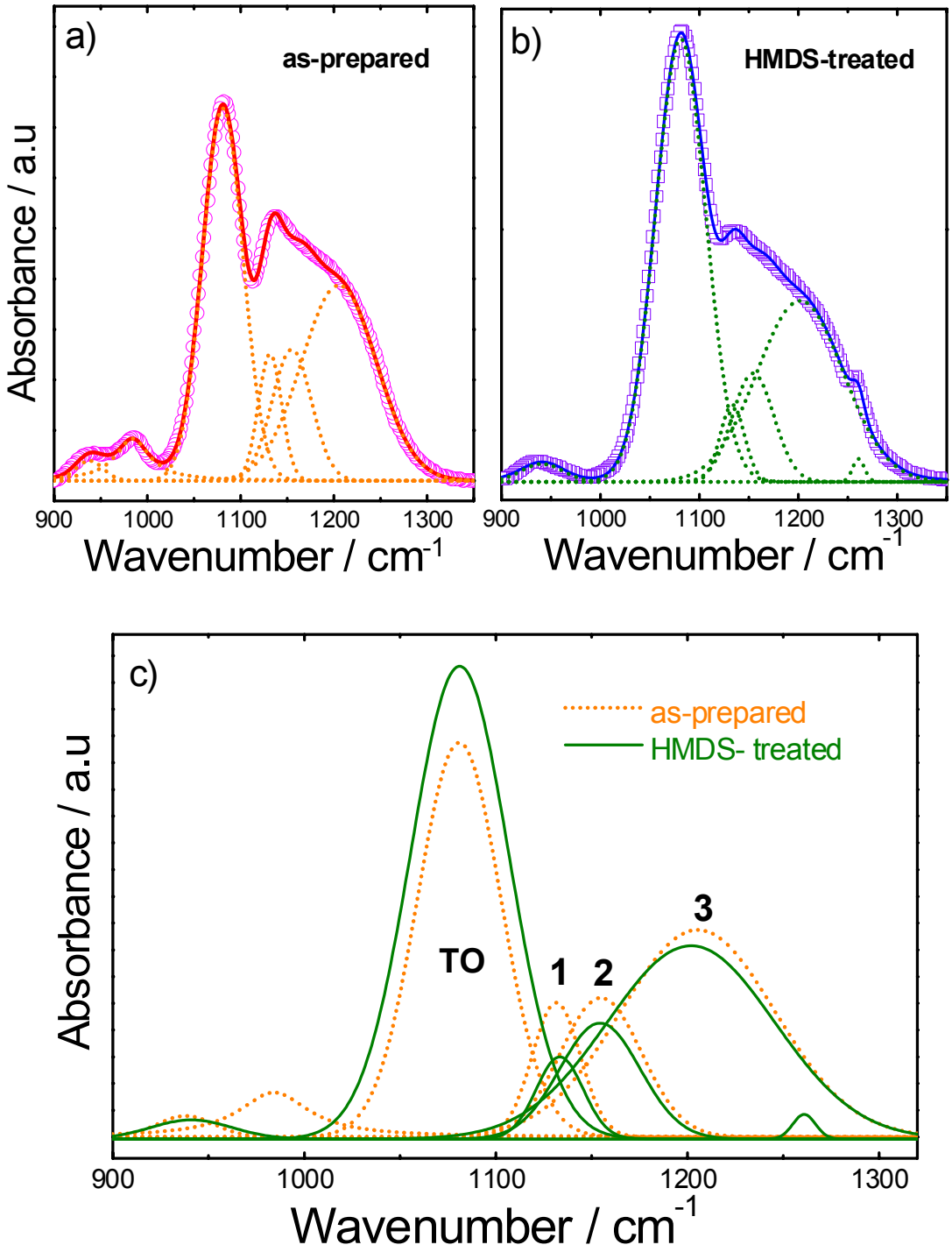


***Fig. 5.15.*** IR absorption spectra for as-prepared (a) and HMDS treated (b) xerogel films. The experimental points are plotted by symbols, the components obtained by curve fitting by dotted lines and the fits by solid lines. A comparison for the peaks for as-prepared and HMDS treated films is also given (c).

Almeida *et al.* [Alm90] indicated that in porous samples due to disorder the light is scattered in all directions inducing appearance of the modes having LO character even at normal incidence. Experimental evidence for this fact was found in

spectra of oxidised porous silicon [Wan99], and of aerosol-gel $SiO_2$ [Pri97] where TO and LO modes for $AS_1$ and $AS_2$ are present also in normal incidence IR spectra. However, it is suggested that in the vitreous materials due to long range structural disorder effects [Alm90] the modes have no pure LO or TO character. Under these conditions the dominant TO response expected at normal incidence will be mixed with modes having LO character. Moreover, it was demonstrated that the shoulder at 1100-1200 $cm^{-1}$ is connected with structural disorder [Mar98] or more directly to the porosity [Cho95, Maw97]. This shoulder was found to be more pronounced in porous gels than in thermal oxide [Alm90]. Chou *et al.* [Chou95] showed that materials with a larger absorption shoulder at 1200 $cm^{-1}$ have a smaller refractive index and a more porous structure.

In figure 5.15 c) the peaks obtained from curve fitting for as-prepared and HMDS treated films are plotted as dotted and solid lines, respectively. According to the literature [Kir88, Wan99, Pri97] the features at 1081, 1132, 1154 and 1205 $cm^{-1}$ can thus be attributed to $AS_1$-TO, $AS_2$-LO, $AS_2$-TO and $AS_1$-LO, respectively. It can be clearly seen that after HMDS treatment the features denoted by 1, 2, and 3 from the region of the shoulder decreased in intensities while the TO mode intensity increased. Considering the discussion above this behaviour suggests a reduction of porosity after HMDS treatment, in very good agreement with VASE results. Porosity reduction is correlated with changes in the silica network structure, namely increasing number of Si-O-Si bridges reflected by increasing TO, accompanied by reduction of the shoulder at 1150-1200 $cm^{-1}$ reflecting porosity reduction and improving order in the system. Mechanisms which can induce these changes are proposed in the next section.

Besides the changes in Si-O-Si structure in the spectra from figure 5.15 c) disappearance of the mode at 985 $cm^{-1}$ and appearance of the mode at 1256 $cm^{-1}$ after HMDS treatment can be observed. This reflects the replacement of the isolated -OH groups by TMS groups during the hydrophobisation reaction.

### 5.2.3. Ellipsometric Porosimetry (EP) results.

Ellipsometric porosimetry was used to confirm the reduction in porosity after HMDS treatment obtained using VASE [Him02a] as was shown in the previous section. The principle behind EP is to use changes in the optical characteristics of porous films during adsorption and/or desorption of an adsorbate in/from the pores, and to determine the amount of adsorbate (toluene in our work) inside the pores. Besides porosity values, important information about pore-size distribution (PSD) and pore interconnectivity can be obtained. A detailed description of the method can be found elsewhere [Bak00a, Bak00b]. In practice equation (5.2) can again be used, because the pores are filled with an adsorptive liquid of known dielectric constant. Measurements performed for different adsorbates showed that the approximation $n_s \cong n_{SiO2}$ was reasonable.

The dependence of adsorptive volume on the relative pressure $P/P_0$ is an adsorptive isotherm, which is used to calculate PSD [Bak00a]. Figure 5.16 a) shows the adsorption and desorption isotherms of the toluene in/from the as-prepared and HMDS-treated xerogel films. Toluene was used as adsorbed species, because it has a contact angle close to zero for the xerogel films under study. The hysteresis behaviour observed is caused by capillary condensation and desorption of the toluene from the porous film [Bak00b]. The porosity is determined from the saturation values of the isotherms in figure 5.16 a), and is called the "open" porosity, because it refers to the open pores which are accessible to toluene. The values of the open porosity from the figure are very close to the values of the "full" porosity obtained by VASE (65% and 50% for as-prepared and HMDS treated films, respectively), which means that nearly all the pores are interconnected.

The skeleton refractive index was, moreover, found to be equal to that of silicon oxide ($n_{skeleton} \approx n_{SiO2}$=1.46) for both untreated and HMDS-treated films. This means there is at most a negligible number of closed pores in the films, because their presence would reduce the skeleton refractive index (the toluene cannot penetrate the closed pores). This is another indication of the interconnectivity between the pores. Figure 5.16 b) shows the PSD obtained from the desorption isotherms by use of the Kelvin and BET equations (a commonly used approach in adsorption porosimetry [Bak00a]). It is apparent that some micropores in the as-prepared sample

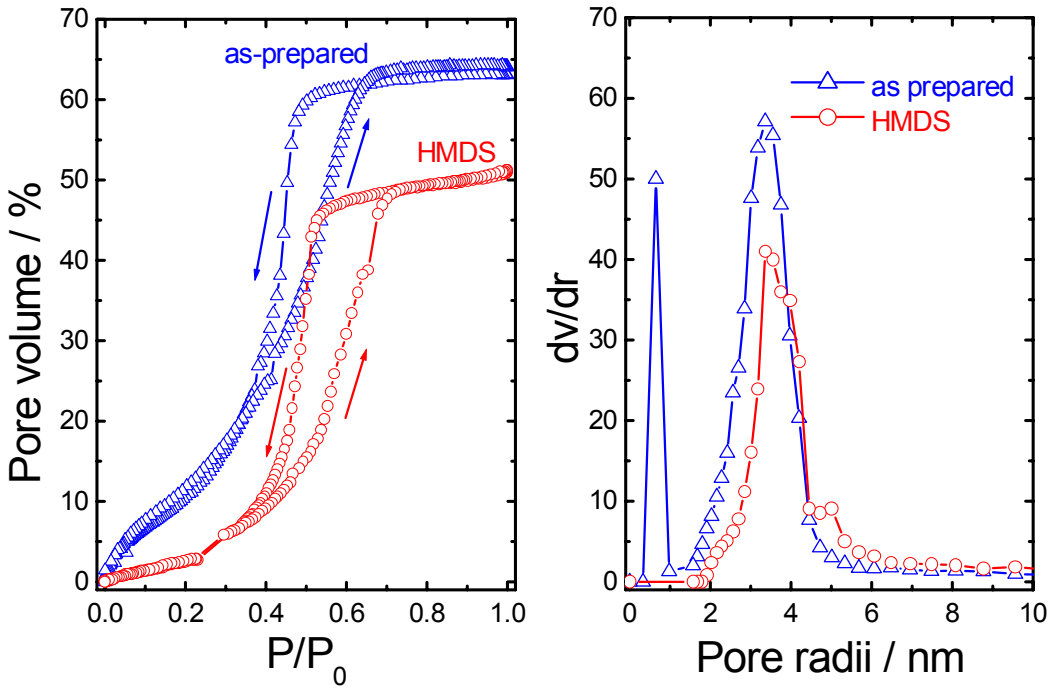


**Fig. 5.16.** (a) Adsorption-desorption isotherms of toluene in/from the pores of the xerogel films. The toluene condenses in the pores at vapour pressures (P) less than the equilibrium pressure ($P_0$). (b) Pore-size distributions in the xerogel films before and after HMDS-treatment, calculated from the desorption isotherms.

disappear after treatment with HMDS. Pores with dimensions smaller than 2 nm were analysed by use of Dubinin-Radushkevich theory [Gre82] which enables determination of the mean pore size of the micropores. These micropores are closed by HMDS treatment by load of TMS groups on the surface in agreement with the results published by Fuji *et al.* [Fuj99]. Covering of mesopore surfaces by TMS groups can decrease the porosity by a few percent, but cannot explain the significant reduction of porosity by ~ 15%.

The mean pore size of 3-4 nm is in good agreement with the dimensions of the pores in the HRTEM image in figure 5.17. The HRTEM images for silica xerogels

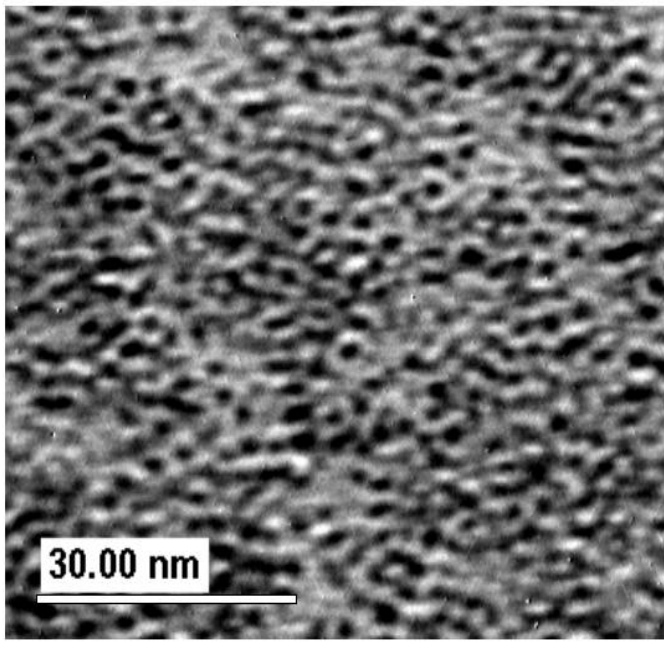


***Fig. 5.17.*** HRTEM image of a silica xerogel film.

films were recorded by means of a platinum replica of the surface of the film.

The reduced porosity of HMDS-treated films is assumed to be the result of several chemical reactions occurring in the presence of HMDS and its by-products. Ammonia, in particular, is known for its catalytic effect, for instance on the condensation reaction which could occur during HMDS treatment. On the other hand, the reaction of neighbouring TMS groups liberating hexamethyldisiloxane (HMDSO) and forming Si-O-Si bridges was observed by Slavov *et al.* [Sla00] during the reaction of HMDS with silica at 200 °C:

$$2\ [\equiv Si\text{-}O\text{-}Si(CH_3)_3] \rightarrow ((CH_3)_3Si)_2O + \equiv Si\text{-}O\text{-}Si\equiv \qquad (5.4)$$

This might explain the reduction in the porosity in our films, because the pendant $Si\text{-}O\text{-}Si(CH_3)_3$ groups are transformed into siloxane species. Thus the structure of the xerogel becomes more compact, reflecting the reduction of porosity found by VASE and EP results. This hypothesis is confirmed by FTIR results presented in the previous section. Further investigations are needed to establish the contributions of the condensation reaction and of the reaction described by equation (5.4) to the formation of Si-O-Si bridges.

### 5.2.4. FTIR investigation of cap-layer deposition on xerogel films.

In the integration process which include Cu metallization the xerogel films must be protected during chemical and mechanical polishing and mask pattering in order to ensure the stability of their advantageous electrical characteristics [Sch01]. One solution to overcome this problem is deposition of an insulating $SiO_2$ or $Si_3N_4$ cap layer on top of xerogel films. Plasma Enhanced Chemical Vapour Deposition (PECVD) was used to deposit such protective cap layers.

FTIR spectroscopy was employed to monitor the influence of cap layer deposition on the chemical composition of the xerogel films. Very important for applications is to preserve the hydrophobic character of the films after depositing a cap layer. Absorbance IR spectra in figure 5.18 show no significant variation of symmetrical and asymmetrical stretching vibrations at 2905 and 2962 $cm^{-1}$ of C-H in TMS groups after deposition of a $Si_3N_4$ layer. A very small reduction of the peak intensity after deposition of $SiO_2$ cap layer was observed. This indicates that the PECVD cap layer deposition process has not removed the methyl groups introduced during HMDS treatment and the hydrophobic nature of the porous xerogel survives. In accordance with FTIR results deposition of cap layers on xerogel films was found to have negligible effects on the electrical properties [Sch01].

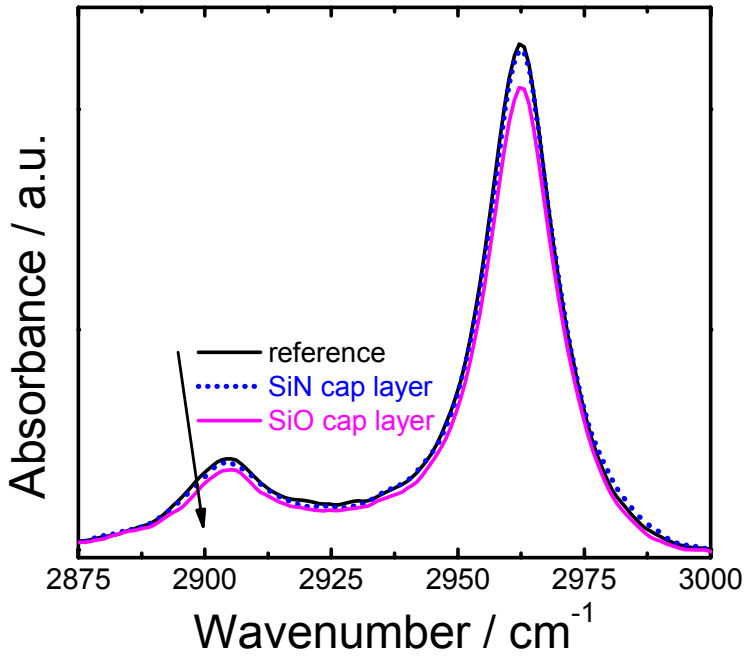


***Fig. 5.18.*** IR absorption spectra of non-capped, SiN and SiO capped xerogel in the region of CH stretching vibrations.

# 5.3. Contributions to dielectric constant.

In this section the electronic and ionic contributions to the static dielectric constant of silica xerogels films were determined from the refractive index in the visible spectral range measured by VASE and from transmission infrared spectra. The static dielectric constant $\varepsilon$, determined by C-V measurements at 1 MHz consists of electronic $\Delta\varepsilon_e$, ionic $\Delta\varepsilon_i$ and configurational $\Delta\varepsilon_c$ contributions [Han98]:

$$\varepsilon = 1 + \Delta\varepsilon_e + \Delta\varepsilon_i + \Delta\varepsilon_c \tag{5.5}$$

where 1 is the dielectric constant of vacuum. The electronic contribution $\Delta\varepsilon_e$ arises from the polarization generated by the distortion of the electron clouds, the ionic contribution $\Delta\varepsilon_i$ is caused by the ionic motions and the configurational contribution $\Delta\varepsilon_c$ stems from polar molecules which try to align with the applied electric field [Han98]. When the frequency of the applied radiation will exceed the characteristic frequency of the motion which contributes to the polarization, this motion cannot further follow the electric field and consequently the dielectric constant is reduced with increasing frequency. In the infrared range the dielectric constant above vacuum dielectric constant consists of ionic and electronic contributions while in the visible range only the electronic part contributes [Lin96].

The dielectric constant $\varepsilon$ of a material is related to its optical constants as follows:

$$\varepsilon = \varepsilon_1 + i\varepsilon_2 = (n + ik)^2 = n^2 - k^2 + i2nk \tag{5.6}$$

where $\varepsilon_1$ and $\varepsilon_2$ are the real and imaginary part of $\varepsilon$, n is the refractive index and k the extinction coefficient. The magnitude of the dielectric constant then is:

$$\bar{\varepsilon} = \sqrt{\varepsilon_1^2 + \varepsilon_2^2} \tag{5.7}$$

Xerogel films produced using different aging / hydrophobisation conditions were used to investigate the contributions to the static dielectric constant determined from C-V characteristics. As can be seen in Table 5.5 the aging was realized in air, solvent or $H_2O$/solvent atmosphere and the hydrophobisation was done in HMDS vapours for 10 minutes or 24 hours. According to the preparation conditions the samples were labeled A24, S10, S24 and W24, respectively.

| Sample | Preparation: (aging / hydrophobisation) | Thickness/nm ± 10 nm | n (632.8 nm) ± $5 \cdot 10^{-3}$ | Porosity % ± 2% | $\Delta\varepsilon_e$ ± 0.01 | $\Delta\varepsilon_i^{650}$ ± 0.1 | $\varepsilon_{static}$ ± 0.1 |
|---|---|---|---|---|---|---|---|
| A24 | Air / 24h HMDS | 444 | 1.27 | 39.8 | 0.61 | 0.42 | 2.6 |
| S10 | solvent / 10 min HMDS | 509 | 1.224 | 49.5 | 0.5 | 0.32 | 2.6 |
| S24 | solvent / 24 h HMDS | 509 | 1.237 | 47 | 0.53 | 0.33 | 2.31 |
| W24 | Water + solvent / 24h HMDS | 582 | 1.198 | 55 | 0.44 | 0.29 | 2 |

***Tabel 5.5*** Aging / hydrophobisation conditions; thickness, refractive index and porosity determined from VASE; as well as electronic and ionic contributions to the static dielectric constant for the samples A24, S10, S24 and W24.

The thickness, optical constants and porosity of the xerogels films were determined from VASE using the method presented in section 5.1. Since the films are transparent (k=0) in the visible range, the dielectric constant is the square of the refractive index ($\varepsilon=n^2$) so that the electronic contribution can be written as:

$$\Delta\varepsilon_e = n^2 - 1 \tag{5.8}$$

In the calculation of $\Delta\varepsilon_e$ the refractive index at 632.8 nm was used for consistence with literature (632.8 nm is a wavelength commonly used in one-wavelength ellipsometry) [Lin96, Han98, Han99, Kim01].

The dielectric constant in the visible range determined from the refractive index and the "static" dielectric constant at 1 MHz are plotted in the figure 5.19

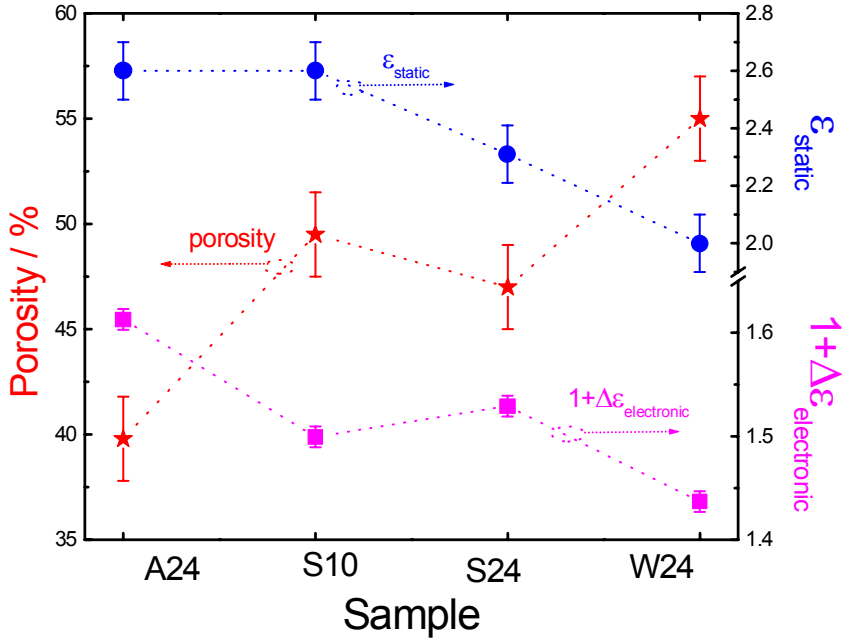


***Fig 5.19*** Porosity (stars), electronic contribution including vacuum dielectric constant (squares) and static dielectric constant (circles) for the samples A24, S10, S24 and W24 respectively.

together with the porosity of the films. It can be observed that the electronic contribution is directly influenced by the porosity, because it is calculated using the refractive index: samples with higher porosity will have a lower electronic contribution to the dielectric constants. On the other hand, it can be seen that there is not a direct connection between the static dielectric constant and porosity.

The dielectric constant in the IR range $\varepsilon_{IR}$ consists of vacuum, electronic and ionic contributions. $\varepsilon_{IR}$ was calculated from IR transmission spectra describing the film as a Lorentz layer consisting of several absorption peaks:

$$\varepsilon_{IR}(h\nu) = \varepsilon_{1\infty} + \sum_k \frac{A_k}{E_k^2 - (h\nu)^2 - iB_k h\nu} \tag{5.9}$$

where k is numbering the oscillators, $A_k$, $E_k$ and $B_k$ are the amplitude, center energy and broadening of each oscillator and $\varepsilon_{1\infty}$ is an additional offset [Joh95]. The model of dielectric constants described by equation (5.9) fulfills the Kramer-Kronig dispersion relations [Joh95].

Using the model described above the optical constants of the films in the IR range were determined. Using equations (5.6) and (5.7) the magnitude of the dielectric constant $\varepsilon_{IR}$ in 650-4000 $cm^{-1}$ IR range was calculated. $\varepsilon_{IR}$ for the films under investigation are plotted in figure 5.20. As can be observed in the figure $\varepsilon_{IR}$ at

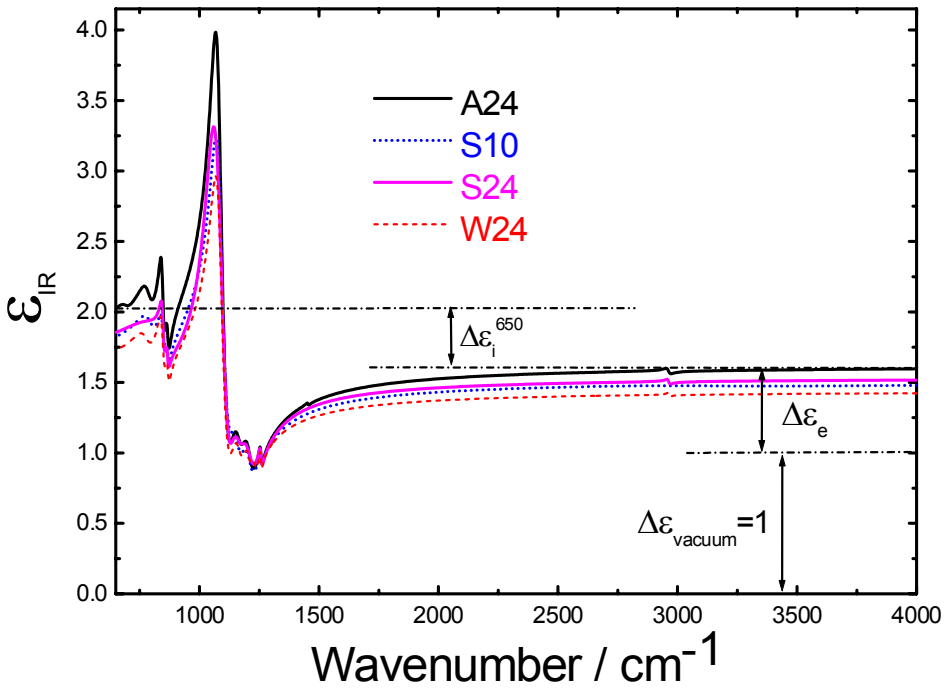


***Fig 5.20*** Dielectric constant in IR range derived from IR transmission spectra.

650 $cm^{-1}$ consist of vacuum (1), electronic ($\Delta\varepsilon_e$) and ionic contributions ($\Delta\varepsilon_i^{650}$). The values for the ionic contribution at 650 $cm^{-1}$ ($\Delta\varepsilon_i^{650}$) are presented in Table 5.5. It should be noted that these values do not contain the whole ionic contribution because vibrations with characteristic frequencies below 650 $cm^{-1}$ were not included in the model (measurements in far IR range were not performed). It can be observed that the ionic contribution decreases slightly with increasing porosity because the films with higher porosity have a smaller density. It can be also pointed out that the ionic contribution is smaller than the electronic one for all the films. The region at about 1100-1200 $cm^{-1}$ where the dielectric constant is slightly smaller than 1 corresponds to the strong absorptions by Si-O vibrations. Such effect was also observed for fluorinated and carbon-incorporated silicon oxide films [Lim96, Han98, Kim01].

Figure 5.21 summarizes in form of a histogram the contribution to the static dielectric constant. The difference between the level of static dielectric constant and the upper level of $\Delta\varepsilon_i$ consists of the remaining ionic contribution in far IR range and the configurational contribution. Because the ionic contributions at 650 $cm^{-1}$ have

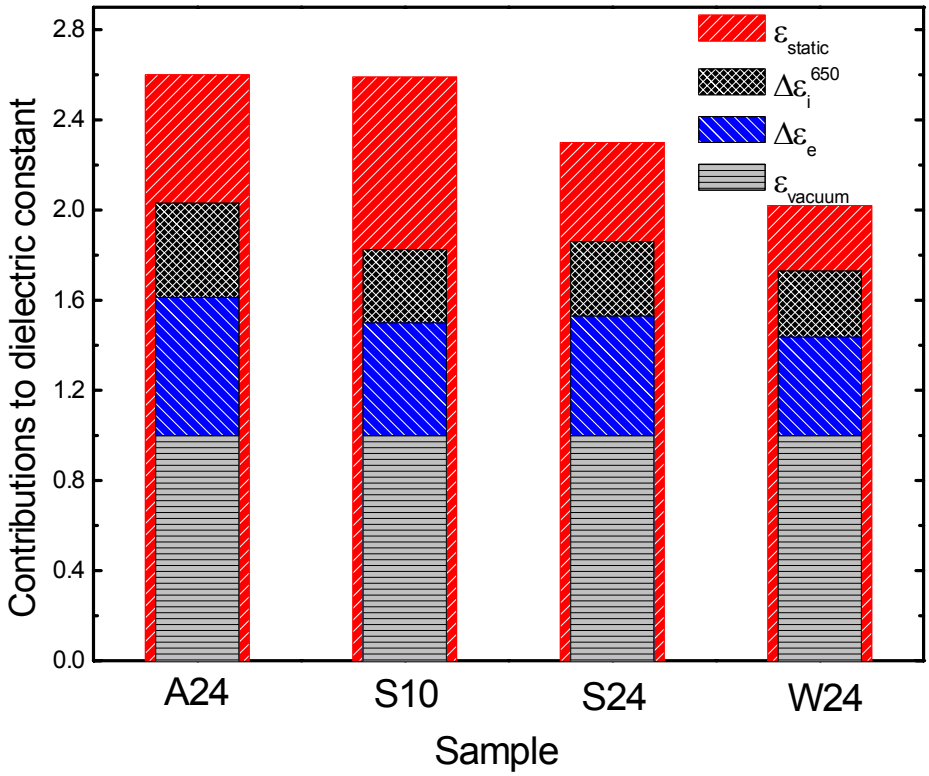


***Fig. 5.21*** Contribution to the static dielectric constant.

close values (minimum 0.29 and maximum 0.42) it is expected that the additional ionic contribution in the far IR range have close values, too. In these conditions the main difference between static dielectric constants (minimum 2 and maximum 2.6) must arise from different configurational contributions.

From figure 5.21 the highest configurational contribution is expected for sample S10 and the lowest for sample W24. This is in good agreement with the fact that for sample S10, which was hydrophobised only for 10 minutes, more –OH groups are present in the pores. Consequently the configurational contribution is expected to be high due to polarity of these groups. On the other hand, for sample W24 aged in $H_2O$/solvent the addition of water in the aging process enhances the polycondensation reaction [Fru02b] so that the number of “unlinked” edges is expected to be reduced. For such a sample the configurational contribution is thus lower because of a smaller number of –OH species.

# Chapter 6

# Conclusions

Combination of IR spectroscopy, ellipsometry and HRTEM was successfully applied for characterization of the surface and interface oxide layers in high temperature Si-Si bonded wafers. It was shown that non-destructive IR spectroscopy allows buried interface oxide layer thicknesses to be precisely determined as was judged from comparison with HRTEM measurements. The role of the chemical species adsorbed at the interface and of the interstitial oxygen in Si bulk, in the buried oxide formation was established. The behaviour of LO and TO modes with annealing is in agreement with an increase of Si-O-Si bond angle and a corresponding strain relaxation in the surface oxide layer. An overview of the method applied is shown in figure 6.1.

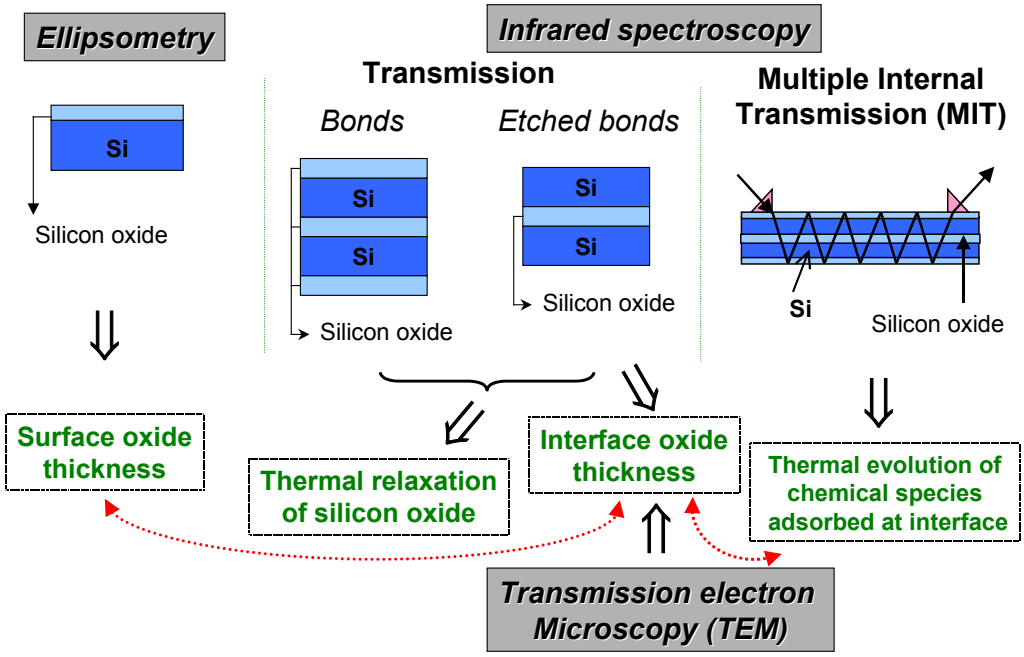


***Fig. 6.1.*** Schematical presentation of the procedures applied for characterisation of surface and interface oxide layers in Si-Si bonded wafers.

A non-destructive two-coupling prisms MIT technique was applied for IR characterisation of bonded interface in low temperature Si-Si bonded wafers. The IR spectra were recorded *in situ* during annealing of RT bonded Si-Si samples produced using different chemical pre-treatments of the Si wafers and *ex situ* for 200° and

400°C annealed bonded wafers. The rearrangement of the atoms at the buried interface obtained from IR spectra suggests chemical reactions which explain how the bonding of Si wafers is realised. Corresponding bonding mechanisms were proposed for low temperature Si-Si bonded wafers with both thin and thick interfacial oxide layers. It was found that the best bonding at low temperatures is realised between Si wafers covered with native oxide together with Si wafers covered with thick thermal oxide in the case when both wafers are treated by RIE oxygen plasma.

Optical and structural properties of silica xerogels films were studied by spectroscopic ellipsometry and IR spectroscopy in dependence of their conditions of growth during a sol-gel spin coating process. The optical constants and the thicknesses of the films were simultaneously determined from the curve fitting of the ellipsometric data describing the films as a Cauchy layer. Further, using these thicknesses, the porosity of the films was calculated applying effective medium approximation. Ellipsometric Porosimetry was used to confirm the porosity values obtained using VASE results.

The effects of the hydrophobisation process on the properties of the xerogels films were also investigated. HMDS was found to be the best hydrophobisation agent. Porosity of silica xerogel films is reduced by ~15% after hydrophobisation treatment, because of the changes in Si-O-Si network as revealed by FTIR. Agreement between "full" porosity (from VASE) and "open" porosity (from EP) values suggests that most of the pores are interconnected.

The electronic contribution to dielectric constant was estimated in visible range from the refractive index while the ionic contribution was estimated from IR transmission spectra. For the films under study with porosities in the range 40-55%, the main difference between static dielectric constant was found to arise from the configurational contribution.

The hydrophobic character, the low refractive index and dielectric constants recommend the xerogel films for dielectric applications.

# References

**[Ahn90]** K.-Y. Ahn, R. Stegl, T.Y. Tan, U. Gösele, and P. Smith – Appl.Phys. A 50, 85, (1990).

**[Alm90]** R.M. Almeida, and C.G. Pantano – J. Appl. Phys. 68, 4225, (1990).

**[Ami00]** P. Amirfeiz, S. Bengtsson, E. Zanghellini, and L. Börjesson – J. Electrochem. Soc. 147, 2693, (2000).

**[And00]** E. San Andres, A. del Padro, F.L. Martinez, I. Martil, D. Bravo and F.J. Lopez – J.Appl. Phys. 87, 1187, (2000).

**[Aoi97]** N. Aoi, – Jpn. J. Appl. Phys. 36, 1355, (1997).

**[Azz92]** R.M.A. Azzam, and M.M. Bashara – Ellipsometry and polarized light, Elsevier, North-Holland (1992).

**[Bak00a]** M.R. Baklanov, K.P. Mogilnikov, V.G. Polovinkin, and F.N. Dutsev – J. Vac. Sci. Technol. B 18, 1385, (2000).

**[Bak00b]** M.R. Baklanov, and K.P. Mogilnikov – Mat. Res. Soc. Symp. Proc., vol 612, D4.2.1., (2000).

**[Ban94]** C.N. Banwell, and E.M. McCash – Fundamentals of molecular Spectroscopy, McGraw-Hill Book Company (1994).

**[Bau96]** G. Bauer, and W. Richter – Optical Characterisation of Epitaxial Semiconductor Layers, Springer, (1996).

**[Ben00]** F. Benitez, E. Martinez, and J. Esteve – Thin Solid Films 377-378, 109, (2002).

**[Ber63]** D.W. Berreman – Phys. Rev. 130, 6, (1990).

**[Bri90]** C.J. Brinker and G.W. Scherer – Sol-Gel Science: Physics and Chemistry of Sol-Gel Processing, (Academic, New York, 1990).

**[Cha86]** Y.J. Chabal, – Surf. Sci. 168, 594, (1986).

**[Cha88]** Y.J. Chabal – Surf. Sci. Rep., 8, 211, (1988).

**[Cha95]** Y.J. Chabal, M.A. Hines, and D. Feijoo – J. Vac. Sci. Technol. A, 13, 1719, (1995).

**[Cho95]** J.S. Chou, and S.C. Lee – Appl. Phys. Lett. 77, 1805, (1995).

**[Cri01]** S. Cristoloveanu – Solid-State Electronics 45, 1403, (2001).

**[Dev96]** R.A.B. Devine – Appl. Phys. Lett. 68, 3108, (1996).

**[Fei94]** D. Feijoo, Y.J. Chabal, and S.B. Christman – Appl. Phys. Lett. 65, 2548, (1994).

**[Fru02]** S.Fruehauf, I.Streiter, S.E.Schulz, E.Brendler, C.Himcinschi, M.Friedrich, T.Gessner, D.R.T.Zahn – Conference Proceedings ULSI XVII, 287, edited by Material Research Society, (2002).

**[Fru02b]** S.Fruehauf, I.Streiter, R. Puschmann, S.E.Schulz, C.Himcinschi, C.M. Flannery, T.Gessner, and D.R.T.Zahn – *to be published* in Proceedings of Advanced Metallization Conference (AMC), October 1-3, 2002, San Diego, USA.

**[Fuj99]** M. Fuji, H. Iwata, T. Takei, T. Watanabe, and M. Chikazawa – Adv. Powder Technol. 10, 187, (1999).

**[Gal79]** F. L. Galeener – Phys. Rev B 19 (1979) 4292.

**[Ges00]** T. Gessner, D.R.T. Zahn, and W Dötzel – "Microelectronic-compatible scanner arrays of high frequency" subproiect C4 SFB 379 in Annual Report 2000 - Center of Microtechnologies Chemnitz.

**[Gös99]** U Gösele, Y. Bluhm, G. Kästner, P. Kopperschmidt, G. Kräuter, R. Scholz, L.-J. Huang, Y.-L. Chao, and T.H. Lee, – J. Vac. Sci. Technol. A 17,.1145, (1999).

**[Gre82]** S.J. Gregg, and K.S.V. Sing – Adsorption Surface Area and Porosity, Academic Press, (1982).

**[Gri86]** P.R. Griffiths, and J.A. de Haseth – Fourier transform infrared spectrometry, Wiley, (1986).

**[Gun00]** V.M. Gunko, M.S. Vedamuthu, G.L. Henderson and J.P. Blitz – J of Coll and Interface Sci 228, 157, (2000).

**[Gur99]** A. B. Gurevich, M. K. Weldon, Y. J. Chabal, R. L. Opila, and J. Sapjeta – Appl. Phys. Lett. 74, 1257, (1999).

**[Han98]** S.M. Han, and E.S. Aydil – J. Appl. Phys. 83, 2172, (1998).

**[Han99]** B. Hanyaloglu, A. Aydinli, M. Oye, and E.S. Aydil – Appl. Phys. Lett. 74, 606, (1999).

**[Han00]** W. Han, J. Yu, and Q. Wang – J. Appl. Phys. 88, 4404, (2000).

**[Han01]** D.M. Hansen, C.E. Albaugh, P.D. Moran, and T.F. Kuech – J. Appl. Phys., 90, 5991, (2001).

**[Hau94]** S. Haukka, and A. Root – J. Phys. Chem. 98, 1695, (1994).

**[Hav98]** R. H. Havemann *et al.* – Mater. Res. Soc. Symp. Proc. 511, 3, (1998).

**[Him01a]** C.Himcinschi, A.Milekhin, M.Friedrich, K.Hiller, M.Wiemer, T.Gessner, S. Schulze, D.R.T.Zahn, – Appl. Surf. Sci., 175-176, 715, (2001).

**[Him01b]** C.Himcinschi, A.Milekhin, M.Friedrich, K.Hiller, M.Wiemer, T.Gessner, S. Schulze, and D.R.T.Zahn – J. Appl. Phys. 89, 1992, (2001).

**[Him01c]** C. Himcinschi, M. Friedrich, C. Murray, I. Streiter, S. E. Schulz, T. Gessner, and D.R.T. Zahn – Semicond. Sci. Technol. 16, 806, (2001).

**[Him02a]** C. Himcinschi, M. Friedrich, S. Frühauf, I. Streiter, S. E. Schulz, T. Gessner, and D.R.T. Zahn – Analytical Bioanalytical Chem. 374, 654, (2002).

**[Him02b]** C.Himcinschi, M.Friedrich, K.Hiller, T.Gessner, and D.R.T.Zahn –, CAS 2002 Proceedings, vol. 2, 271-274 (published by IEEE).

**[Hir02]** C.J. Hirschmugl – Surface Science 500, 577, (2002).

**[Ish97]** K. Ishikava, U. Uchiyama, H. Ogawa, and S. Fujimura – Appl. Surf. Sci. 117/118, 212, (1997).

**[Jel92]** G.E. Jellison Jr. – Opt. Mater **1**, 41, (1992).

**[Jin97]** C. Jin, J.D. Luttmer, D.M. Smith, and T.A. Ramos – MRS Bull., October, 39 (1997).

**[Joh95]** B. Johs and C. Herzinger – Guide to using WVASE32, J.A. Woolan Co., Inc. Lincoln (1995).

**[Kim01]** J.Y. Kim, M.S. Hwang, Y.H. Kim, H.J. Kim, and Y. Lee – J. Appl. Phys. 90, 2469, (2001).

**[Kir88]** C.T. Kirk – Phys. Rev. B 38, 1255, (1988).

**[Krä98]** G. Kräuter, A. Schumacher, and U. Gösele – Sens. Actuators A 70, 271, (1998).

**[Kyt97]** A. Kytokivi, and S. Haukka, – J. Phys. Chem. B 101, 10365, (1997).

**[Leh82]** A. Lehman, L. Schumann, and K. Hubner – Phys. Status Solidi B 117, 689, (1982).

**[Lim96]** S.W. Lim, Y. Shimogaki, Y. Nakano, K. Tada, and H. Komiyama – Jpn. J. Appl. Phys. 35, 1468, (1996).

**[Luc87]** G. Lucovsky, M.J. Manitini, J.K. Srivastava, and E.A. Irene – J. Vac. Sci. Technol. B 5, 530, (1987).

**[Mar98]** J.R. Martinez, F. Ruiz, Y.V. Vorobiev, F. Perez-Robles, and J. Gonzales-Hernandez – J. Chem. Phys. 109, 7511, (1998).

**[Mas88]** W.P. Maszara, G. Goetz, A. Gaviglia, and J.B. McKitterick – J. Appl. Phys. 64, 4943 (1988).

**[Maw97]** D.B. Mawhinney, J.A. Glass Jr., and J.T. Yates Jr. – J. Phys. Chem. B 101, 1202, (1997).

**[Mic84]** T.A. Michalske and B.C. Bunker – J. Appl. Phys. 56, 2686 (1984).

**[Mil00]** A. Milekhin, M. Friedrich, K. Hiller, M. Wiemer, T.Gessner, and D.R.T. Zahn, J. Vac. Sci. Technol. B, 18, 1392, (2000).

**[Mil99]** A. Milekhin, M. Friedrich, K. Hiller, M. Wiemer, T.Gessner, and D.R.T. Zahn, J. Vac. Sci. Technol. B, 17, 1773, (1999).

**[Mur02]** C. Murray, C. Flannery, I. Streiter, S.E. Schulz, M.R. Baklanov, K.P. Mogilnikov, C. Himcinschi, M. Friedrich, D.R.T. Zahn, and T. Gessner, – Microelectronics Eng. 60, 133, (2002).

**[Nit99]** S.V. Nitta, V. Pisupatti, A. Jain, P.C. Wayner Jr., W.N. Gill and J.L. Plawsky – J. Vac. Sci. Technol. B 17, 205, (1999).

**[Oga92]** H. Ogawa, T. Hattori, – Appl. Phys. Lett. 61, 579, (1992).

**[Ohw97]** T. Ohwaki, M. Takeda, and Y. Takai – Jpn. J. Appl. Phys., 36, 5507, (1997)

**[Pal85]** Handbook of optical constants of Solids, edited by E.D. Palik, Academic Press, New York, (1985).

**[Par93]** T.M. Parrill – J. Mater. Res. 9, 723, (1994).

**[Pri97]** N. Primeau, C. Vautey, and M. Langlet – Thin Solid Films 310, 47, (1997).

**[Que00]** K.T. Queeney, M.K. Weldon, J.P. Chang, Y.J. Chabal, A.B. Gurevich, J. Sapjeta, and R.L. Opila, – J. Appl. Phys., 87, 1322, (2000).

**[Rei95]** M. Reiche, S. Hopfe, U. Gösele, and Q.Y. Tong – Appl. Phys. A, 61, 101, (1995).

**[Sas95]** A. Sassella, P. Lucarno, A. Borghesi, F. Corni, S. Rojas, and L. Zanotti – J. Non. Cryst. Solids 187, 395, (1995).

**[Sch01]** S.E. Schulz, H. Koerner, C. Murray, I. Streiter, and T. Gessner – Microelectronic Engineering 55, 45, (2001).

**[Sko92]** D.A. Skoog, and J.L. Leary – Principles of Instrumental Analysis, Saunders College Publisher, (1992).

**[Sla00]** S.V. Slavov, A.R. Sanger, and K.T. Chuang – J. Phys. Chem. B 104, 983, (2000).

**[Sun02a]** L. Sun, J-C. Fouere, and C. Pickering – Compound Semiconductor, vol. 8, no. 5, 49 (2002).

**[Sun02b]** T. Suni, K. Henttinen, I. Suni, and J. Mäkinen, – J. Electrochem. Soc. 149, G348, (2002).

**[The90]** J.A. Theil, D.V. Tsu, M.W. Watkins, S.S. Kim, and G. Lucovsky, – J. Vac. Sci. Technol. A 8, 1374, (1990).

**[Ton98]** Q.-Y. Tong, W.J. Kim, T.-H. Lee, and U Gösele – Electrochem. Sol. Stat. Lett. 1, 52, (1998).

**[Ton99]** Q.Y. Tong and U. Gösele – Semiconductor Wafer Bonding: Science and Technology (The Electrochemical Society, New York, 1999).

**[Wan99]** J.W. Wang, B. Zou, and M.A. El-Sayed – J. Molec. Str. 508, 87, (1999).

**[Wel96a]** M.K. Weldon, V.E. Marsico, Y.J. Chabal, D.R. Hamann, S.B. Christman, and E.E. Chaban, – Surf. Sci. 368, 163, (1996).

**[Wel96b]** M.K. Weldon, Y.J. Chabal, D.R. Hamann, S.B. Christman, E.E. Chaban, and L.C. Feldman, – J. Vac. Sci. Technol. B, 14, 3095, (1996).

**[Win98]** T. Winkler, S.E. Schulz and T. Gessner, – MRS Symp. Proc. ULSI XII, MRS Warrendale PA, 347-351, (1998).

**[Woo99]** J.A. Woollam, B. Johs, C.M. Herzinger, J.N. Hilfiker, R. Synowicki, and C. Bungay – SPIE Proceedings, CR72, (1999).

**[Yu99]** Yu and Cardona – Fundamentals of Semiconductors, Springer, (1999).

# List of tables

***Table 2.1.*** Description of the pre-treatments of the Si wafers before room temperature bonding. ***10***

***Table 4.1.*** Description of the pre-treatments of the Si wafers before room temperature bonding. ***49***

***Table 5.1.*** Variation of the parameter of the sol-gel spin coating process: mixing time, aging time and spin speed. ***63***

***Table 5.2.*** The values and the errors of the optical parameters, thickness and porosity determined by fitting of the ellipsometric data using Cauchy and EMA models. ***63***

***Table 5.3.*** Values of, and errors in, the Cauchy parameters $a_n$ and $b_n$ for as-prepared and HMDS-treated films. ***74***

***Table 5.4.*** Relative porosity decrease of xerogels films function of exposure time for different chemicals. ***75***

***Tabel 5.5*** Aging / hydrophobisation conditions; thickness, refractive index and porosity determined from VASE; as well as electronic and ionic contributions to the static dielectric constant for the samples A24, S10, S24 and W24. ***84***

# List of figures

***Fig. 2.1.*** Schematic representation of the IR imaging system used to control the bonding quality. ***11***

***Fig. 2.2.*** IR transmission image of a Si-Si wafer bond system showing unbonded regions at the interface. ***11***

***Fig. 2.3.*** Schematic diagram of the blade test method. ***11***

**Fig. 2.4.** Scheme of the xerogel fabrication process. ***12***

***Fig. 2.5.*** Silylation reaction scheme for different chemicals [Fru02]. ***13***

***Fig. 3.1.*** Types of infrared molecular vibrations. Arrows indicate the direction of the atomic movement; + indicates motion from page towards the reader; - indicates motion away from the reader (according to [Sko92]). ***16***

***Fig. 3.2.*** The bond energy diagram in a diatomic molecule considering harmonic oscillator model: classical treatment (parabola) and quantum treatment (energy levels and allowed transitions). ***16***

***Fig. 3.3.*** Energy diagram for a diatomic molecule considering the model of anharmonic oscillator (a).The phonon dispersion curves showing by arrows the allowed vibrational transitions between the phonon levels in the reduce-zone scheme according to [Hir02]. (b) ***18***

***Fig. 3.4.*** Electric field for p-polarisation. TO and LO modes. ***19***

***Fig. 3.5.*** Scheme of a Michelson interferometer. ***20***

***Fig. 3.6.*** A typical interferogram (left) and the corresponding spectrum obtained by Fourier transformation (right). ***21***

***Fig. 3.7.*** Schematic diagram of FTIR set-up for the Bruker IFS-66 spectrometer. ***21***

***Fig. 3.8.*** Schematical representation of Attenuated Total Reflection (ATR) and Multiple Internal Reflection (MIR) geometries. ***23***

***Fig. 3.9.*** Multiple Internal Transmission geometries used by Chabal and co-workers [Cha95, Wel96a,b] (a) and in our laboratory (b) to study the bonded interface in Si-Si bonded wafers. The path of the light in the case of external transmission (ET) is also plotted. ***24***

***Fig. 3.10.*** Picture of the set-up used for *ex situ* MIT measurements: the wafer (1), the prisms (2), the mirrors for alignment (3) the polariser (4) and the screws (5) for adjusting the optical contact prism-wafer are indicated on the picture. ***25***

***Fig. 3.11.*** IR external transmission (ET) spectrum and the corresponding multiple internal transmission spectrum for a Si-Si bonded wafer. ***26***

***Fig. 3.12.*** Experimental set-up for *in situ* MIT measurements: MIT geometry and heating plate (a); annealing low-vacuum chamber (b). ***28***

***Fig. 3.13.*** Interaction of linear polarized light with a sample. ***30***

***Fig. 3.14.*** Woollam VASE Ellipsometer. Optical fiber (1), polarizer (2), sample (3), analyser (4) and autoretarder (5) are marked on the picture by numbers. ***31***

***Fig. 3.15.*** $\Delta$ ellipsometric spectra for a xerogel film on Si sample measured without (open symbols) and with (filled symbols) autoretarder. ***32***

***Fig. 3.16.*** Analysis procedure for VASE data. ***33***

***Fig. 3.17.*** Schematic representations of effective medium theories [Ohw97]. ***35***

***Fig 3.18.*** SEM picture of a silica xerogel sample. ***36***

***Fig. 3.19.*** Schematic representation of the system used for EP measurements. ***37***

***Fig. 3.20.*** Typical adsorption and desorption isotherms of the toluene in/from the pores of a xerogel film (a) and the corresponding pore size distribution (b). ***38***

***Fig. 4.1.*** Experimental (symbols) and simulated (lines) imaginary part of the pseudo-dielectric function for Si-Si wafer bonds annealed at different temperatures. Inset shows the surface oxide thickness determined from the best fit to the experimental data. ***39***

***Fig. 4.2.*** IR transmission spectra of as-prepared (solid lines) and etched Si-Si bonded wafers (dotted lines). Spectra of the samples annealed at different temperatures are equidistantly shifted. ***41***

***Fig. 4.3.*** IR response of the surface silicon oxide of the Si-Si bonded wafers. ***41***

***Fig. 4.4.*** Dependence of TO and LO frequency position and $\nu_{LO}^2$-$\nu_{TO}^2$ value in the surface oxide as a function of annealing temperature. Solid and dotted lines are included as guides for the eye. ***42***

***Fig. 4.5.*** Experimental (symbols) and calculated (lines) IR transmission spectra of etched Si-Si bonded wafers. ***45***

***Fig. 4.6.*** Surface (ellipsometry results are shown by circles) and interface (IR and HRTEM data are squares and triangles, respectively) oxide thicknesses as a function of annealing temperature. ***46***

***Fig. 4.7.*** Cross sectional HRTEM images of the interface regions of the bonds annealed at 400°C (a), 800°C (b) and 1100°C (c). ***47***

***Fig.4.8.*** p- polarized IR MIT spectra of the prebonded and annealed at 400°C (solid lines) and 800°C (dotted lines) Si-Si wafer bonds measured in the spectral regions of SiH and $O_3$–SiH species (a) and OH and Si–OH species (b). The spectra were normalised with respect to spectrum of the sample annealed at 1100°C. ***47***

***Fig. 4.9.*** *In situ* MIT IR spectra recorded during annealing in the region of water and SiO-H absorption for a) RCA b) $O_2$ plasma and c) RIE samples. The temperature

increases in the direction of the arrows in the order: 30°, 100°, 125°, 150°, 175°, 200° and 225°C. ***50***

***Fig 4.10.*** Surface energies determined by the blade method for RCA, O2 plasma and RIE; 200°C (squares) and 400°C (stars) annealed samples. ***51***

***Fig. 4.11.*** MIT IR spectra of Si-Si bonded sample at RT, 225°C and after cooling and storage in air for 10 days. ***52***

***Fig. 4.12.*** *Ex situ* MIT IR spectra in the region of $O_y$-Si-$H_x$ vibrations measured at room temperature for a) RCA b) $O_2$ plasma and c) RIE samples. The spectra correspond to RT prebonded samples (——); 200°C annealed sample (·····); and 400°C annealed samples (- - - - ). ***53***

***Fig. 4.13.*** IR transmission image of prebonded (a) and annealed at 400°C (b) RIE sample. ***54***

***Fig. 4.14.*** Transmission spectra (70°, p-polarisation) of RT and 400°C Si-Si bonded wafers, in the region of LO mode in silicon oxide. ***54***

***Fig. 4.15.*** MIT IR spectra in the region of water and SiO-H stretching vibrations for 200°C Si-$SiO_2$ / Si bonded wafers with RCA, K1 and RIE pre-treatments. ***56***

***Fig. 4.16.*** Surface energies determined by blade method for 200°C annealed Si-$SiO_2$ / Si bonded wafers with RCA, K1 and RIE pre-treatments. ***56***

***Fig. 4.17.*** Evolution with annealing of the MIT IR spectra for RIE Si-$SiO_2$ / Si bonded wafers.

***Fig. 4.18.*** Schematic diagram of low temperature wafer bonding mechanism for Si-$SiO_2$ / Si bonded wafers. ***59***

***Fig. 5.1.*** $\Psi$ ellipsometric (a) and reflectance (b) spectra of a xerogel films on a Si substrate. The symbols are experimental data and solid lines are the fits obtained using a Cauchy model. ***61***

***Fig. 5.2.*** Optical constants of a silica xerogel film obtained from reflectance (squares) and ellipsometric (line) measurements. ***62***

***Fig. 5.3.*** $\Psi$ and $\Delta$ ellipsometric spectra of a silica xerogel film on a Si substrate. Symbols are the experimental points, continuous lines are the fits obtained using a Cauchy model and crosses lines are the fits obtained using EMA model. The spectra refer to sample C. ***64***

***Fig. 5.4.*** The refractive index of the xerogel films: solid lines are the calculated using Cauchy model and dotted lines are calculated using EMA model. The inset shows the extinction coefficient obtained considering Urbach absorbance. ***65***

***Fig. 5.5.*** Porosity (squares) and refractive index (circles) at 632.8 nm for samples A to E obtained by variation of the process parameters as presented in Table 5.1. ***66***

***Fig. 5.6.*** Plot of MSE values (filled squares) of EMA model as function of thickness. ***67***

***Fig. 5.7.*** Scheme of the hydrophobisation reaction of silica with HMDS. ***68***

***Fig. 5.8.*** FTIR-spectra of untreated and HMDS treated samples. The treatment time increases from 1 minute up to 4 h and the order of the corresponding spectra is indicated by the arrow. ***69***

***Fig. 5.9.*** Comparison of FTIR spectra of samples silylated by HMDS, TMSDEA or OTMSA (the spectra are in the order indicated by the arrows) for 1min (bottom) and for 4 hours exposure time (top). ***70***

***Fig. 5.10.*** The normalised absorbance spectra of the xerogel films in the region of CH stretching vibrations. ***71***

***Fig. 5.11.*** CH integrated intensity and refractive index (at 632.8 nm) as function of the porosity. (Dotted lines are guides to the eye.) ***72***

***Fig. 5.12.*** Experimental $\psi$ and $\Delta$ spectra (for 70° incidence angle) of an as-prepared (triangles) and HMDS treated (circles) xerogel film, and the fitted spectra considering Cauchy (dotted lines) and EMA (solid lines) models. ***73***

***Fig. 5.13.*** Refractive indices obtained by use of the Cauchy model for the as-prepared and HMDS-treated xerogel films, compared with the literature [Pal85] refractive index of $SiO_2$. ***74***

***Fig. 5.14.*** Porosity reduction function of treatment time for a HMDS treated sample. ***75***

***Fig. 5.15.*** IR absorption spectra for as-prepared (a) and HMDS treated (b) xerogel films. The experimental points are plotted by symbols, the components obtained by curve fitting by dotted lines and the fits by solid lines. A comparison for the peaks for as-prepared and HMDS treated films is also given (c). ***77***

***Fig. 5.16.*** (a) Adsorption-desorption isotherms of toluene in/from the pores of the xerogel films. The toluene condenses in the pores at vapour pressures (P) less than the equilibrium pressure ($P_0$). (b) Pore-size distributions in the xerogel films before and after HMDS-treatment, calculated from the desorption isotherms. ***80***

***Fig. 5.17.*** HRTEM image of a silica xerogel film. ***80***

***Fig. 5.18.*** IR absorption spectra of non-capped, SiN and SiO capped xerogel in the region of CH stretching vibrations. ***82***

***Fig 5.19*** Porosity (stars), electronic contribution including vacuum dielectric constant (squares) and static dielectric constant (circles) for the samples A24, S10, S24 and W24 respectively. ***84***

***Fig 5.20*** Dielectric constant in IR range derived from IR transmission spectra. ***85***

***Fig. 5.21*** Contribution to the static dielectric constant. ***86***

***Fig. 6.1.*** Schematical presentation of the procedures applied for characterisation of surface and interface oxide layers in Si-Si bonded wafers. ***88***

# Erklärung

Ich erkläre, dass ich die vorliegende Arbeit selbständig und nur unter Verwendung der angegebenen Literatur und Hilfsmittel angefertigt habe.

November 2002

Master in Physik Cameliu C. Himcinschi

# Lebenslauf

Cameliu Constantin HIMCINSCHI

Birthday: 29. Juni 1974

Birthplace: Blaj, Romania

Nationality: Romanian

Status: Married

**Studies:**

- **Ph. D. Student (Physics)** **Nov. 1999 ~ Nov. 2002**

Semiconductor Physics Laboratory

Chemnitz University of Technology, Germany

Supervisor: Prof. Dr. D.R.T. Zahn

- **Master of Science (Physics)** **Oct. 1996 ~ Jul.1997**

Solid State Physics

Babes-Bolyai University Cluj-Napoca, Romania in collaboration with Joseph-Fourier University, Grenoble, France

*Master thesis: "Magnetotransport proprieties for the perovskite ferromagnetic compounds of type $La_{1-x}Ca_xMnO_3$, M=Ca, Sr"* Supervisor: Dr. Laurent Ranno

- **Bachelor of Science (Physics)** **Oct.1992 ~ Jul.1996**

Bolyai University Cluj-Napoca (Romania)

Diploma thesis *"Determination of the detection efficacity for bulk samples by Monte Carlo simulation"* Supervisor: Prof. Dr. C. Cosma

- **High-School** **Sep.1988 ~ Jun.1992**

Theoretical Highscool "Iacob Muresianu", Blaj , Romania,

# Publication List

C.Himcinschi, M.Friedrich, S.Frühauf, I.Streiter, S.E.Schulz, T.Gessner, M.R.Baklanov, K.P.Mogilnikov, and D.R.T.Zahn- *Ellipsometric study of the change in the porosity of silica xerogels after surface chemical modification with hexamethyldisilazane*, **Analytical and Bioanalytical Chemistry 374 (2002) 654-657.**

C.Himcinschi, M.Friedrich, K.Hiller, T.Gessner, and D.R.T.Zahn - *Investigation during annealing of the interface in Si-Si bonded wafers by multiple internal transmission infrared spectroscopy*, International Semiconductor Conference (CAS) 2002, 8-12 october, 2002, Sinaia, Romania, **CAS 2002 Proceedings**, **vol. 2, 271-274** (published by IEEE).

S.Fruehauf, I.Streiter, S.E.Schulz, E.Brendler, C.Himcinschi, M.Friedrich, T.Gessner, and D.R.T.Zahn - *Hydrophobisation process for porous low-k dielectric silica layers*, **Conference Proceedings ULSI XVII 287-294**, published by Materials Research Society 2002.

C.Murray, C.Flannery, I.Streiter, S.E.Schulz, M.R.Baklanov, K.P.Mogilnikov, C.Himcinschi, M.Friedrich, D.R.T.Zahn, and T.Gessner- *Comparison of Techniques to Characterise the Density, Porosity and Elastic Modulus of Porous Low-k $SiO_2$ Xerogel Films,* **Microelectronics Engineering 60 (2002), 133-141.**

C.Himcinschi, M.Friedrich, C.Murray, I.Streiter, S.Schulz, T.Gessner, and, D.R.T.Zahn - *Characterisation of silica xerogels films by variable angle spectroscopic ellipsometry and infrared spectroscopy*, **Semiconductor Science and Technology 16 (2001), 806-811.**

C.Himcinschi, A.Milekhin, M.Friedrich, K.Hiller, M.Wiemer, T.Gessner, S.Schulze, and D.R.T.Zahn - *Silicon oxide in Si-Si bonded wafers,* **Applied Surface Science 175-176 (2001), 716-721.**

G.Salvan, C.Himcinschi, A.Yu.Kobitski, M.Friedrich, H.P.Wagner, T.U.Kampen, and D.R.T.Zahn - *Crystallinity of PTCDA films on silicon derived via optical spectroscopic measurements,* **Applied Surface Science 175-176 (2001), 364-369**.

C.Himcinschi, A.Milekhin, M.Friedrich, K.Hiller, M.Wiemer, T.Gessner, S.Schulze, and D.R.T.Zahn - *Growth of buried silicon oxide in Si-Si bonded wafers upon annealing,* **J. Appl. Phys. 89 (2001), 1992-1994.**

C.Himcinschi, E.Burzo, and J.P.Deville - *Magnetic and Magnetocaloric Properties of $La_{1.4-x}Yb_xCa_{1.6}Mn_2O_7$,* **Materials Science Forum 373-376 (2001), 521-524.**

I.Ardelean, G.Salvan, M.Peteanu, V.Simon, C.Himcinschi, and F.Ciorcas - *EPR and magnetic susceptibility studies of $B_2O_3$-SrO-$Fe_2O_3$ glasses* **Modern Physics Letters B, Vol. 13, Nos. 22 & 23 (1999), 801-808**.

# Acknowledgements

At the end of these 3 years of work I would like to thank to all people which help me to finish this dissertation.

My special thanks to Prof. Dr. DRT Zahn for giving me the opportunity to join “Halbleiterphysik” group, for the helpful discussions and for supervising my work.

I also thank to Prof. Dr. T. Gessner the head of the project SFB 379 where I was involved, and to Prof. Dr. U. Gösele (MPI Halle) for correcting and refereeing my dissertation.

My deepest gratitude goes to my lovely wife Georgeta for making possible getting this Ph.D. position, for trusting and encouraging me permanently.

Many thanks go to Dr. M. Friedrich for the fruitful discussions about infrared spectroscopy and ellipsometry and to Dr. A. Milekhin for introducing me to working with MIT set-up.

I would like to thank to Dr. K. Hiller for providing the wafer bonded samples and for the bonding energy measurements. Many thanks to Dr. S. Frühauf for the xerogels samples and for the nice collaboration we had. These thanks are also addressed to Chris, Isa and Dr. S.E. Schulz.

Thanks also to Dr. S. Schulze and G. Baumann for microscopy images.

The ellipsometric porosimetry measurements done by Dr. M. Baklanov (IMEC Leuven Belgium) and the useful discussions with Dr. T Wagner (LOT Oriel Darmstadt) about VASE helped me to deepen my ellipsometry knowledge.

I would like to express my appreciation to the other colleagues from Semiconductor Physics laboratory: Axel, Andreea, Andrei, Arindam, Beynor, Ela, Giani, Giang, Henry, Ilja, Matthias, Miruna, Reinhard, Simona, Sungook and Thorsten and to all others who have visited the lab for the nice time spent together.

I would also like to thank to Sybille Raschke, Katrin Träber and Kornelia Dostmann for the help in the administrative field.

Many thanks to Cristian for providing me part of the literature.

Finally I thank to my parents and my sister for the spiritual support provided me.